Further Studies on Seismic Interaction in Interconnected Electrical Substation Equipment

Armen Der Kiureghian
Kee-Jeung Hong
Jerome L. Sackman

Structural Engineering, Mechanics & Materials
Department of Civil & Environmental Engineering
University of California, Berkeley

A report on research sponsored by Pacific Gas & Electric Company (PG&E)
under Contract No. Z19-5-274-86 and the California Energy Commission
under Contract No. 500-97-101

PEER Report 2000/01
Pacific Earthquake Engineering Research Center
College of Engineering
University of California, Berkeley

November 1999

EXECUTIVE SUMMARY

In a previous study, we investigated the effect of interaction between interconnected electrical substation equipment subjected to ground motions. Each equipment item was modeled as a system with distributed mass and stiffness properties and, through the use of a displacement shape function, was characterized by a single degree of freedom. Two kinds of connecting elements were considered: One was a linear spring-dashpot-mass element, representing a rigid bus conductor, and another was an extensible cable, representing a flexible conductor, in which the flexural rigidity and inertia effects were neglected. It was shown that the interaction effect resulting from the interconnection could have a significant influence on the equipment responses. Amplification factors as high as 6 to 8 in the response of the higher frequency equipment item, relative to its stand-alone response, were estimated. In the cable-connected system, the response of the lower frequency equipment item may also be amplified but to a lesser extent.

The present study extends the results of the previous investigation in two important directions. First, it extends the investigation of the rigid bus conductor by accounting for the nonlinear behavior of the flexible strap connector (FSC), which is usually installed at one end of the bus conductor to allow for thermal expansion. Second, it extends the investigation of the flexible (cable) conductor by accounting for its flexural rigidity, inertia and damping characteristics. Both problems are highly nonlinear and advanced finite element models are used to perform the analyses.

To idealize the FSC, an elasto-plastic, large deformation finite element model is used with more than 500 elements. The material properties are determined from the results of monotonic uniaxial tests of the material coupons performed at the University of California at San Diego (UCSD). More accurate characterization of the material properties is possible if cyclic test data of the material coupons are available. The finite element model of the FSC is used to compute force-elongation hysteresis loops under a prescribed cyclic loading. These predictions show reasonable agreement with the experimental results obtained at UCSD. Closer agreement can be achieved by using a refined finite element model that accounts for contact and friction between the bars and straps of the FSC.

With such refinement, the finite element model can be used to predict the behavior of other FSC configurations, thus avoiding costly tests.

For dynamic analysis of the combined system, we develop a mathematical model of the hysteretic behavior of the FSC. For this purpose, we use a modified version of the well-known Bouc-Wen model. Using this model, time history analysis of a combined system, consisting of two equipment items connected by a rigid bus with a FSC, is carried out for two recorded ground motions. The effect of interaction on each equipment item is measured by computing the ratio of its response in the connected system to its stand-alone response. Separate analyses are performed to show the influences of the flexibility and energy dissipation of the FSC on the interaction effect. The results show that the flexibility and energy dissipation characteristics of the FSC significantly reduce the adverse effect of interaction on the higher frequency equipment item. These results appear to be in agreement with test results obtained at UCSD. The analytical approach developed can be used with confidence in the future to investigate the effect of interaction on equipment items connected by conductors that have grossly nonlinear behavior.

For the flexible (cable) conductor, a finite element model using frame elements and a Lagrangian formulation is used that accounts for large displacements. First, comparisons are made with previous experimental results for cables subjected to out-of-phase support motions. Good qualitative agreement with experimental results are obtained, which show very large amplification of the cable force due to the flexural rigidity and inertia effects. Parametric studies showing the influences of the flexural rigidity and damping of the cable are carried out. Next, the finite element model is used to carry out time history analyses of a combined system, consisting of two equipment items and a connecting cable, for five different recorded ground motions. Separate analyses are performed to show the influences of the cable flexural rigidity, inertia and damping. The effect of interaction on each equipment item is measured in terms of the ratio of the equipment response in the connected system to its stand-alone response. These response ratios are plotted as functions of an interaction parameter introduced in our previous study. The results show that, for certain ground motions and equipment/cable configurations, the cable flexural rigidity and inertia may further amplify the adverse effect of interaction. Based on these results, a

recommendation for the minimum cable length to avoid the adverse interaction effect is developed.

Conductor cables used in the power industry are usually made of braided aluminum strands of wire. Under dynamic excitation, the strands may slip against each other under friction forces. The present study accounts for this effect in an approximate manner by using an equivalent moment of inertia and a judgmentally assigned damping value. For a more accurate prediction of the cable response, it is necessary to develop a refined model that explicitly accounts for the slippage and friction between the cable strands. Until verified by such refined analyses, the results and recommendations presented in this study should be regarded as preliminary in nature.

CONTENTS

EXECUTIVE SUMMARY iii

ACKNOWLEDGMENTS vi

TABLE OF CONTENTS vii

LIST OF TABLES ix

LIST OF FIGURES xi

CHAPTER 1 — INTRODUCTION 1

1.1 Introduction 1

1.2 Organization of the Report 3

CHAPTER 2 — MODELING AND ANALYSIS OF SYSTEMS CONNECTED BY A RIGID BUS WITH A FLEXIBLE STRAP CONNECTOR ..5

2.1 Introduction 5

2.2 Model of the Rigid Bus with Flexible Strap Connector 6

2.3 Analytical Model of the RB-FSC 10

2.4 The Combined Equipment RB-FSC System 14

2.5 Investigation of the Interaction Effect in Example Systems 15

CHAPTER 3 — INFLUENCE OF THE BENDING STIFFNESS AND INERTIA OF THE CONNECTING CABLE ON THE INTERACTION EFFECT 49

3.1 Introduction 49

3.2 Section Properties of the Flexible Conductor 51

3.3 Finite Element Model of the Cable 53

3.4 Comparison of the Finite Element Model with the Catenary Cable 55

3.5 Comparison with Experimental Results of Dastous and Pierre 56

3.5.1 Experiment 1: Sine-Start Test 57

3.5.2 Experiment 2: Sine-Sweep Test 60

3.6 Cable-Connected Equipment Items 61

3.6.1 Effect of Flexural Rigidity, Inertia and Damping of the Cable on the Equipment Response 62

3.6.2 Effect of Interaction in the Cable-Connected System 64

CHAPTER 4 — SUMMARY AND RECOMMENDATIONS FOR FURTHER STUDY 87

4.1 Summary 87

4.2 Recommendations for Further Study 89

REFERENCES 91

LIST OF TABLES

CHAPTER 2

Table 2.1 Influence of the flexibility and energy dissipation of the RB-FSC on the effect of interaction on equipment items 20

Table 2.2 Influence of the flexibility and energy dissipation of the RB-FSC on the effect of interaction on the equipment combination 2 in the UCSD test 21

Table 2.3 Influence of the flexibility and energy dissipation of the RB-FSC on the effect of interaction on equipment the equipment combination 5 in the UCSD test 22

CHAPTER 3

Table 3.1 Properties of conductor cables used in the experiments by Dastous and Pierre 66

LIST OF FIGURES

CHAPTER 2

Figure 2.1 Rigid bus with a symmetric flexible strap connector 23

Figure 2.2 Dimensions of FSC No. 30-2022 23

Figure 2.3 Rigid bus with an asymmetric flexible strap connector 24

Figure 2.4 Dimensions of FSC No. 30-2021 24

Figure 2.5 Comparison of uniaxial tensile stress-strain relationship of FSC coupons generated in the UCSD tests with fitted model 25

Figure 2.6 Schematics of the finite element layout of the RB with symmetric FSC: (a) frame elements for the RB-FSC, (b) frame elements for the FSC, (c) extreme deformed shape under compression, and (d) extreme deformed shape under tension 26

Figure 2.7 Schematics of the finite element layout of the RB with asymmetric FSC: (a) frame elements for the RB-FSC, (b) frame elements for the FSC, (c) extreme deformed shape under compression, and (d) extreme deformed shape under tension 27

Figure 2.8 History of imposed support displacement used in the UCSD test 28

Figure 2.9 Comparison of FE predicted force-elongation relationship of the RB with the symmetric FSC with UCSD test results: (a) $H_{kin} = E/100$, (b) $H_{kin} = E/20$ 29

Figure 2.10 Comparison of FE predicted force-elongation relationship of the RB with the asymmetric FSC with UCSD test results for $H_{kin} = E/20$ 30

Figure 2.11 Force-elongation relationship of the first RB with symmetric FSC obtained from the UCSD test and from the modified Bouc-Wen model 31

Figure 2.12 Model of equipment items connected by a RB-FSC 32
Figure 2.13 Displacement time histories of the lower-frequency equipment item for the Newhall-Northridge record: (a) response in the stand-alone configuration and (b) response in the connected system 33
Figure 2.14 Displacement time histories of the higher-frequency equipment item for the Newhall-Northridge record: (a) response in the stand-alone configuration and (b) response in the connected system 34
Figure 2.15 Displacement time histories of the lower-frequency equipment item for the TabasLN record: (a) response in the stand-alone configuration and (b) response in the connected system 35
Figure 2.16 Displacement time histories of the higher-frequency equipment item for the TabasLN record: (a) response in the stand-alone configuration and (b) response in the connected system 36
Figure 2.17 Force-elongation hysteresis loops of the RB-FSC in the connected system subjected to the Newhall-Northridge record 37
Figure 2.18 Force-elongation hysteresis loops of the RB-FSC in the connected system subjected to the TabasLN record 37
Figure 2.19 Displacement time histories of the lower-frequency equipment item in the stand-alone configuration for the table motion TRB127 (Newhall 100%): (a) experiment and (b) analysis 38
Figure 2.20 Displacement time histories of the higher-frequency equipment item in the stand-alone configuration for the table motion TRB127 (Newhall 100%): (a) experiment and (b) analysis 39
Figure 2.21 Displacement time histories of the lower-frequency equipment item in the connected system for the table motion TRB101 (Newhall 100%): (a) experiment and (b) analysis 40
Figure 2.22 Displacement time histories of the higher-frequency equipment item in the connected system for the table motion TRB101 (Newhall 100%): (a) experiment and (b) analysis 41

Figure 2.23 Force-elongation hysteresis loops of the RB-FSC in the connected system subjected to the table motion TRB101 (Newhall 100%): (a) experiment and (b) analysis 42

Figure 2.24 Displacement time histories of the lower-frequency equipment item in the stand-alone configuration for the table motion TRB126 (Tabas 50%): (a) experiment and (b) analysis 43

Figure 2.25 Displacement time histories of the higher-frequency equipment item in the stand-alone configuration for the table motion TRB126 (Tabas 50%): (a) experiment and (b) analysis 44

Figure 2.26 Displacement time histories of the lower-frequency equipment item in the connected system for the table motion TRB100 (Tabas 50%): (a) experiment and (b) analysis 45

Figure 2.27 Displacement time histories of the higher-frequency equipment item in the connected system for the table motion TRB100 (Tabas 50%): (a) experiment and (b) analysis 46

Figure 2.28 Force-elongation hysteresis loops of the RB-FSC in the connected system subjected to the table motion TRB100 (Tabas 50%): (a) experiment and (b) analysis 47

CHAPTER 3

Figure 3.1 Cross section of a conductor cable made of braided wire strands 67

Figure 3.2 Comparison of exact and computed normalized responses of an oscillator to step loading : (a) oscillator with 5Hz frequency and 2% damping ratio, (b) oscillator with 50Hz frequency and 2% damping ratio 68

Figure 3.3 Horizontal force versus slackness for a cable with no flexural rigidity under its own weight 69

Figure 3.4 Shapes of cables of length $s_0 = 6\,\mathrm{m}$: (a) without flexural rigidity, (b) with flexural rigidity 70

Figure 3.5 Comparison of horizontal force-slackness relationship for a catenary cable and a cable with flexural rigidity 71
Figure 3.6 Time history of horizontal force at the cable support (after Dastous and Pierre, 1996) 72
Figure 3.7 Time history of horizontal force at the cable support as predicted by the finite element model 72
Figure 3.8 Sensitivity of the horizontal force at the support to cable moment of inertia 73
Figure 3.9 Finite element model of distributed viscous damping 74
Figure 3.10 Sensitivity of the horizontal force at the support to cable damping 74
Figure 3.11 Horizontal support force spectrum obtained from the experiment (after Dastous and Pierre, 1996) 75
Figure 3.12 Horizontal support force spectrum predicted by the finite element model 75
Figure 3.13 Cable-connected equipment items 76
Figure 3.14 N-S component of Newhall record, 1994 Northridge Earthquake 77
Figure 3.15 Displacement time histories of the stand-alone equipment items calculated by the damped energy-conserving algorithm 78
Figure 3.16 Displacement time histories of equipment items in the connected system, using catenary cable formulation and neglecting flexural rigidity, inertia and damping of the cable 79
Figure 3.17 Displacement time histories of equipment items in the connected system, including the inertia effect but neglecting the flexural rigidity and damping of the cable 80
Figure 3.18 Displacement time histories of equipment items in the connected system, including the flexural rigidity but neglecting the inertia and damping of the cable 81
Figure 3.19 Displacement time histories of equipment items in the connected system, including flexural rigidity and inertia, but neglecting the damping of the cable 82

Figure 3.20 Displacement time histories of equipment items in the connected system, including the flexural rigidity, inertia and damping of the cable 83

Figure 3.21 Response ratios for five earthquakes as functions of the interaction parameter neglecting the flexural rigidity, inertia and damping of the cable 84

Figure 3.22 Response ratios for five earthquakes as functions of the interaction parameter, including the flexural rigidity and inertia of the cable with zero damping 85

Chapter 1 Introduction

1.1 Introduction

In a previous report (Der Kiureghian et al., 1999), we studied the effects of interaction between interconnected electrical substation equipment subjected to ground motions. Investigated were equipment items connected by a linear spring-dashpot-mass element, representing a rigid bus conductor, and by an extensible cable representing a flexible conductor, in which the flexural rigidity and inertia effects of the cable were neglected. It was shown that the interaction effect resulting from the interconnection could have a significant influence on the equipment response. Amplification factors as high as 6 to 8 in the response of the higher-frequency equipment item, relative to its stand-alone response, were estimated. In cable-connected systems, the response of the lower-frequency equipment may also be amplified but normally by a much lesser extent.

The purpose of the present study is to further investigate the effects of seismic interaction between interconnected equipment items considering two specific problems: (a) the nonlinear behavior of the spring used for thermal expansion with rigid bus connectors and comparison with experimental results conducted at the University of California, San Diego, and (b) the influence of the flexural rigidity and inertia effect of the flexible (cable) conductor on the interaction effect.

The response of the rigid bus with the spring connector under severe earthquake loading is strongly inelastic with large deformations. Hence, it requires careful modeling and analysis to accurately reflect the real behavior. We have used an elasto-plastic, large deformation finite element model to predict the hysteretic behavior of the conductor consisting of a rigid bus and a flexible strap connector, which was tested at UCSD. The fi-

nite element code FEAP, developed by R. L. Taylor (1998), is used for this purpose. This study shows that the behavior of such systems can be predicted by finite element analysis with reasonable accuracy. For the dynamic analysis of the combined equipment conductor system, a modified version of the Bouc-Wen hysteretic model, which is fitted to the experimentally obtained hysteretic loops, is utilized. The results show that the flexibility and energy dissipation characteristics of the flexible strap conductor significantly reduce the adverse effect of interaction on the high-frequency equipment item, which is present when a rigid bus without the flexible strap connector is used. Quantitative estimates of the interaction effect are found to be in agreement with experimental results obtained at UCSD.

The cable dynamics problem is highly nonlinear and because of the special construction of the conductor cable as braided strands of wire involves significant uncertainties as to the effective cable properties, such as the flexural rigidity, damping and initial configuration. For this analysis, a finite element model with a Lagrangian strain formulation is utilized. Comparisons are made with previous experimental results for cables subjected to harmonic support excitations. While good qualitative agreement between the experimental and analytical results are achieved, questions regarding the effective cable stiffness and damping remain unanswered. Time history analyses of the cable-connected equipment items for five different recorded motions are carried out, separately accounting for the contributions of cable flexural rigidity, inertia and damping. The results show that, for certain ground motions and equipment/cable configurations, the cable flexural rigidity and inertia tend to further amplify the adverse interaction effect on the equipment items in comparison to what we had estimated without accounting for these effects. Based on this limited study, a preliminary recommendation for the minimum cable length to avoid the adverse interaction effect is formulated. Because of the importance of this problem, the scope of this part of the study was substantially broadened to include comparisons with experimental results that were discovered during the course of the study.

1.2 Organization of the Report

Following this introductory chapter, in Chapter 2 we present the analysis of the rigid bus with the flexible strap connector and the effect of interaction between two equipment items connected by such a conductor. Chapter 3 deals with the modeling and response analysis of cables and cable-connected equipment items. Chapter 4 summarizes the main results of the study and describes areas needing further investigation.

Chapter 2 Modeling and Analysis of Systems Connected by a Rigid Bus with a Flexible Strap Connector

2.1 Introduction

A rigid bus typically consists of an aluminum pipe connected between two electrical equipment items for conduction. To accommodate thermal expansion, a U-shaped spring element made of copper bars is normally inserted at one end of the rigid bus between the pipe and the attachment point on one of the equipment items. In the case of a severe earthquake, the relative displacement demand between the two equipment items in general will cause large inelastic deformation of the spring connector. In the first section of this chapter, we use an elasto-plastic model of the spring material together with a large deformation finite element analysis to predict the hysteretic response of the spring element under cyclic loading. Data from monotonic uni-axial testing of the material coupons is used to determine the material property constants. The predicted hysteresis loop is compared with experimental results obtained at the University of California, San Diego (UCSD, Filiatrault et al., 1999). A fairly good agreement between the two sets of results is obtained. However, in order to achieve more accuracy in the prediction, it is necessary to include in the finite element model the effects of contact and friction between bars, which give additional effective stiffness to the spring. Furthermore, it is necessary to have unloading data of the material coupons in order to more accurately determine the constitutive properties.

For dynamic analysis of the equipment items connected by the rigid bus and spring element, it is more convenient to employ an analytical model of the hysteretic behavior

for computational simplicity. To this end, we employ the well-known Bouc-Wen model (Wang and Wen, 1998), which we modify to fit the experimental results obtained at UCSD. This model, thereby, includes the effects of both material and geometric nonlinearities and the effects of both contact and friction between bars. The fitted model is subsequently used in a step-by-step dynamic analysis of the connected equipment system to determine the effect of interaction.

2.2 Model of the Rigid Bus with Flexible Strap Connector

Figure 2.1 shows a sketch of a typical rigid bus (RB) with a flexible strap connector (FSC). The RB consists of an aluminum pipe segment. At one end, it is rigidly attached to one of the equipment items. At the other end, the RB is attached to the FSC, which in turn is rigidly attached to the other equipment item. The FSC shown in Figure 2.2 is constructed from three straps, where each strap consists of two copper bars in the form of an inverted U. The dimensions shown in Figure 2.2 are consistent with the PG&E specification for FSC No. 30-2022 (Pacific Gas & Electric Company). Figures 2.3 and 2.4 show sketches of another typical RB-FSC and FSC, respectively. The dimensions shown in Figure 2.4 are consistent with the PG&E specification for FSC No. 30-2021.

Three coupons from a sample FSC were tested at UCSD under monotonic uniaxial tension to determine the material properties. Figure 2.5 shows the test results as dotted lines. Two of the curves exhibit small amplitude oscillations, which are presumed to be due to measurement noise. For the finite element analysis of the RB-FSC using the finite element analysis program FEAP (Taylor 1998), we employ an 1-dimensional elasto-plastic material model with hardening. In this model an additive split of the strain in the form

$$\varepsilon = \varepsilon^{el} + \varepsilon^{pl} \tag{2.1}$$

is assumed, where ε is the total strain, ε^{el} is the elastic strain and ε^{pl} is the plastic strain. The uniaxial constitutive relation is given by the following set of equations: The elastic stress-strain relation of the material is

$$\sigma = E(\varepsilon - \varepsilon^{pl}) \tag{2.2}$$

where σ is the applied stress and E is the Young's modulus. The yield condition is defined as

$$f(\sigma,\hat{q},\alpha)=|\sigma-\hat{q}|-\sigma_Y(\alpha)\leq 0 \tag{2.3}$$

where $\hat{q}$ is the back stress, α is the internal isotropic-hardening variable, and $\sigma_Y(\alpha)$ is the flow stress defined by the linear and saturated form of isotropic hardening, given by

$$\sigma_Y(\alpha)=\sigma_\infty+(\sigma_0-\sigma_\infty)\exp(-\beta\alpha)+H_{iso}\alpha \tag{2.4}$$

where $\alpha=|\varepsilon^{pl}|$ is assumed, σ_∞ is the stress at large strain, σ_0 is the initial yield stress, β is a delay constant, and H_{iso} is the modulus of linear isotropic hardening. The evolution of the back stress is defined by a linear kinematic hardening rule

$$\dot{\hat{q}}=H_{kin}\dot{\varepsilon}^{pl} \tag{2.5}$$

The associative flow rule gives the plastic strain rate in terms of the derivative of the yield function f, as

$$\dot{\varepsilon}^{pl}=\gamma\frac{\partial f}{\partial\sigma}=\gamma\,\mathrm{sgn}(\sigma-\hat{q}) \tag{2.6}$$

where γ is the absolute value of the flow rate. Since σ must satisfy the yield condition given by (2.3) and γ must be non-negative, we have the conditions

$$\gamma\geq 0 \quad\text{and}\quad f\leq 0 \tag{2.7}$$

If the absolute value of the applied stress, $|\sigma|$, is less than the flow stress σ_Y, no change in ε^{pl} takes place, i.e., $\gamma=0$ if $f<0$. On the other hand, a change in ε^{pl} can take place only if $f=0$, i.e., $\gamma>0$ only if $f=0$. Therefore, the condition

$$\gamma f=0 \tag{2.8}$$

always holds. The conditions given by (2.7) and (2.8) are known as the Kuhn-Tucker conditions. The additional condition

$$\gamma\dot{f}=0 \quad\text{when}\quad f=0 \tag{2.9}$$

is necessary because, when $f=0$, we specify $\gamma>0$ only if $\dot{f}=0$, and set $\gamma=0$ if $\dot{f}<0$. This condition is referred to as the consistency condition and is used, together

with the Kuhn-Tucker conditions, to determine the actual value of $\gamma \geq 0$ at any given time. A more detailed description of this plastic model can be found in Simo and Hughes (1998).

The uniaxial tensile test results of the FSC coupons supplied by UCSD did not contain any unloading data. Therefore, it is difficult to determine both isotropic and kinematic hardening moduli from this data. If we simulate the tensile test by a finite element analysis using one frame element with a judgmentally chosen elasto-plastic hardening model having parameters $E = 14{,}000\,\text{ksi}$, $\sigma_0 = 18\,\text{ksi}$, $\sigma_\infty = 27.5\,\text{ksi}$, $\beta = 1000$, $H_{iso} = 0$ and $H_{kin} = E/100$, we obtain the solid line shown in Figure 2.5, which closely matches the actual data. We apply this model below to analyze the RB-FSC by the finite element method.

Figures 2.6a and 2.6b show schematics of the finite element layout of an RB-FSC, which was tested at UCSD. The RB is a 4in-diameter SPS aluminum pipe of 10ft length, having an inner radius of 2.013in. and an outer radius of 2.250in. The main body of the RB is modeled with 10 elastic frame elements, whereas connections A and B shown in Figure 2.2 are modeled with 1 and 6 elastic frame elements, respectively. The Young's modulus of the RB is assumed to be $E = 10{,}000\,\text{ksi}$. The selected FSC is consistent with the PG&E specification No. 30-2022. It is made of three parallel straps, each consisting of a pair of copper bars, and has the material properties mentioned earlier. Each bar of the FSC is modeled by 80 elasto-plastic frame elements, each element consisting of 10 layers to properly account for the plastic behavior through the thickness of the bar. In addition, 20 elastic frame elements are used to model the spacers between the bars at the ends and 2 elastic frame elements are used to model the spacers between the RB and the FSC. Thus, in total, the RB-FSC is modeled by 519 frame elements of which 480 are elasto-plastic.

Figures 2.7a and 2.7b show schematics of the finite element layout of a second RB-FSC, which was also tested at UCSD. The RB is the same as described above, whereas the FSC is consistent with the PG&E specification No. 30-2021. A finite element mesh similar to that described in the previous paragraph was used to model this RB-FSC.

For the finite element analysis, one end of the RB-FSC is assumed to be fixed, while the other end is subjected to the horizontal displacement time history utilized in the UCSD tests, which is shown in Figure 2.8. The finite element program FEAP by R. L. Taylor (1998), which employs a Lagrangian strain formulation to account for large deformations, is used to predict the cyclic response of the RB with the 30-2022 FSC. The computed force-elongation relationship is plotted in Figure 2.9a. The agreement between the two hysteresis loops is fairly good. However, the experimental curves show apparent hardening for large elongation or contraction values, which are not well predicted by the finite element model. This might be due to the wrong choice of the hardening moduli and/or due to the effect of contact and friction between bars and straps, which are not accounted for in the finite element model. In the test, significant friction could occur between bars in a strap, and contact between straps would occur for extreme states of deformation. The contact and friction between the bars and straps would provide additional effective stiffness to the RB-FSC. To account for this effect in an approximate manner, we can use a larger value of the kinematic hardening modulus, even though we lose accuracy in matching the uniaxial test results. After a number of trials, we found the value $H_{\text{kin}} = E/20$ of the kinematic hardening coefficient produce results that best fit the test hysteresis loops. The result, shown in Figure 2.9b, demonstrates much closer agreement with the test results. The extreme deformed shapes of the RB-FSC obtained from this analysis are shown in Figures 2.6c and 2.6d.

If the deviations between the computed and test results in Figure 2.9a were truly due to material effects, then this revised value of the hardening parameter should produce good results for other FSC models as well. However, as we will shortly see, this is not the case. That is, the deviations seen in Figure 2.9a are more due to contact and friction between the bars and straps than due to material characterization.

Next, we use the chosen material parameter values to conduct finite element analysis of the RB with the 30-2021 FSC, which has an asymmetric shape as shown in Figure 2.7. The computed hysteresis loops are compared with the UCSD test results in Figure 2.10 and the extreme deformed shapes are shown in Figures 2.7c and 2.7d. It is seen that there is a more significant difference between the computed and test results. This difference is

due to a more significant effect of contact and friction between bars and straps for this asymmetric configuration of the FSC. It is clear that the material characterization alone cannot account for this effective added hardening across different RB-FSC systems.

The above comparisons show that, while the finite element predictions of the cyclic behavior of the RB-FSC are in reasonable agreement with test results, for enhanced accuracy it is necessary to develop a finite element model that accounts for the effect of contact and friction between the bars and straps of the FSC. Furthermore, it is necessary to perform cyclic tests of the FSC coupons so that the hardening moduli can be estimated properly. By achieving these, the behavior of the RB-FSC under large deformations can be well predicted by a finite element model that accounts for the elasto-plastic material behavior, the effect of contact and friction between bars, and large deformations. Such an analysis can be performed in the future in lieu of costly testing to determine the behavior of other RB-FSC configurations.

2.3 Analytical Model of the RB-FSC

For the analysis of the RB-FSC-connected equipment system, the above finite element model is not convenient, as it would involve a very large nonlinear dynamic model. In this section, we use an analytical model to fit the hysteresis loops of the RB-FSC, which is then used in the subsequent section to carry out dynamic analysis of the combined system. This approach has the advantage of computational simplicity. Furthermore, it allows for a random vibration analysis of the combined system, which we intend to carry out as a follow-up to this study. Such an approach would properly account for the variability that is present in the earthquake excitation.

To analytically describe the behavior of the RB-FSC, we employ the well-known hysteresis model originally proposed by Bouc (1967) and later modified by Wen (1976). This model has been generalized by Baber and Wen (1979) for degrading systems and by Wang and Wen (1998) to account for asymmetric yielding behavior. Since the hysteresis loops of the RB-FSC element exhibit asymmetric behavior due to geometric nonlinearity, we employ the form of the model suggested by Wang and Wen (1998). According to this model, the nonlinear force-elongation relationship for the RB-FSC element is defined by

$$q(\Delta u, z) = \alpha k \Delta u + (1-\alpha) k z \tag{2.10}$$

where $q(\Delta u, z)$ is the force acting on the element, Δu is the resulting elongation, k is the initial elastic stiffness, α is the post-to-pre-yielding stiffness ratio, and z is the hysteretic part of the elongation satisfying the differential equation

$$\dot{z} = \frac{\Delta \dot{u}}{\eta}\left[A - \nu |z|^n \{\beta \operatorname{sgn}(\Delta \dot{u} z) + \gamma + \phi(\operatorname{sgn}(z) + \operatorname{sgn}(\Delta \dot{u}))\}\right] \tag{2.11}$$

In the preceding equation, A, β, γ, and n are parameters that control the shape of hysteresis loop, η is a parameter that controls the pre-yielding stiffness, ν is a parameter that controls the ultimate strength, and ϕ is a parameter that accounts for the asymmetric yielding behavior. Also, $\operatorname{sgn}(x) = 1$ for $x > 0$, $\operatorname{sgn}(x) = -1$ for $x < 0$, and $\operatorname{sgn}(x) = 0$ for $x = 0$.

Baber and Wen defined A, η and ν as functions of the total dissipated energy, ε_T,

$$A(\varepsilon_T) = A_0 - \delta_A \varepsilon_T, \quad \eta(\varepsilon_T) = \eta_0 - \delta_\eta \varepsilon_T, \quad \nu(\varepsilon_T) = \nu_0 - \delta_\nu \varepsilon_T \tag{2.12}$$

$$\varepsilon_T = (1-\alpha) k \int_0^t z \Delta \dot{u} \, dt \tag{2.13}$$

In the preceding equations, A_0, η_0 and ν_0 are initial values of A, η and ν, respectively, and δ_A, δ_η and δ_ν are parameters that control the rate of degradation. This model of deterioration is capable of accounting for the duration and severity of the response. The quasi-static tests conducted at UCSD incorporate geometric and material nonlinearities and contact and friction between bars. It is difficult to derive equations that simulate the behavior of the RB-FSC and account for these effects. Motivated by the Baber-Wen approach, we fit the test behavior of the RB-FSC by letting the parameters A, η and ν be functions of the response. Specifically, these parameters are considered to be functions of the elongation/contraction Δu and its rate $\Delta \dot{u}$ to account for the dependency of the nonlinearity on the response and the state of loading. For this purpose, we introduce the following limiting response values:

Δu_t^E marker for the limit of the nearly elastic elongation zone

Δu_c^E marker for the limit of the nearly elastic contraction zone

Δu_t^m maximum elongation experienced during the test

Δu_c^m maximum contraction experienced during the test

Associated with the nearly elastic zone, we define the parameter values A^E, η^E and ν^E. Associated with Δu_t^u (Δu_c^u), we define the parameter values A_t^+, η_t^+, ν_t^+ A_t^-, η_t^- and ν_t^- (A_c^+, η_c^+, ν_c^+, A_c^-, η_c^- and ν_c^-), where a superposed + denotes a "loading" state, i.e., $\Delta\dot{u} \geq 0$, and a superposed – denotes an "unloading" state, i.e., $\Delta\dot{u} < 0$. Furthermore, we define the set of parameters A_0^+, η_0^+, ν_0^+, A_0^-, η_0^- and ν_0^- associated with the state $\Delta u = 0$.

Initially, the parameters A, η and ν are set to the values A^E, η^E and ν^E. These values are kept fixed until a reversal of loading occurs outside the nearly elastic zone. From that point on, the parameters A, η and ν are made functions of Δu. For a given Δu, their values are obtained by interpolating between the extreme values associated with the states $\Delta u = 0$ and either Δu_t^m or Δu_c^m, depending on whether the RB-FSC is elongated or compressed. The extreme parameter values selected are those with superscript + if $\Delta\dot{u} \geq 0$ and those with superscript – if $\Delta\dot{u} < 0$. A simple parabolic interpolation between the two extreme parameter values is used to determine the current value of each parameter. For example, subsequent to a point of load reversal outside the nearly elastic zone when the element is in contraction and $\Delta\dot{u} < 0$, we obtain the value of parameter A for a given Δu from

$$A(\Delta u) = (A_c^- - A_0^-)\left(\frac{\Delta u}{\Delta u_c^m}\right)^2 + A_0^- \tag{2.14}$$

If a reversal of loading occurs inside the nearly elastic zone, the parameter values are again set to the constant values A^E, η^E and ν^E.

Based on the extreme displacements imposed on the test RB-FSC, we selected $\Delta u_t^m = 8$ in. and $\Delta u_c^m = -6$ in. Furthermore, observing the range of nearly elastic behavior, the limiting values $\Delta u_t^E = 2$ in. and $\Delta u_c^E = -2$ in. were chosen. Of the parameters of

the Bouc-Wen model, $k = 200$ lbs/in., $n = 2$, $\alpha = 0.1$, $\beta = 0.507$, $\gamma = 0.485$, $A^E = 0.42$, $\eta^E = 0.34$ and $\nu^E = 0.08\,\text{in.}^{-2}$ were selected by trial-and-error fitting of the overall features of the hysteresis loops obtained in the test. For the parameter ϕ, which controls the asymmetric yielding behavior, the initial value $\phi = 0.1$ is selected. This value is used until a reversal of loading outside the nearly elastic zone is encountered, in which case the parameter is set to $\phi = -0.1$. This value remains in effect until a reversal of loading within the nearly elastic zone occurs, in which case the parameter is reset to $\phi = 0.1$. This modification is necessary to avoid vertical shifting of the narrow hysteresis loop in the nearly elastic zone. This leaves us 18 parameters associated with the three extreme values of the parameter set A, η and ν. These are obtained by minimizing the cumulative squared error between the experimental values and the predictions by the Bouc-Wen model together with trial-and-error to search for a better local minimum. The resulting optimal parameter values were:

$$A_0^+ = 0.27,\ A_0^- = 0.42,\ A_t^+ = 0.47,\ A_t^- = 0.42,\ A_c^+ = 0.42,\ A_c^- = 0.42$$

$$\eta_0^+ = 0.27,\ \eta_0^- = 0.34,\ \eta_t^+ = 0.30,\ \eta_t^- = 0.14,\ \eta_c^+ = 0.34,\ \eta_c^- = 0.34$$

$$\nu_0^+ = 0.06\,\text{in.}^{-2},\ \nu_0^- = 0.08\,\text{in.}^{-2},\ \nu_t^+ = 0.04\,\text{in.}^{-2},\ \nu_t^- = 0.04\,\text{in.}^{-2},\ \nu_c^+ = 0.04\,\text{in.}^{-2},\ \nu_c^- = 0.08\,\text{in.}^{-2}$$

where A and η are dimensionless and ν has the unit of in.$^{-2}$ (for $n = 2$).

Figure 2.11 shows a comparison of the hysteresis loops obtained in the UCSD experiments together with the hysteresis loops obtained from the modified Bouc-Wen model described above. It is evident that the model predictions are in close agreement with the test results. It is particularly noteworthy that the model closely follows the asymmetric features of the actual hysteresis loops. This model is used in the following section to investigate the interaction between two equipment items attached by a RB-FSC.

2.4 The Combined Equipment RB-FSC System

In this section, we develop the equations for the system shown in Figure 2.12, which consists of two equipment items connected by a RB-FSC represented by the modified Bouc-Wen model described above. In the subsequent section, we carry out time history analyses to compute the responses of the stand-alone and connected systems to selected earthquake ground motions in order to determine the effect of the interaction on the equipment items.

As in our previous study (Der Kiureghian et al., 1999), we employ a single-degree-of-freedom model for each equipment item that is characterized by distributed mass and stiffness properties and a single displacement shape function. The displacement of equipment i is written in the form $u_i(y,t) = \psi_i(y) z_i(t)$, where y is the spatial coordinate, $\psi_i(y)$ is the displacement shape function, and $z_i(t)$ is the generalized coordinate that defines the variations of the displacement shape in time. For an equipment item modeled as a beam of length L_i, the equivalent mass and stiffness are respectively given by

$$m_i = \int_0^{L_i} \rho_i(y) [\psi_i(y)]^2 dy, \tag{2.15}$$

$$k_i = \int_0^{L_i} EI_i(y) [\psi_i''(y)]^2 dy \tag{2.16}$$

and the effective mass producing the external inertia force is given by

$$l_i(y_i) = \psi_i(y_i) \int_0^{L_i} \rho_i(y) \psi_i(y) dy \tag{2.17}$$

In the above expressions, $\rho_i(y)$ is the mass per unit length of the equipment, $EI_i(y)$ is the flexural stiffness, and y_i is the coordinate at the point where the connecting element is attached to the equipment. For reasons described in the previous study, it is advantageous to scale the shape functions such that $\psi_i(y_i) = 1$. Furthermore, it is convenient to introduce the abbreviated notation $u_i(t) = u_i(y_i, t)$ and $l_i = l_i(y_i)$. The equations of motion of the connected system expressed in terms of the displacements at the attachment points when it is subjected to base acceleration $\ddot{x}_g$ can now be written as

$$\mathbf{M}\,\ddot{\mathbf{u}} + \mathbf{C}\,\dot{\mathbf{u}} + \mathbf{R}(\mathbf{u}, z) = -\mathbf{L}\,\ddot{x}_g \tag{2.18}$$

where

$$\mathbf{u} = \begin{Bmatrix} u_1(t) \\ u_2(t) \end{Bmatrix},\ \mathbf{M} = \begin{bmatrix} m_1 & 0 \\ 0 & m_2 \end{bmatrix},\ \mathbf{C} = \begin{bmatrix} c_1 + c_0 & -c_0 \\ -c_0 & c_2 + c_0 \end{bmatrix}, \tag{2.19a}$$

$$\mathbf{R}(\mathbf{u}, z) = \begin{Bmatrix} k_1\, u_1(t) - q(\Delta u, z) \\ k_2\, u_2(t) + q(\Delta u, z) \end{Bmatrix},\ \mathbf{L} = \begin{Bmatrix} l_1 \\ l_2 \end{Bmatrix} \tag{2.19b}$$

and the modified Bouc-Wen model is defined by

$$q(\Delta u, z) = \alpha k\, \Delta u + (1 - \alpha) k z \tag{2.20a}$$

$$\dot{z} = \frac{\Delta \dot{u}}{\eta}\left[A - \nu |z|^n \{\beta \operatorname{sgn}(\Delta \dot{u}\, z) + \gamma + \phi(\operatorname{sgn}(z) + \operatorname{sgn}(\Delta \dot{u}))\}\right] \tag{2.20b}$$

where $\Delta u = u_2(t) - u_1(t)$ is the relative displacement between the two equipment items, which is equivalent to the elongation/contraction of the RB-FSC. In (2.18), we have added a viscous damping matrix similar to that described in our previous study (see Equation (2.10) in Chapter 2 of Der Kiureghian et al., 1999). Elements c_1 and c_2 of the damping matrix in (2.19a) represent the damping coefficients of the two equipment items, whereas c_0 represents the viscous damping of the RB-FSC. In the following analysis, we have used $c_0 = 0$, since the amount of energy dissipated by viscous damping would be negligible in comparison to that dissipated by the inelastic action in the FSC.

For the numerical results reported in the following section, the above system of equations were solved by a 4th order Runge-Kutta algorithm using automatically varying time steps with a relative tolerance of 10^{-6}.

2.5 Investigation of the Interaction Effect in Example Systems

In this section, we examine the effect of interaction between two equipment items connected by a RB-FSC and subjected to selected earthquake ground motions. As in our previous study, we examine the effect of interaction by computing the response ratios

$$R_i = \frac{\max|u_i(t)|}{\max|u_{i0}(t)|}, \quad i = 1,2 \tag{2.21}$$

where $u_i(t)$ and $u_{i0}(t)$ denote the responses of equipment i in the connected and stand-alone systems, respectively. As should be clear, a value greater than unity for a response ratio implies amplification of the corresponding equipment response in the connected system in comparison to its stand-alone response. To the contrary, a value smaller than unity for a response ratio implies de-amplification of the corresponding equipment response. As discussed in the earlier study, although these response ratios are computed for the displacement responses, they are equally valid for internal forces in each equipment item.

In the following, we investigate three example systems. The first system has properties that are similar to that of a system investigated in our previous study (described in page 55 of Der Kiureghian et al., 1999). The other two examples have properties similar to two of the systems tested at UCSD.

The first example system has the properties: $m_1 = 5.71\,\text{lb.s}^2/\text{in}$, $\omega_1 = \sqrt{k_1/m_1} = 4\pi\,\text{rad/s}$ and $\zeta_1 = c_1/(2\omega_1 m_1) = 0.02$ for equipment 1, and $m_2 = 2.85\,\text{lb.s}^2/\text{in.}$, $\omega_2 = \sqrt{k_2/m_2} = 10\pi\,\text{rad/s}$, and $\zeta_2 = c_2/(2\omega_2 m_2) = 0.02$ for equipment 2. The RB has the properties described earlier in this chapter. The FSC is selected in accordance to the PG&E specification No. 30-2022. Figures 2.13 and 2.14 show the response pairs $(u_{10}(t), u_1(t))$ and $(u_{20}(t), u_2(t))$, respectively, of the two equipment items in the stand-alone and connected configurations, when the system is subjected to the N-S component of the Newhall record of the Northridge (1994) earthquake. Figures 2.15 and 2.16 show the same for the system subjected to the longitudinal record of Tabas (1978) earthquake (TabasLN). The ratios of the peak responses in the connected and stand-alone systems are $R_1 = 0.757$ and $R_2 = 0.931$ for the Northridge earthquake and $R_1 = 0.845$ and $R_2 = 0.776$ for the TabasLN. It is apparent that the responses of both equipment items in the connected system are de-amplified relative to their stand-alone responses. Figures 2.17 and 2.18 show the force-elongation hysteresis loops of the RB-FSC for the two

earthquakes. These plots show significant nonlinearity and energy dissipation in the FSC.

To quantify the influences of the flexibility and energy dissipation characteristics of the FSC, we repeat the above analysis while entirely removing the FSC. In this case, the connection has the full elastic axial rigidity of the RB, which is equal to $k_0 = 264{,}504$ lbs/in. According to the definition in our previous study, this corresponds to a stiffness ratio of $\kappa = k_0/(k_1 + k_2) = 71.2$. To quantify the influence of the energy dissipation capacity of the FSC, we repeat the analysis while using an ideally elastic model of the FSC with its initial stiffness $k_0 = 225$ lbs/in., which corresponds to the stiffness ratio $\kappa = k_0/(k_1 + k_2) = 0.0606$. The response ratios from these analyses are summarized in Table 2.1.

Our interest is in cases where $R_2 > 1$ in Table 2.1, since a response ratio larger than 1 indicates an adverse interaction effect on an equipment item. By attaching the FSC to RB, we increase the flexibility of the conductor and thereby reduce the response ratio R_2 of the higher-frequency equipment from 3.526 to 1.053 (70% reduction) for the Northridge earthquake and from 1.272 to 0.884 (31% reduction) for the TabasLN earthquake. Furthermore, when we consider the energy dissipation provided by the FSC, R_2 is further reduced from 1.053 to 0.931 (12% reduction) for the Northridge earthquake and from 0.884 to 0.776 (12% reduction) for the TabasLN earthquake. This comparison clearly shows that, for this example system, the flexibility of the FSC is much more significant in reducing the adverse effect of the interaction than the energy dissipation of the RB-FSC. However, it is expected that if the RB-FSC is subjected to a larger relative displacement, then energy dissipation will be larger so that it will have more influence on reducing responses. Clearly, the considered flexible strap connector (the PG&E 30-2022 FSC) provides a significant advantage in reducing the adverse effects of interaction between the connected equipment items.

The second example considered is the equipment combination (pair) 2 used in the UCSD experiments (Filiatrault et al. 1999). Adjusted frequency and damping values for this system were determined through discussions with A. Filiatrault of UCSD. The as-

sumed displacement shape function corresponds to the static displacement of a cantilever with an end load. The property values used in the analysis are: $m_1 = 2.057$ lb.s^2/in., $\omega_1 / 2\pi = 1.945$ Hz and $\zeta_1 = 0.013$ for equipment 1, and $m_2 = 0.422$ lb.s^2/in., $\omega_2 / 2\pi = 5.47$ Hz and $\zeta_2 = 0.013$ for equipment 2. Figures 2.19-2.22 compare the responses of the two equipment items in their stand-alone (Figures 2.19 and 2.20) and connected (Figures 2.21 and 2.22) configurations, as obtained in the experiments (top figures) and as predicted by analysis, for the table motion simulating the Newhall 1994 record at 100% span. While the two sets of response time histories are not in close agreement, general features are alike. For example, both experimental and analytical results show that the response of the lower-frequency equipment item is de-amplified as a result of the interaction, whereas that of the higher-frequency equipment item is amplified. This is consistent with the results established in our previous study for linearly connected equipment systems. Figure 2.23 shows the force-displacement hysteresis loop for the FSC under this excitation. Whereas the overall shapes of the experimental and analytical hysteresis loops are similar, the effective stiffness of the FSC deduced from the test is found to be much larger than that predicted analytically. The analytical value actually matches the effective stiffness of the FSC directly measured under quasi-static cyclic loads at UCSD. Based on our discussions with A. Filiatrault, we believe the higher stiffness measured for the FSC in this dynamic test has to do with the manner of attachment of the RB-FSC to the equipment items. It is noteworthy that for the present example the FSC does not experience a large degree of nonlinearity or energy dissipation.

Figures 2.24-2.28 show similar comparisons between experimental and analytical predictions of the equipment responses to a table motion simulating the Tabas 1978 ground motion at 50% span. The trends here are similar to those observed in Figures 2.19-2.23 for the Newhall motion.

Table 2.2 lists the response ratios for the example system for the two table motions. In addition to the cases described above, we have included the response ratios for systems without the FSC and for systems with linear FSC in the same manner as in Table 2.1. The experimental values are listed in parenthesis in the last row of the table. It is observed that the flexibility of the FSC significantly contributes to reducing the interaction

effect, whereas the energy dissipation within the FSC reduces the interaction effect by a small amount. Furthermore, the response predictions by the analytical method are in reasonably close agreement with those measured in the experiments.

Analyses similar to the above were carried out for the system with equipment combination 5 in the UCSD tests. This system has the properties: $m_1 = 2.057\,\text{lb.s}^2/\text{in.}$, $\omega_1/2\pi = 1.945\,\text{Hz}$ and $\zeta_1 = 0.013$ for equipment 1, and $m_2 = 0.422\,\text{lb.s}^2/\text{in.}$, $\omega_2/2\pi = 12.23\,\text{Hz}$ and $\zeta_2 = 0.009$ for equipment 2. In this case, equipment 2 had displacements smaller than the measurement error, and reliable experimental estimates of its response consequently could not be obtained. For the sake of brevity, here we list only the predicted response ratios in Table 2.3, where the test values only for equipment 1 are shown in parenthesis in the last row. The very large amplification of the higher-frequency equipment item for this system, even when the flexibility and energy dissipation of the FSC are accounted for, is due to the large separation between the frequencies of the two equipment items. This example serves to once again demonstrate the adverse effect of interaction when equipment items with widely separated frequencies are connected.

Table 2.1 Influence of the flexibility and energy dissipation of the RB-FSC on the effect of interaction on equipment items

Connector	R_1		R_2	
	Northridge	TabasLN	Northridge	TabasLN
RB ($\kappa = 71.2$)	0.4172	0.513	**3.5256**	**1.272**
Linear Spring with Initial Stiffness ($\kappa = 0.0606$)	0.844	0.901	**1.053**	0.884
RB-FSC	0.757	0.845	0.931	0.776

Table 2.2 Influence of the flexibility and energy dissipation of the RB-FSC on the effect of interaction on the equipment combination 2 in the UCSD test

Connector	R_1		R_2	
	Newhall 100% span	Tabas 50% span	Newhall 100% span	Tabas 50% span
RB (κ=328)	0.4461	0.7012	**2.8767**	**3.2682**
Linear Spring with Initial Stiffness (κ=0.2793)	0.5804	0.8001	**1.5953**	**1.4083**
RB-FSC (UCSD experiment)	0.5277 (0.5689)	0.6879 (0.6255)	**1.5509 (1.2150)**	**1.2707 (1.2959)**

Table 2.3 Influence of the flexibility and energy dissipation of the RB-FSC on the effect of interaction on equipment the equipment combination 5 in the UCSD test

Connector	R_1		R_2	
	Newhall 100% span	Tabas 50% span	Newhall 100% span	Tabas 50% span
RB (κ=94.5)	0.1068	0.1431	**7.9218**	**7.8270**
Linear Spring with Initial Stiffness (κ=0.08)	0.5595	0.7677	**3.6879**	**3.6610**
RB-FSC (UCSD experiment)	0.4107 (0.3854)	0.6790 (0.4367)	**3.0058**	**2.5939**

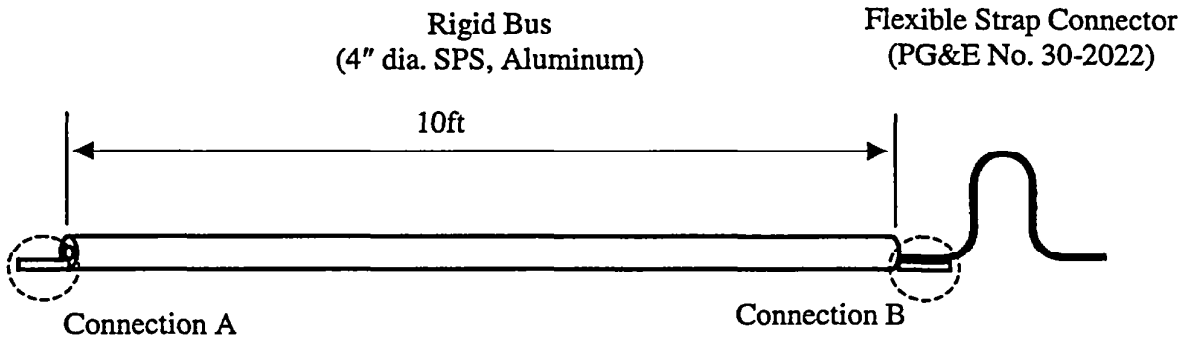

Figure 2.1 Rigid bus with a symmetric flexible strap connector

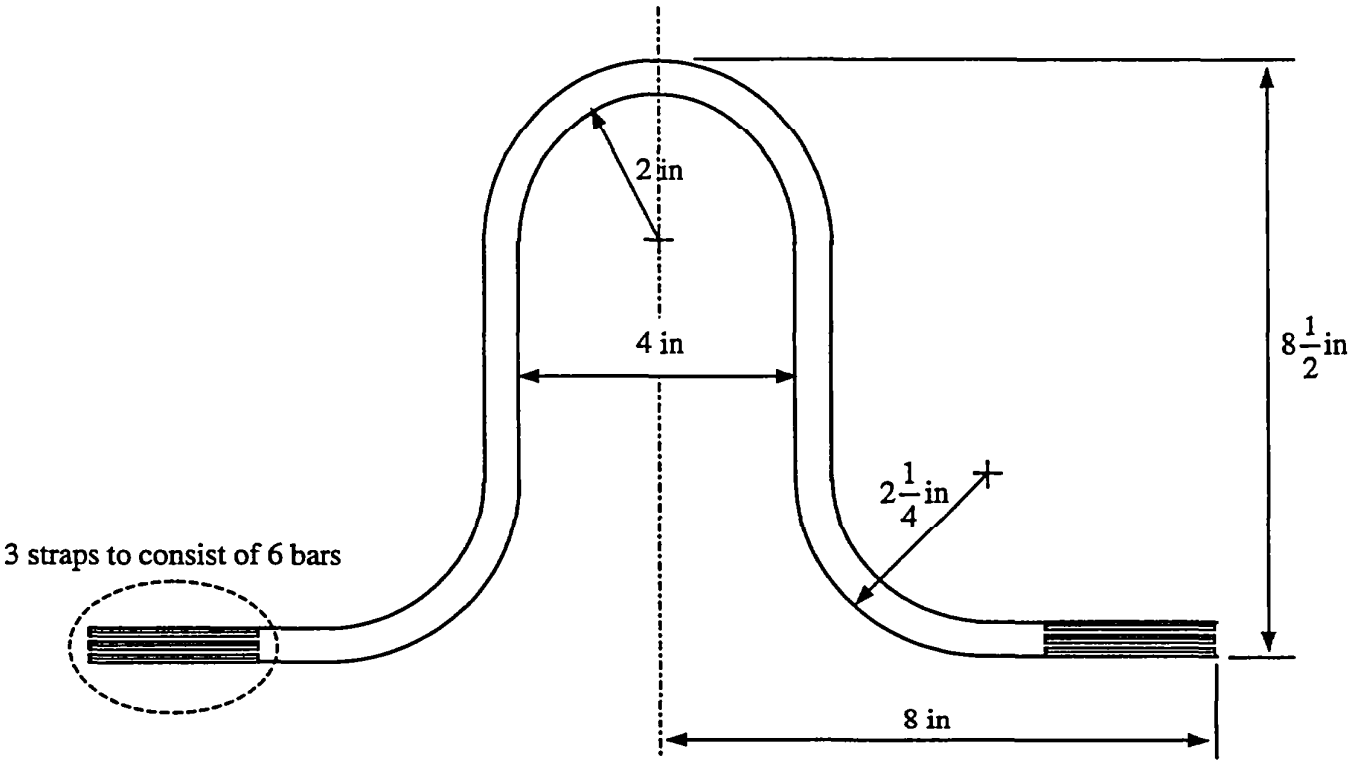

Figure 2.2 Dimensions of FSC No. 30-2022

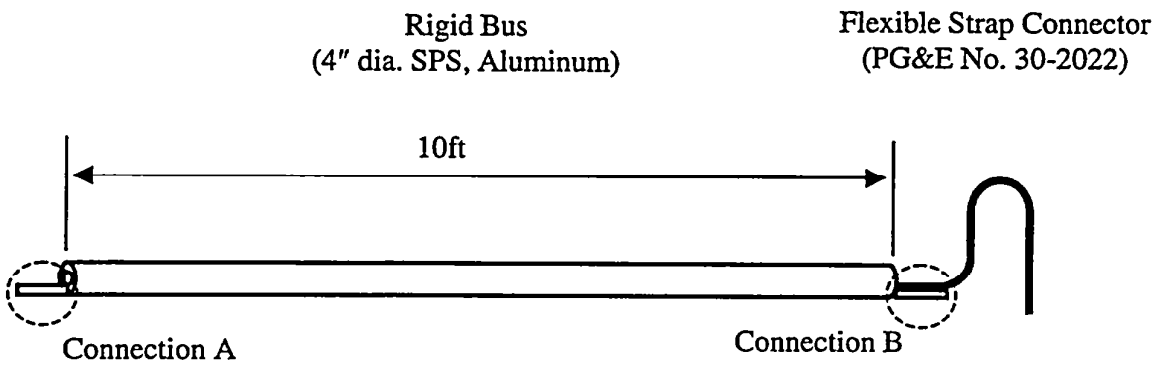

Figure 2.3 Rigid bus with an asymmetric flexible strap connector

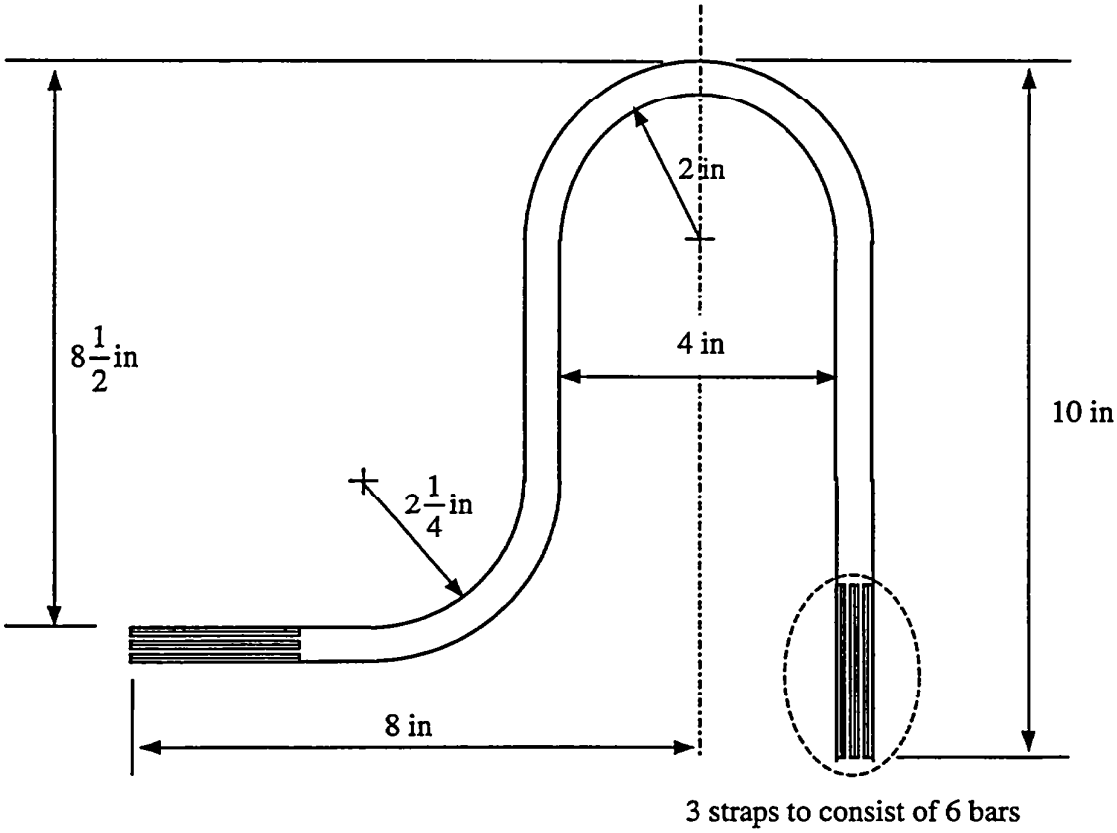

Figure 2.4 Dimensions of FSC No. 30-2021

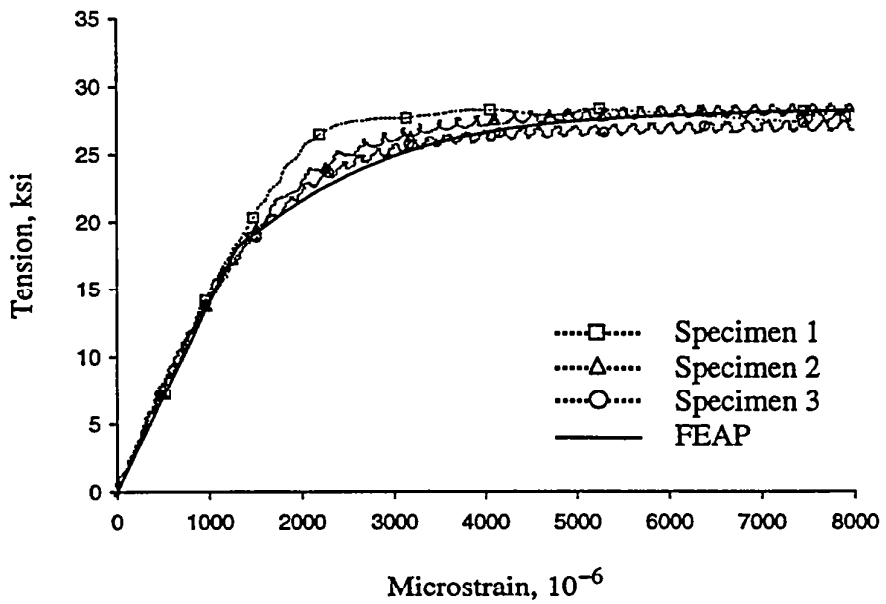

Figure 2.5 Comparison of uniaxial tensile stress-strain relationship of FSC coupons generated in the UCSD tests with fitted model

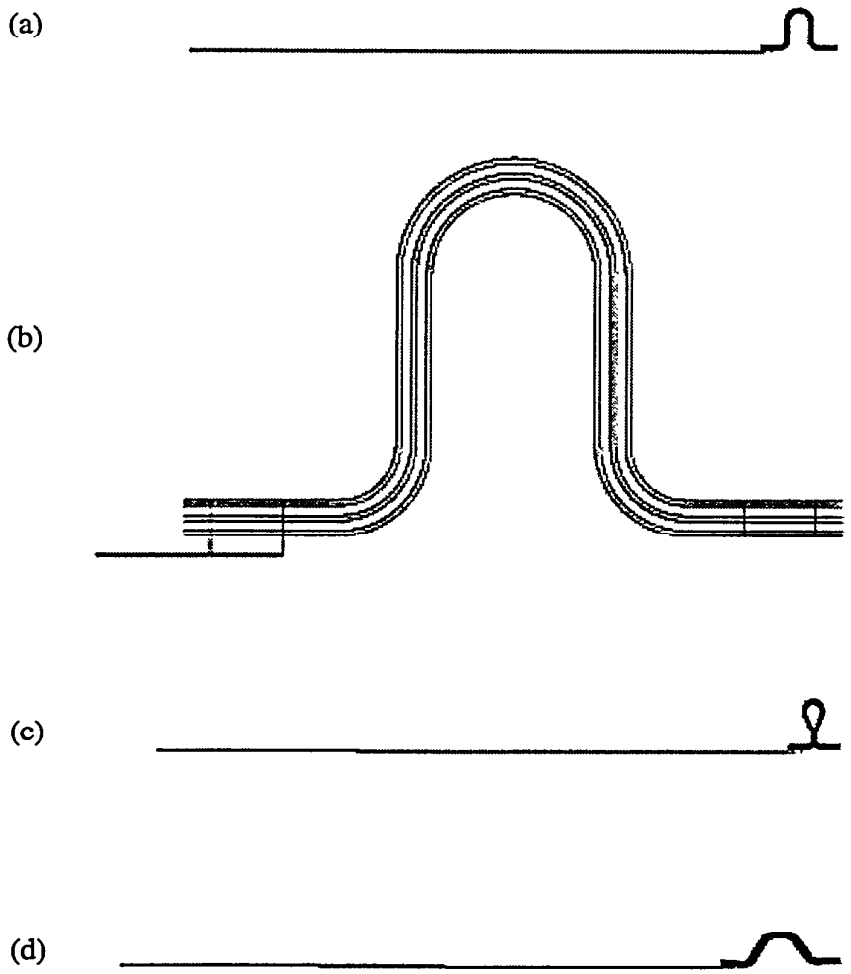

Figure 2.6 Schematics of the finite element layout of the RB with symmetric FSC: (a) frame elements for the RB-FSC, (b) frame elements for the FSC, (c) extreme deformed shape under compression, and (d) extreme deformed shape under tension

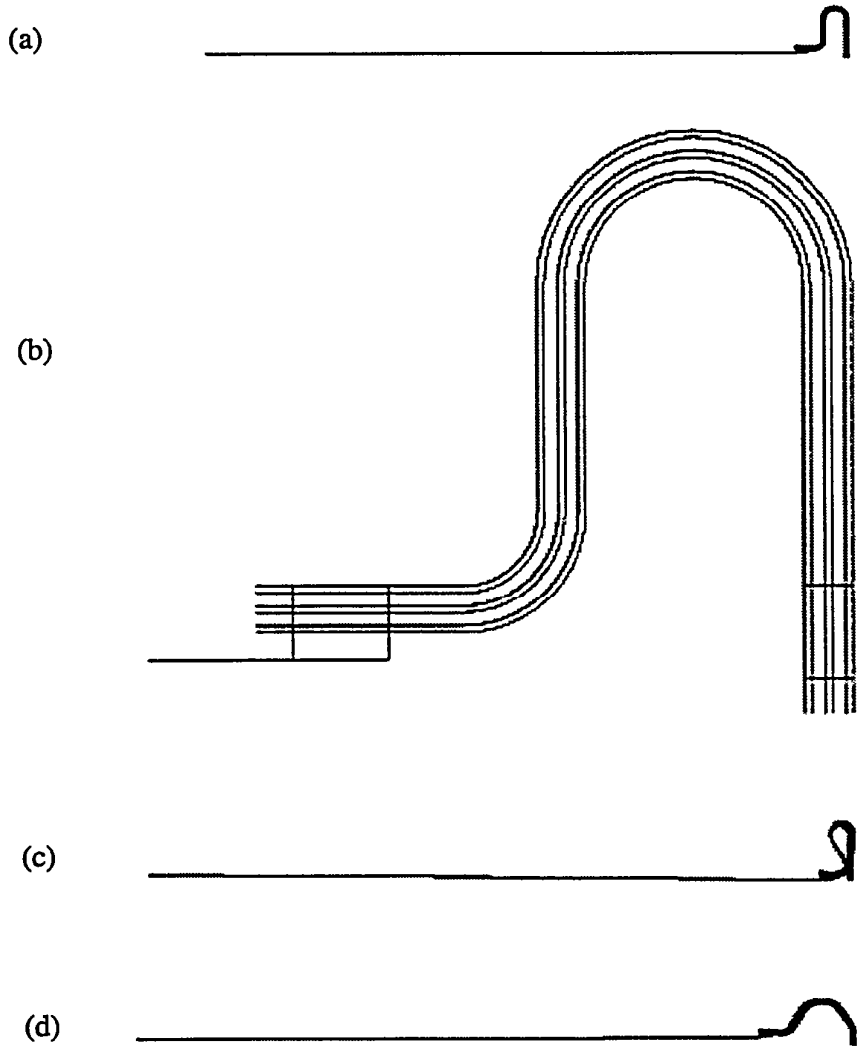

Figure 2.7 Schematics of the finite element layout of the RB with asymmetric FSC: (a) frame elements for the RB-FSC, (b) frame elements for the FSC, (c) extreme deformed shape under compression, and (d) extreme deformed shape under tension

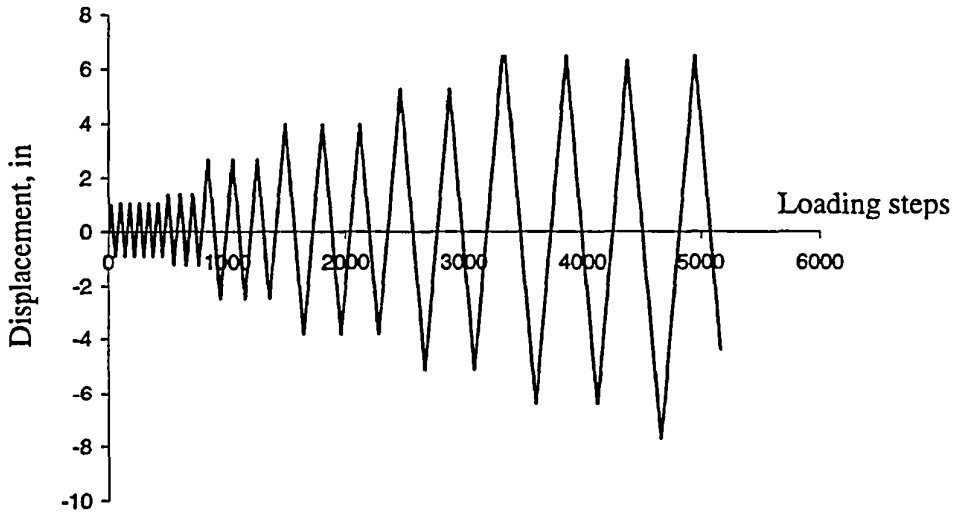

Figure 2.8 History of imposed support displacement used in the UCSD test

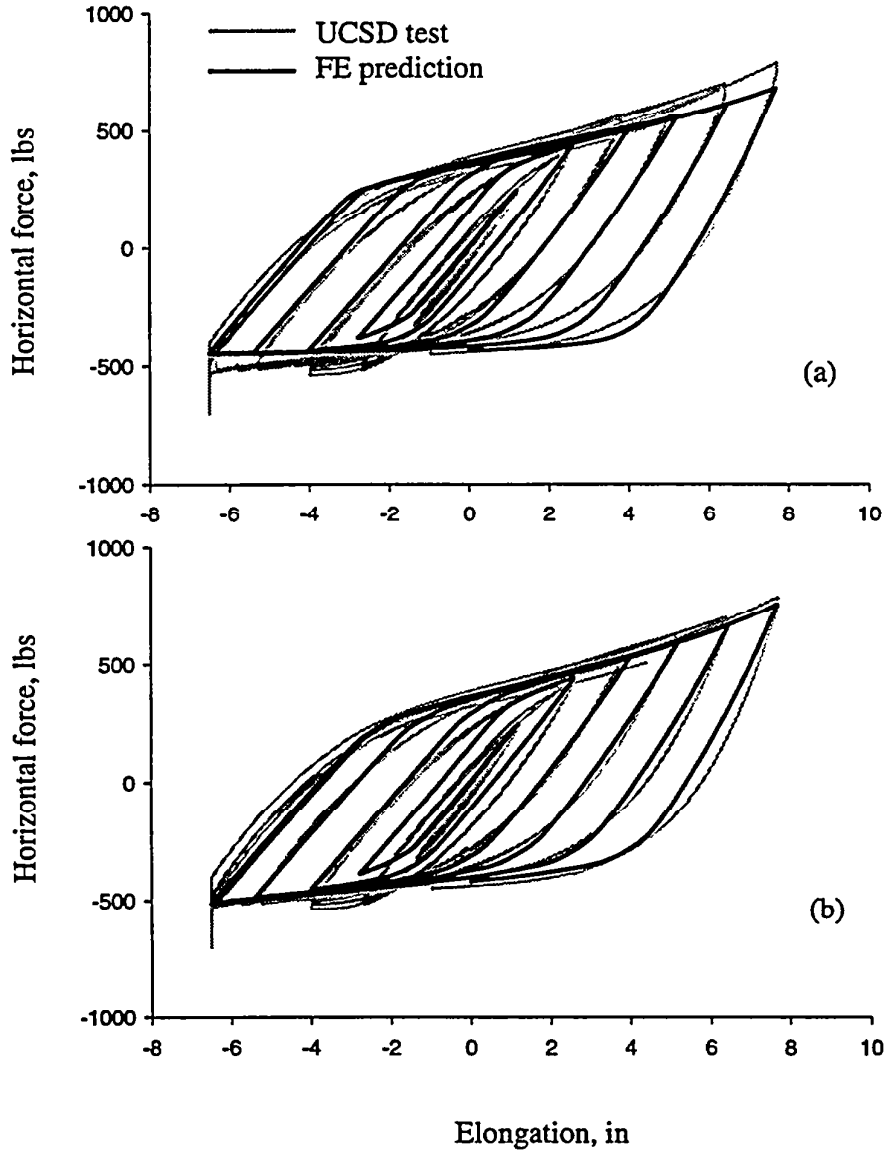

Figure 2.9 Comparison of FE predicted force-elongation relationship of the RB with the symmetric FSC with UCSD test results: (a) $H_{kin} = E/100$, (b) $H_{kin} = E/20$

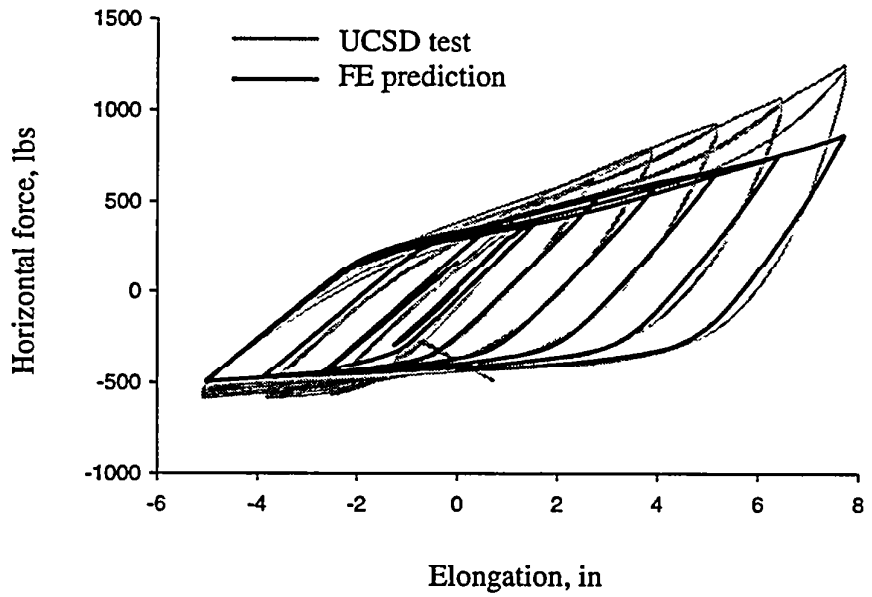

Figure 2.10 Comparison of FE predicted force-elongation relationship of the RB with the asymmetric FSC with UCSD test results for $H_{kin} = E/20$

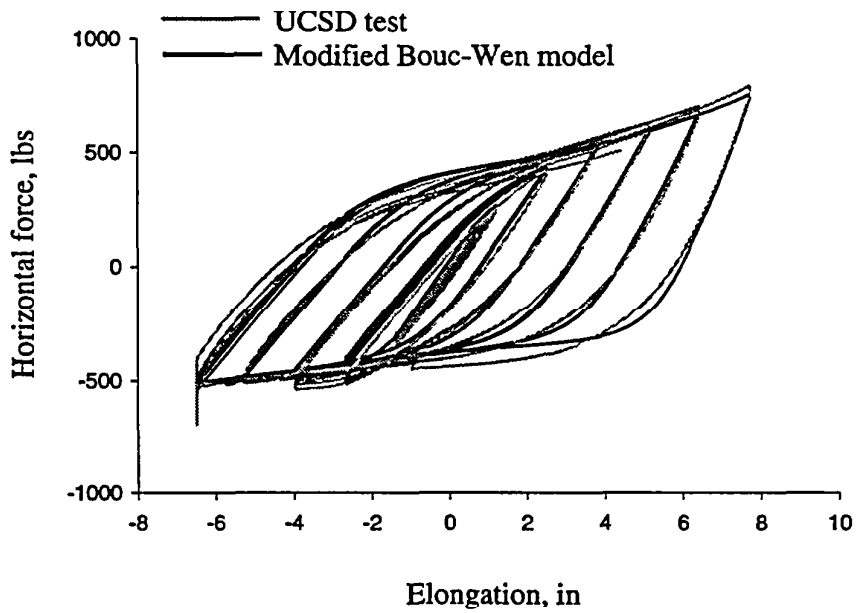

Figure 2.11 Force-elongation relationship of the first RB with symmetric FSC obtained from the UCSD test and from the modified Bouc-Wen model

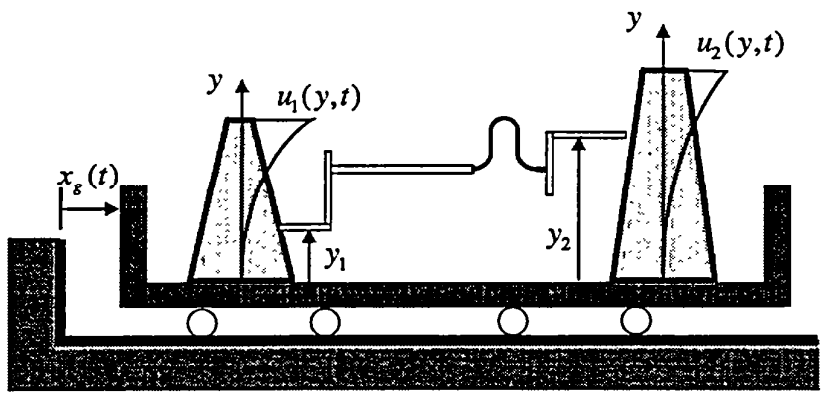

Figure 2.12 Model of equipment items connected by a RB-FSC

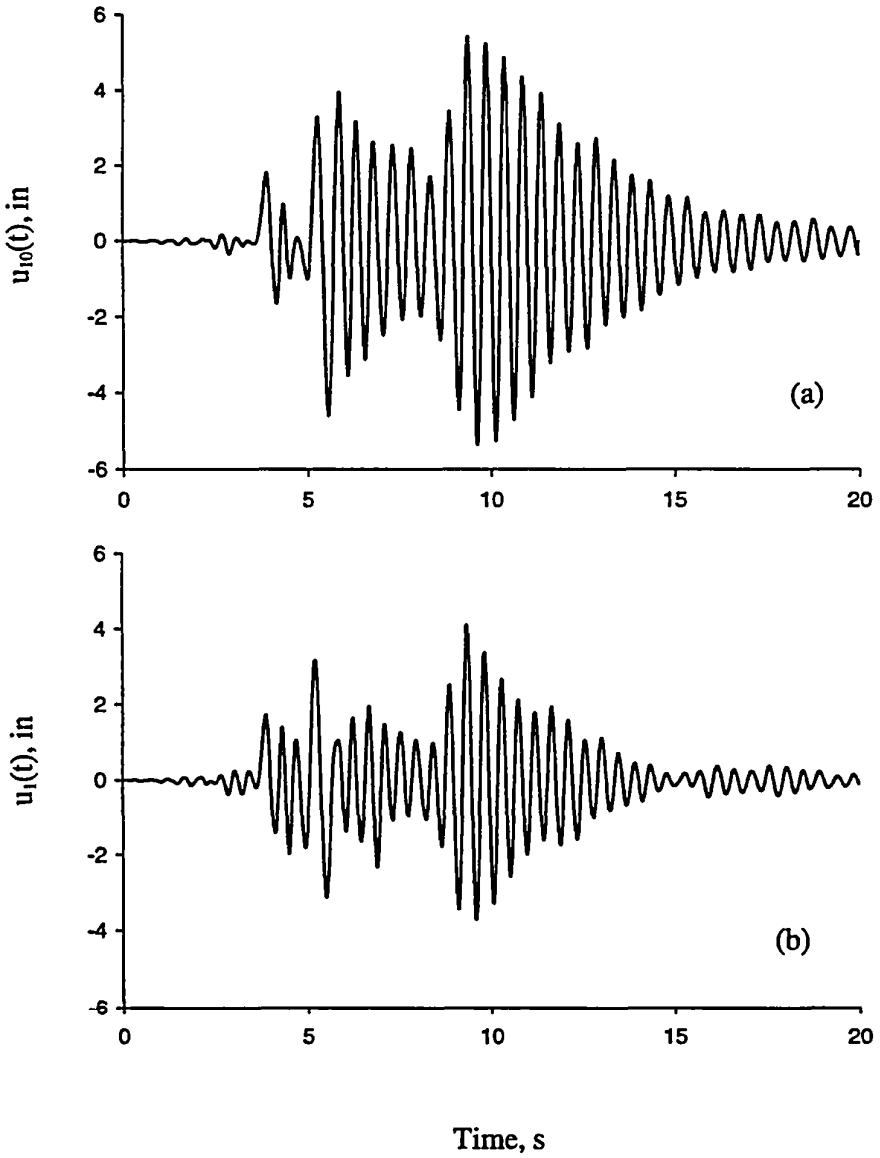

Figure 2.13 Displacement time histories of the lower-frequency equipment item for the Newhall-Northridge record: (a) response in the stand-alone configuration and (b) response in the connected system

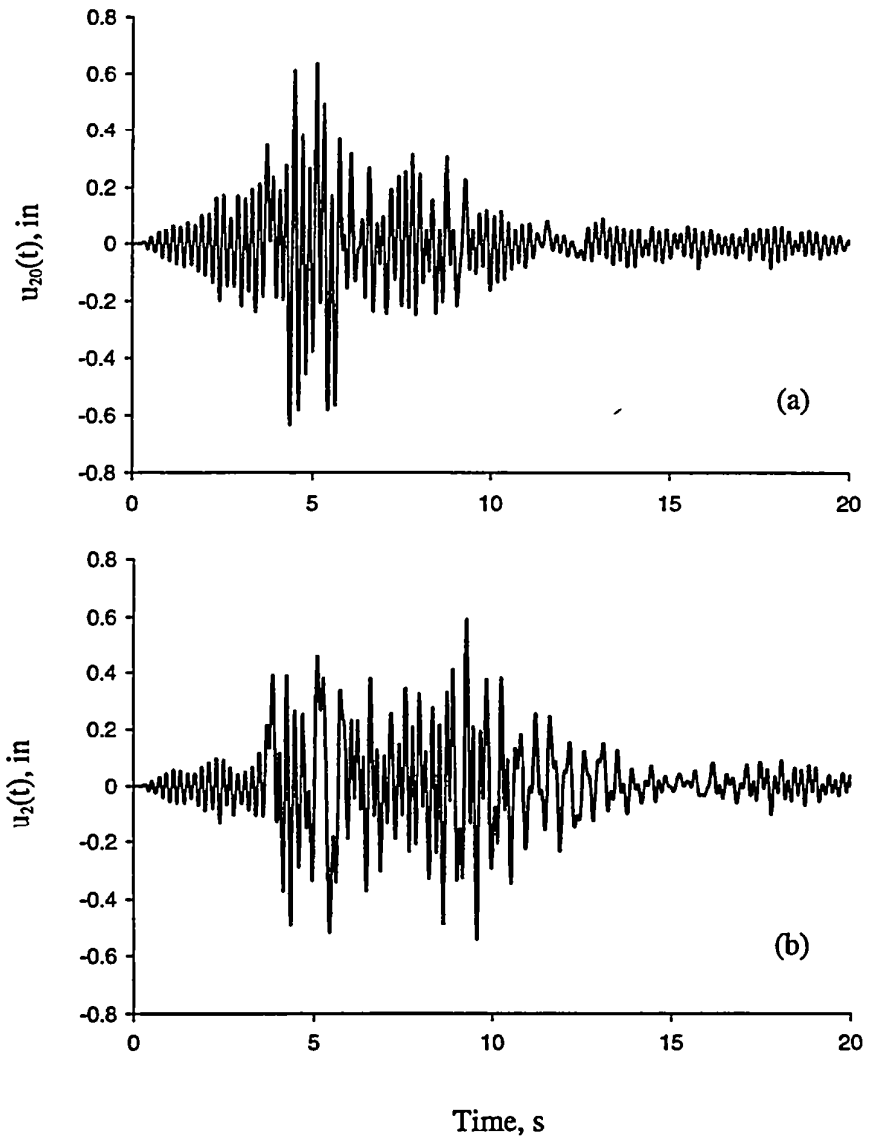

Figure 2.14 Displacement time histories of the higher-frequency equipment item for the Newhall-Northridge record: (a) response in the stand-alone configuration and (b) response in the connected system

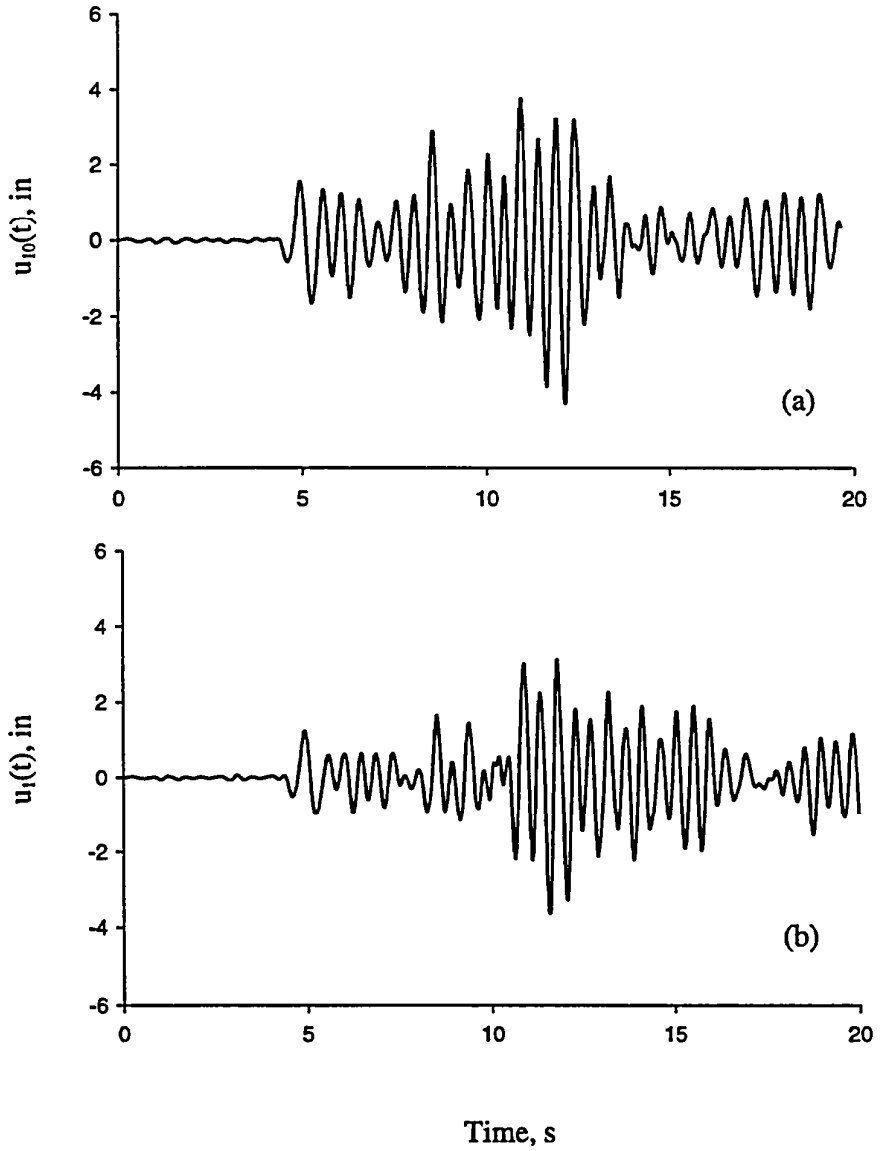

Figure 2.15 Displacement time histories of the lower-frequency equipment item for the TabasLN record: (a) response in the stand-alone configuration and (b) response in the connected system

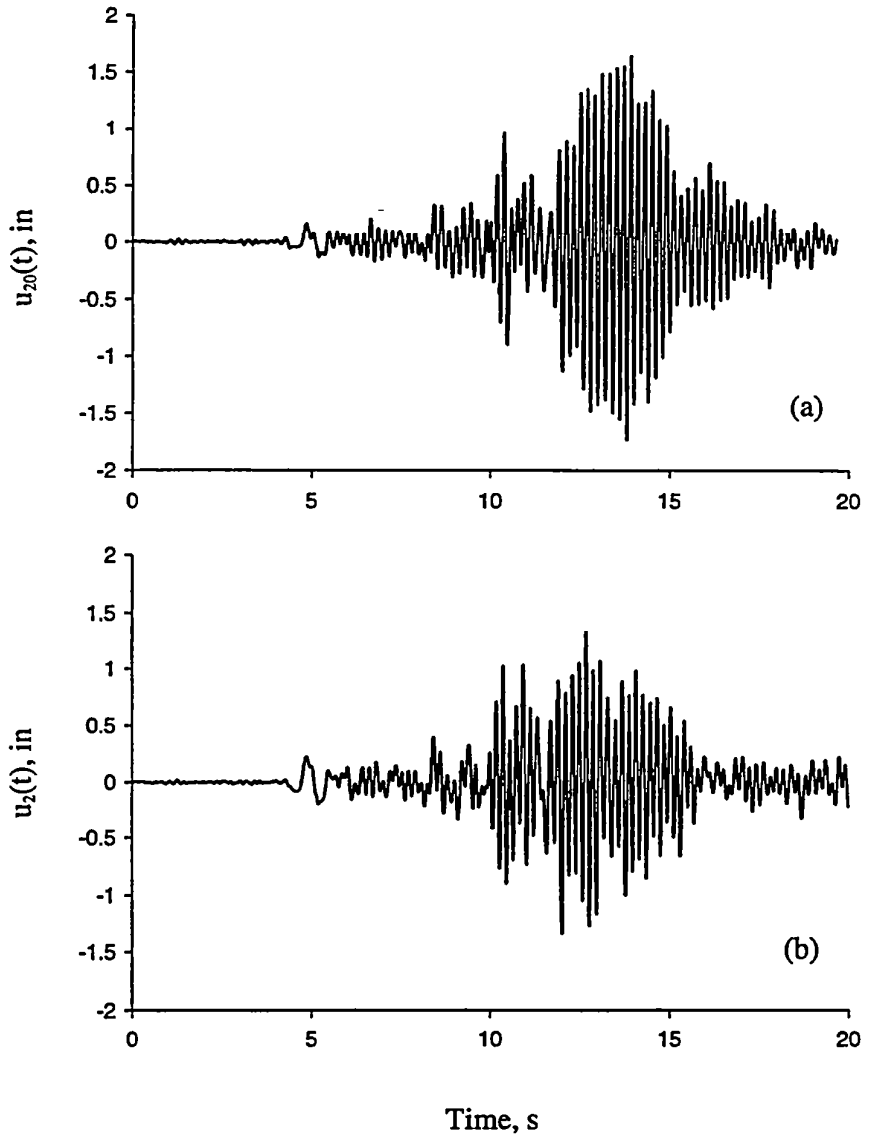

Figure 2.16 Displacement time histories of the higher-frequency equipment item for the TabasLN record: (a) response in the stand-alone configuration and (b) response in the connected system

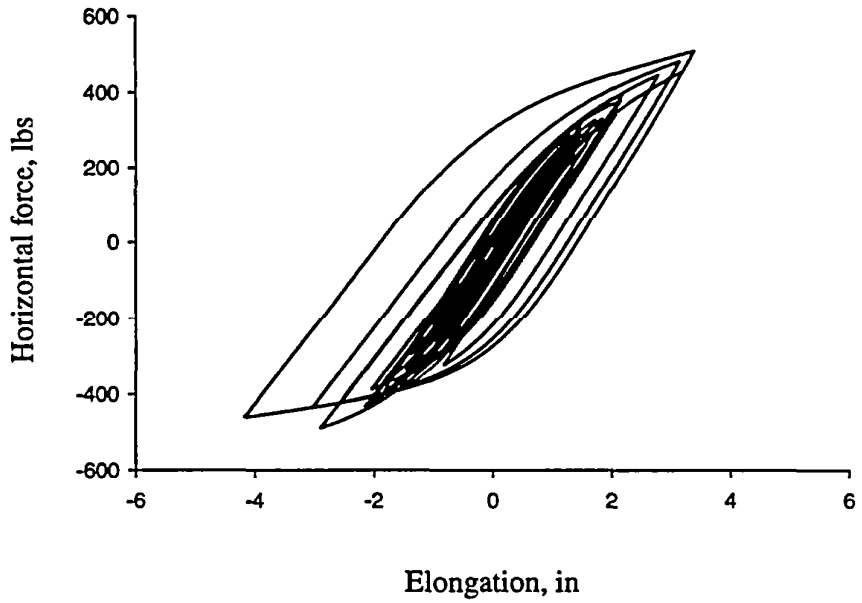

Figure 2.17 Force-elongation hysteresis loops of the RB-FSC in the connected system subjected to the Newhall-Northridge record

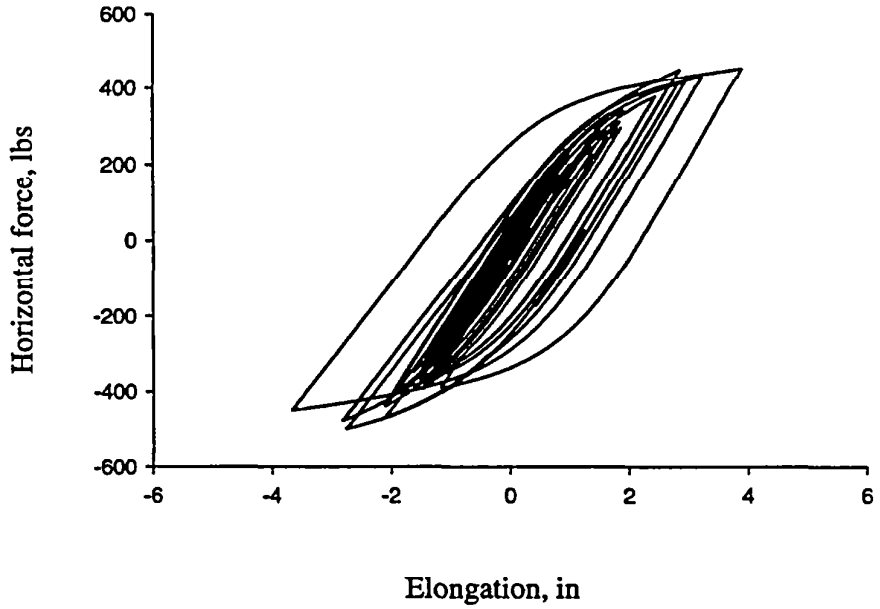

Figure 2.18 Force-elongation hysteresis loops of the RB-FSC in the connected system subjected to the TabasLN record

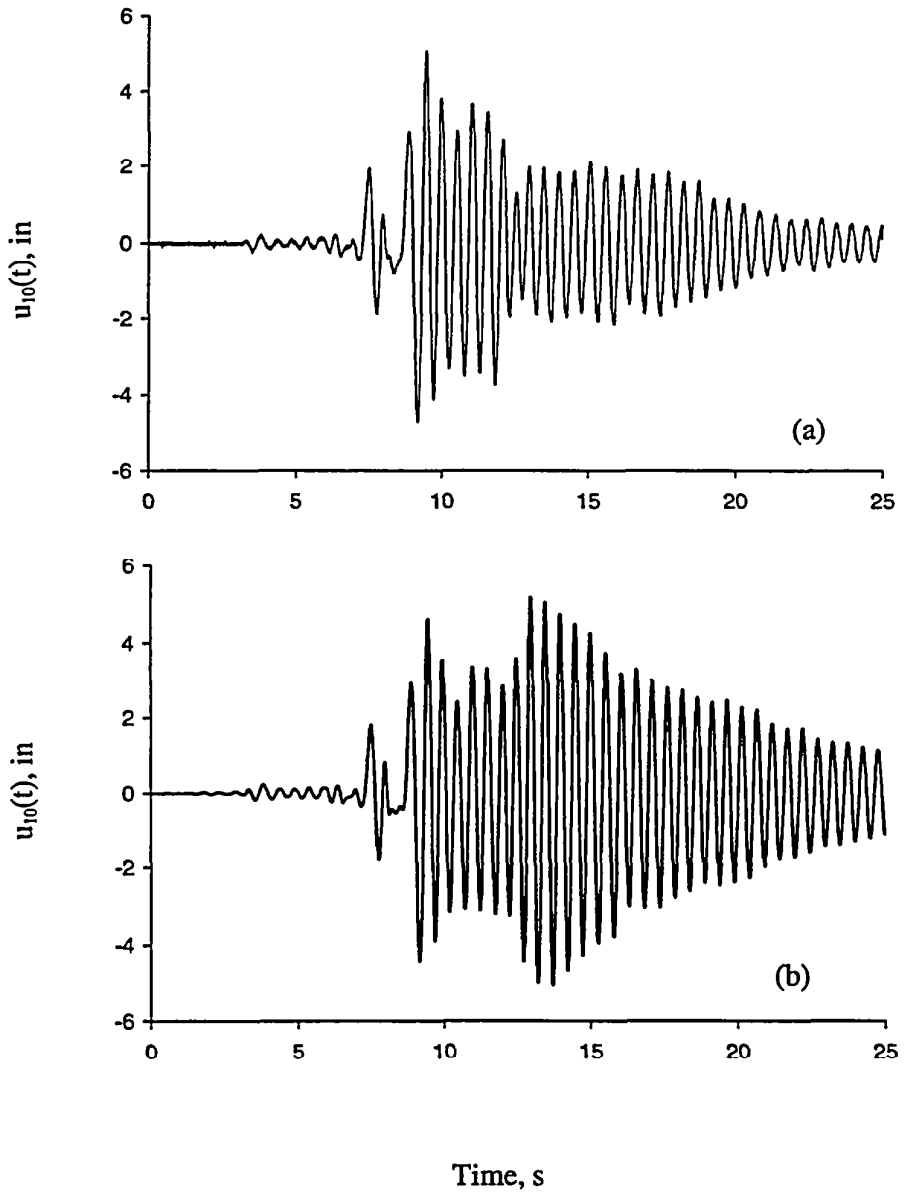

Figure 2.19 Displacement time histories of the lower-frequency equipment item in the stand-alone configuration for the table motion TRB127 (Newhall 100%): (a) experiment and (b) analysis

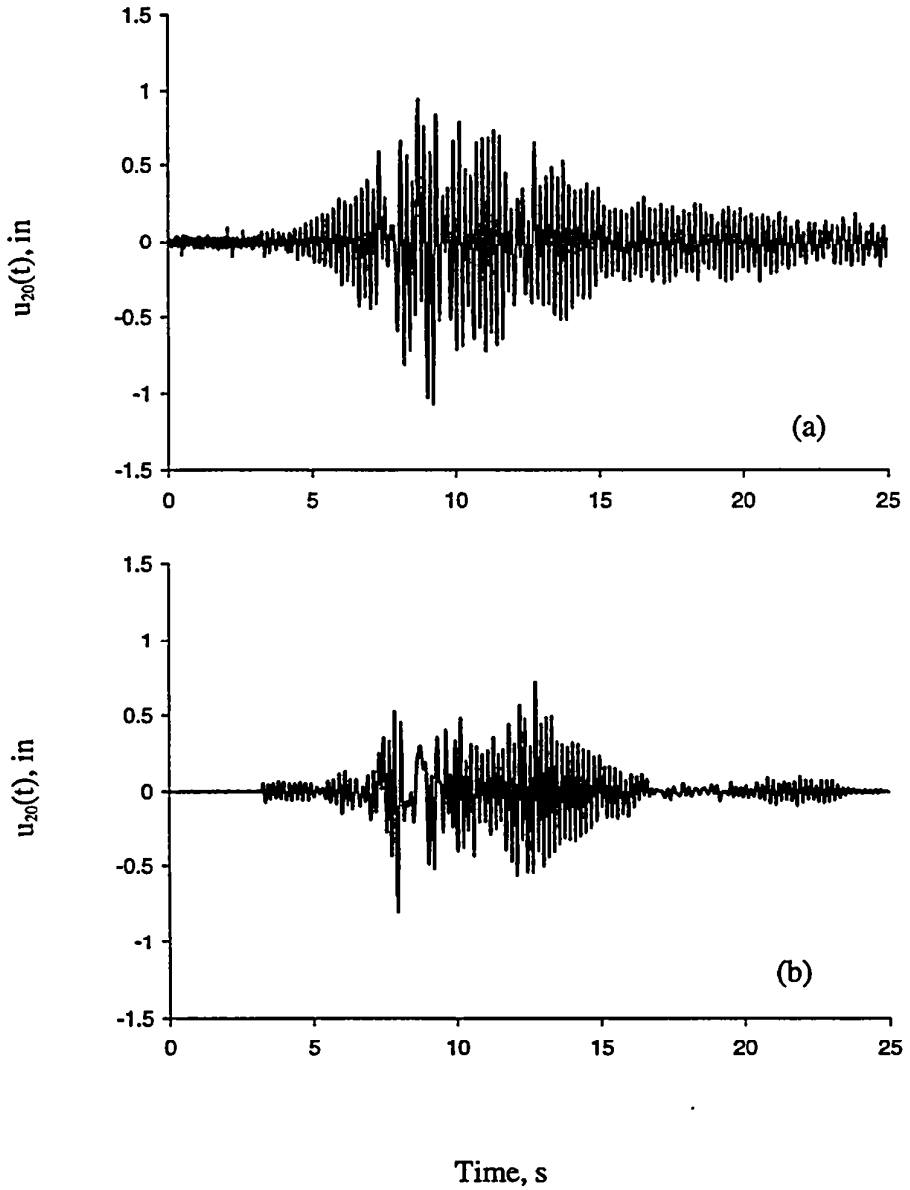

Figure 2.20 Displacement time histories of the higher-frequency equipment item in the stand-alone configuration for the table motion TRB127 (Newhall 100%): (a) experiment and (b) analysis

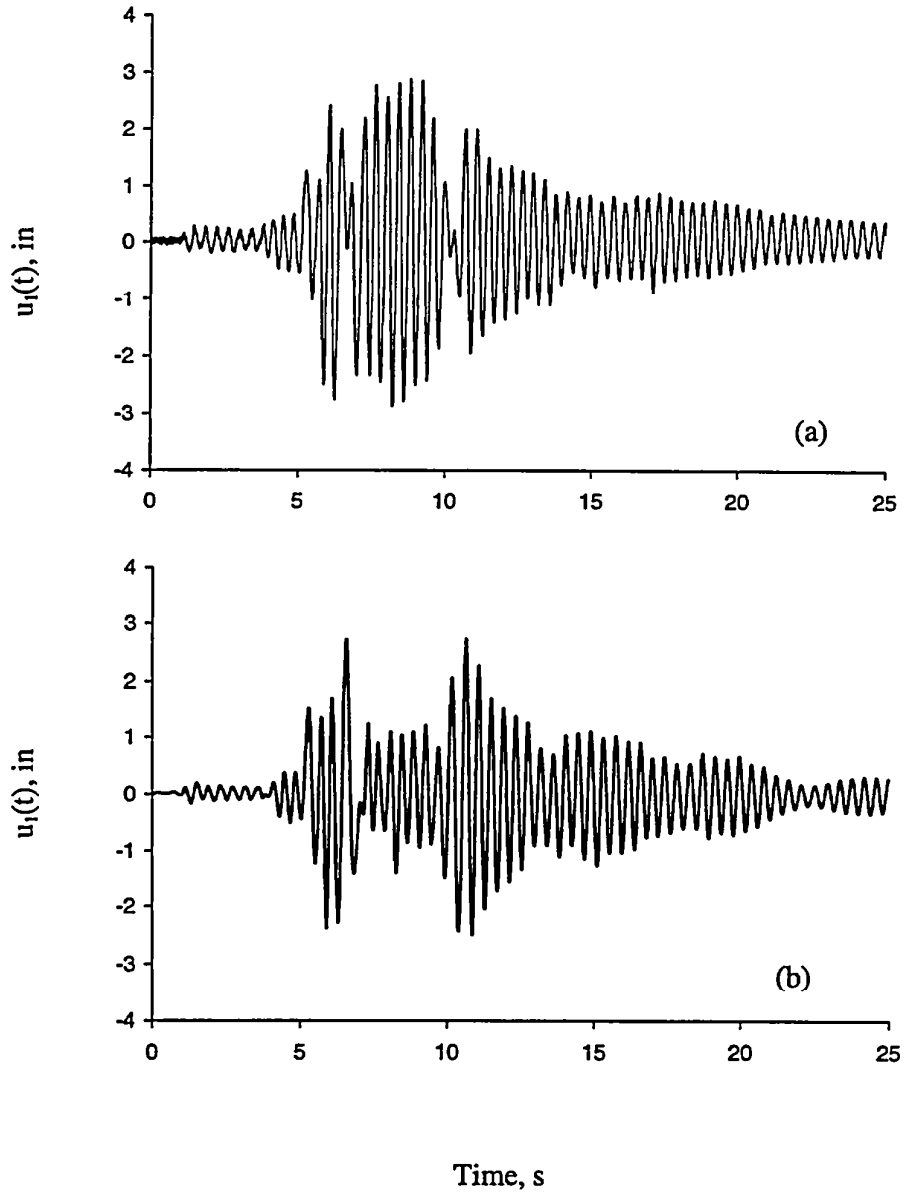

Figure 2.21 Displacement time histories of the lower-frequency equipment item in the connected system for the table motion TRB101 (Newhall 100%): (a) experiment and (b) analysis

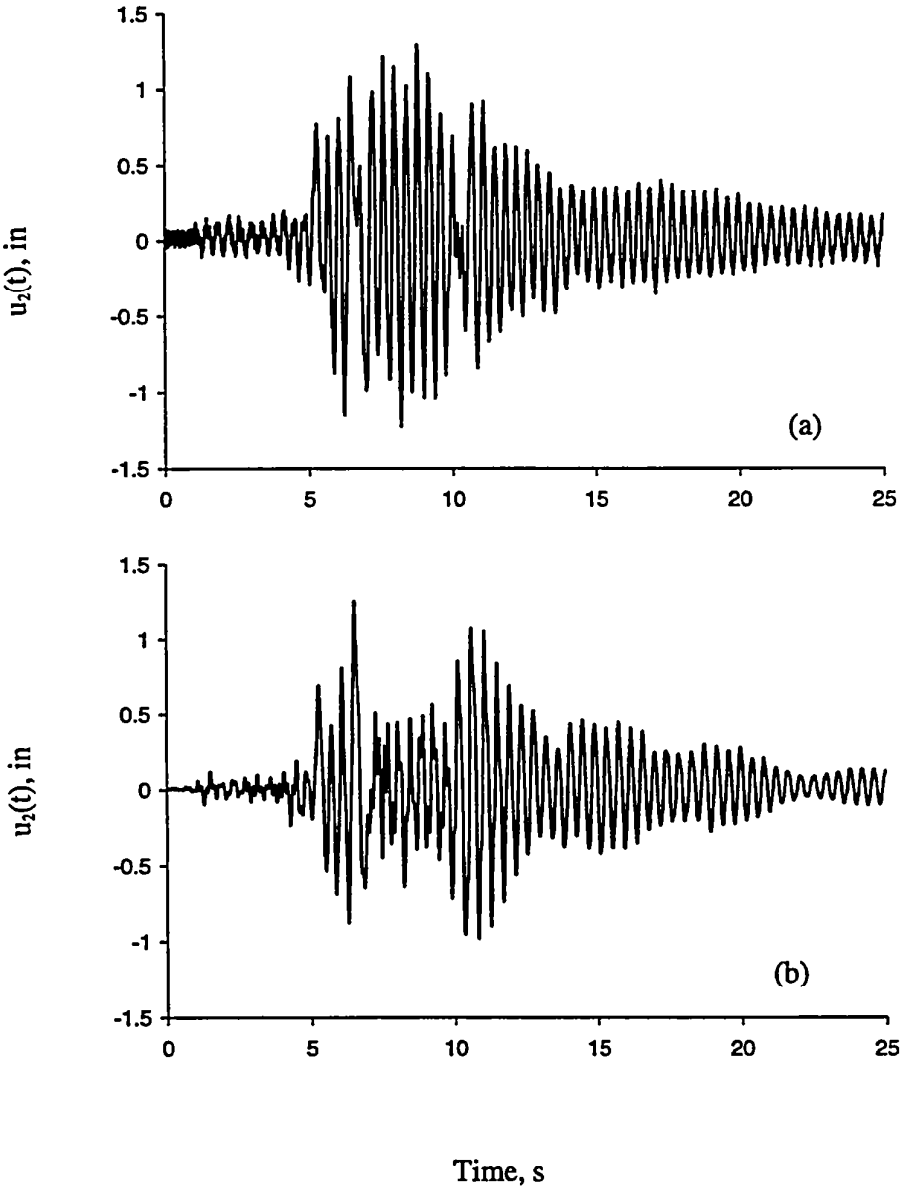

Figure 2.22 Displacement time histories of the higher-frequency equipment item in the connected system for the table motion TRB101 (Newhall 100%): (a) experiment and (b) analysis

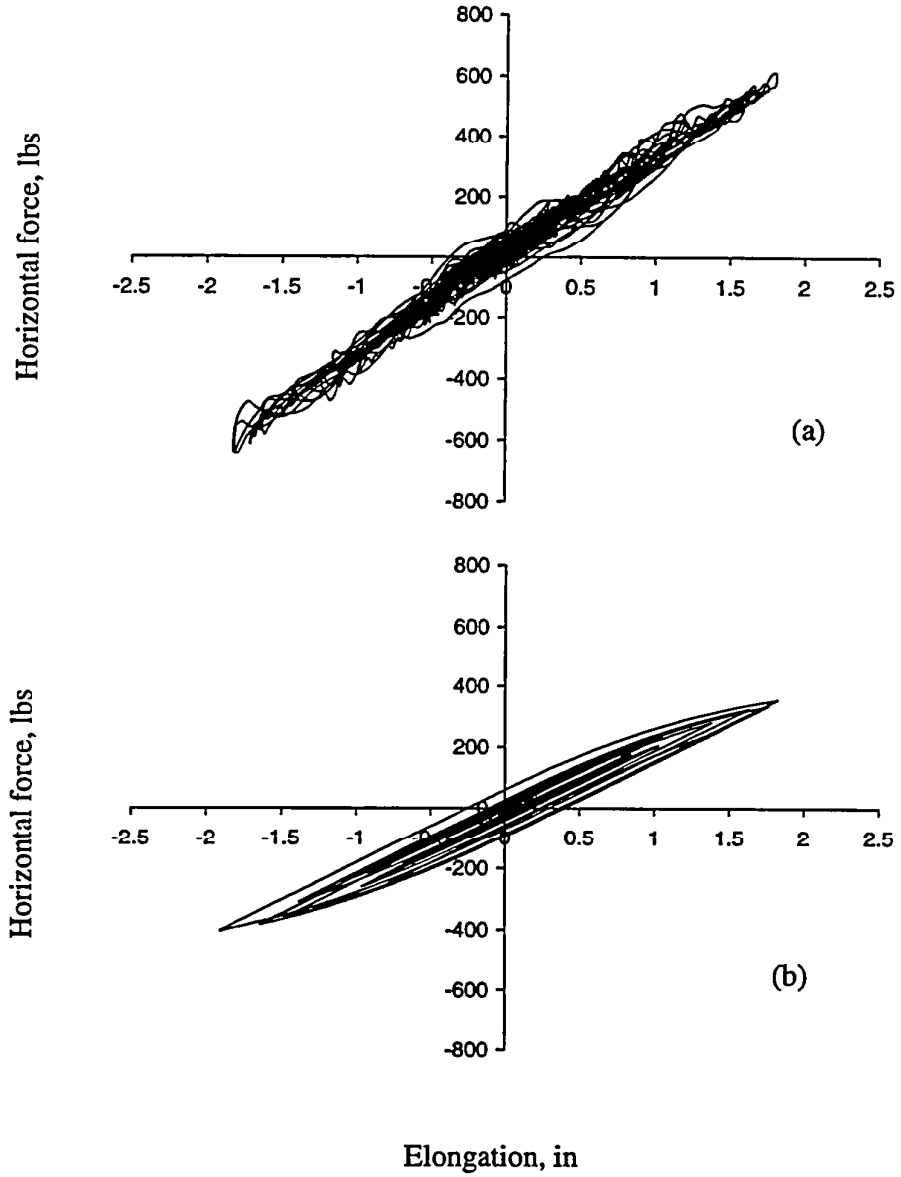

Figure 2.23 Force-elongation hysteresis loops of the RB-FSC in the connected system subjected to the table motion TRB101 (Newhall 100%): (a) experiment and (b) analysis

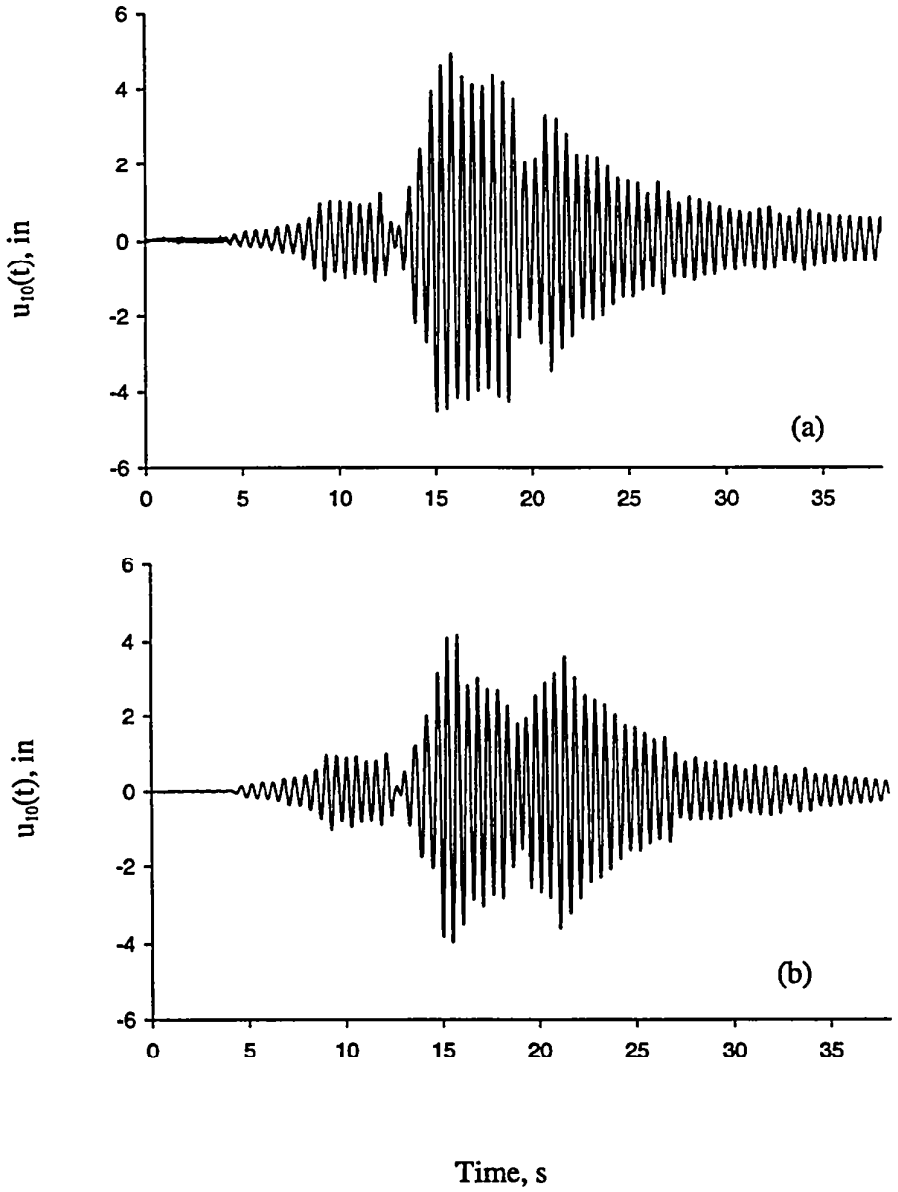

Figure 2.24 Displacement time histories of the lower-frequency equipment item in the stand-alone configuration for the table motion TRB126 (Tabas 50%): (a) experiment and (b) analysis

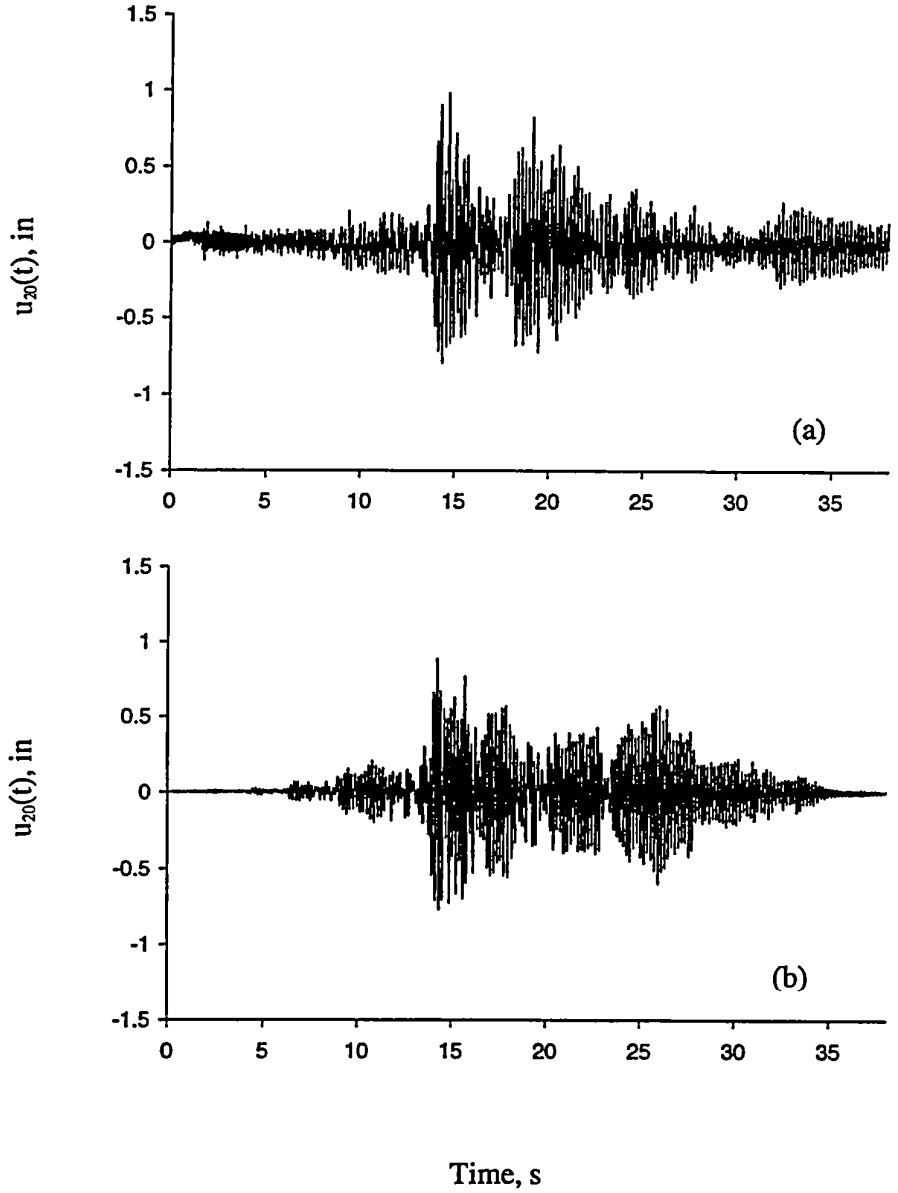

Figure 2.25 Displacement time histories of the higher-frequency equipment item in the stand-alone configuration for the table motion TRB126 (Tabas 50%): (a) experiment and (b) analysis

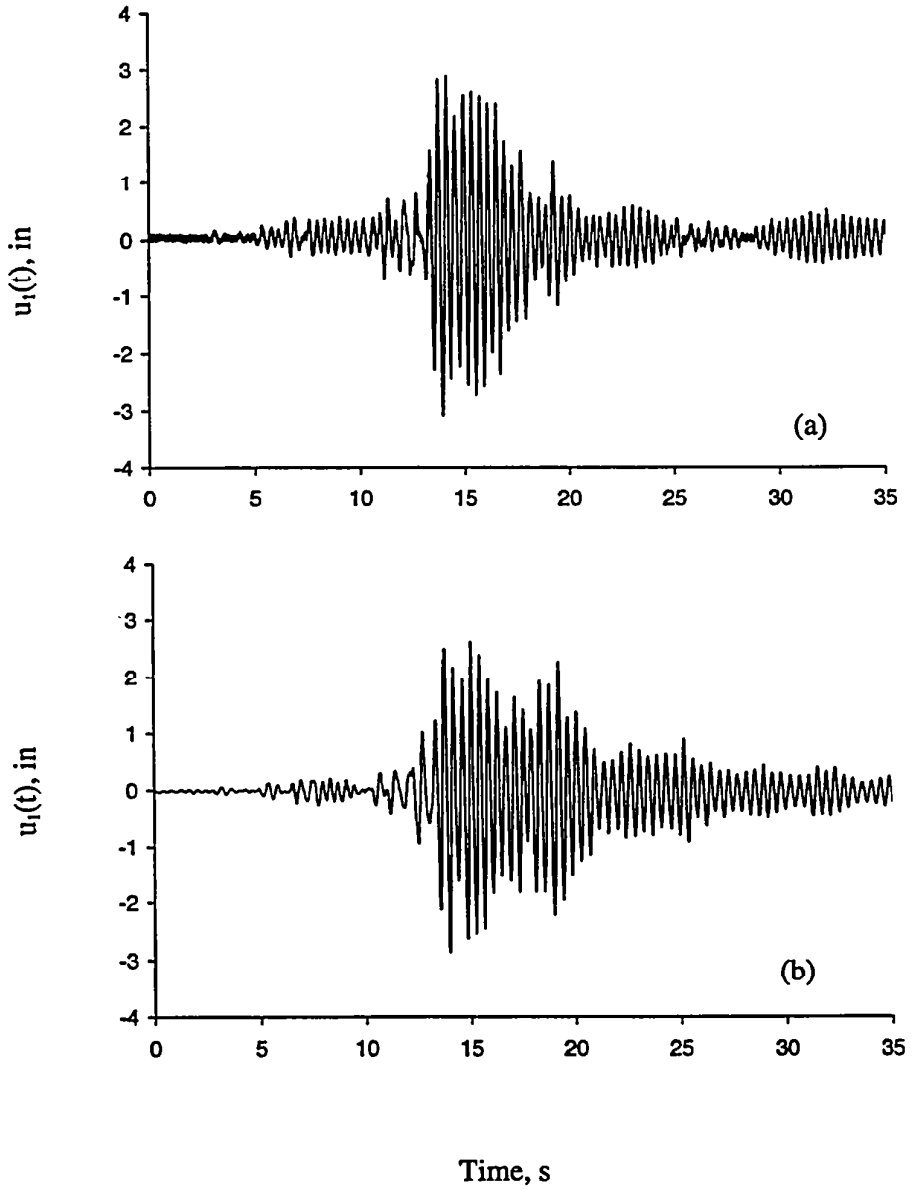

Figure 2.26 Displacement time histories of the lower-frequency equipment item in the connected system for the table motion TRB100 (Tabas 50%): (a) experiment and (b) analysis

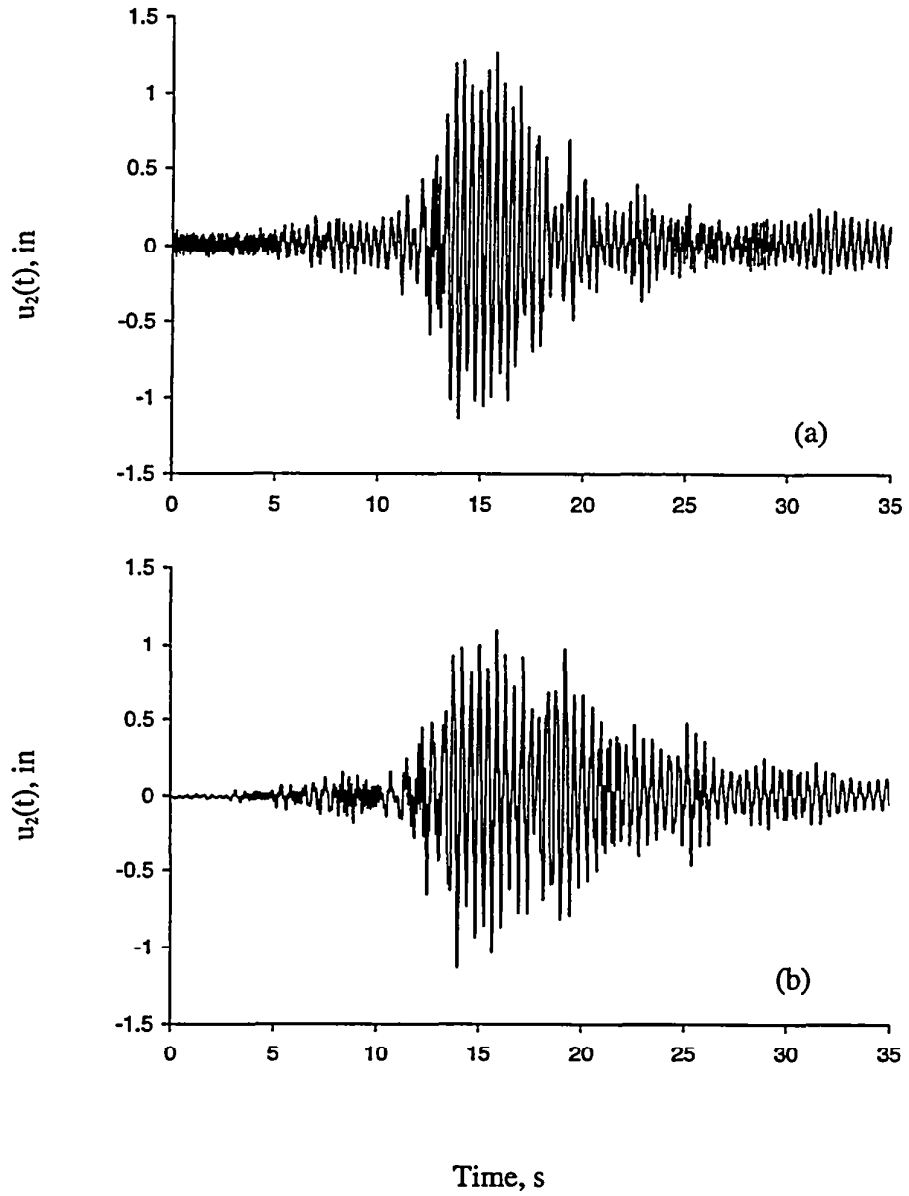

Figure 2.27 Displacement time histories of the higher-frequency equipment item in the connected system for the table motion TRB100 (Tabas 50%): (a) experiment and (b) analysis

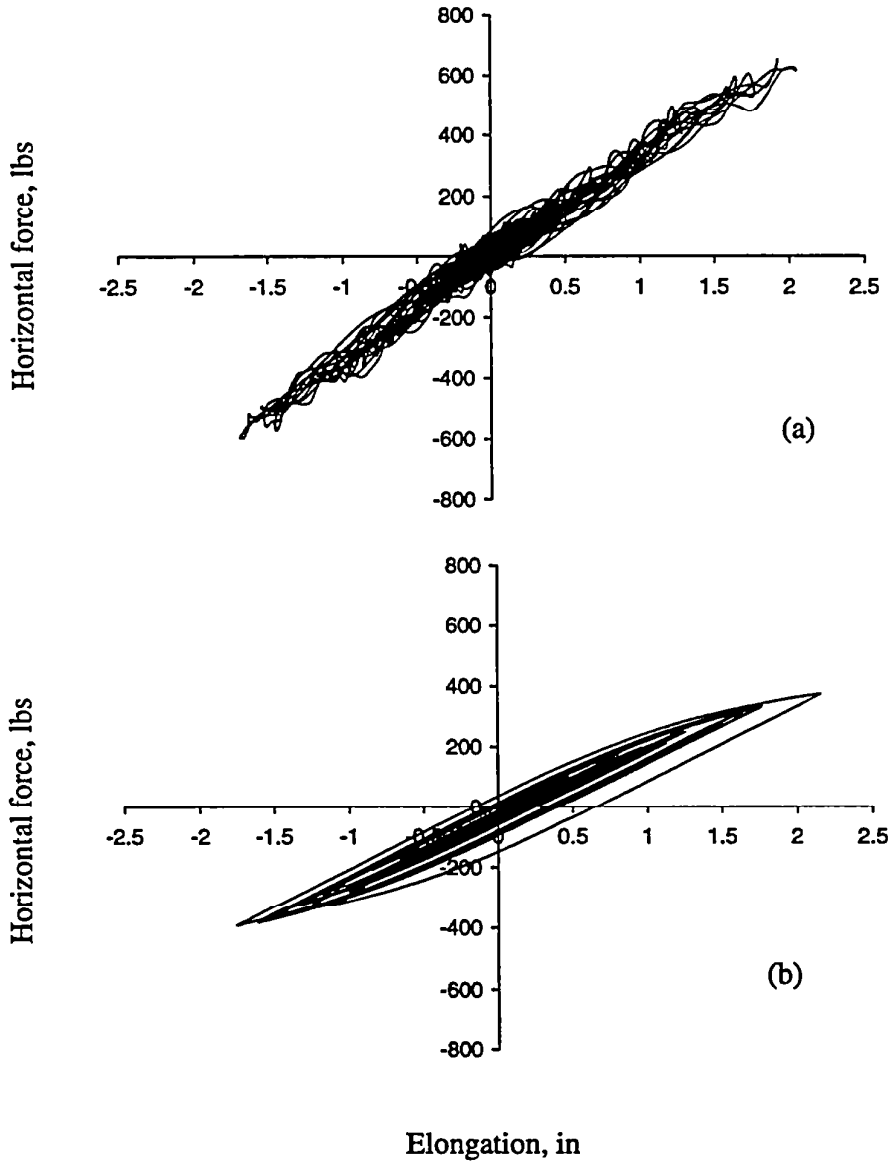

Figure 2.28 Force-elongation hysteresis loops of the RB-FSC in the connected system subjected to the table motion TRB100 (Tabas 50%): (a) experiment; and (b) analysis

Chapter 3 Influence of the Bending Stiffness and Inertia of the Connecting Cable on the Interaction Effect

3.1 Introduction

Many equipment items in electrical substations are connected to each other by flexible conductors, typically cables made of braided aluminum wire strands. In our previous study (Der Kiureghian et al., 1999), we investigated the effect of interaction in such systems when the flexible conductor was considered to be an extensible cable with negligible flexural rigidity and inertia effects. Under these approximations, the flexible conductor was modeled as an extensible catenary cable and closed form expressions were derived for its effective stiffness as a function of its geometry, i.e., span length, vertical separation of the supports, cable length, its weight per unit length w, and its axial rigidity EA, where E denotes the Young's modulus and A is the cross-sectional area of the cable. Extensive parametric studies using time history analyses with recorded ground motions were carried out to determine the effect of interaction on two equipment items connected by such a cable. It was found that, depending on the equipment characteristics and the selected ground motion, the response of both equipment items could be strongly amplified (in relation to their stand-alone responses) when the cable has a small sag. To quantify the needed sag in order to avoid a large response amplification, the response ratios R_1 and R_2 (see their definitions in (2.21)) were computed as functions of the "interaction" parameter β defined as

$$\beta = \frac{\Delta \cdot L_0 / c_0^2}{s_0 / c_0 - 1} \tag{3.1}$$

In this formula, L_0 denotes the initial span of the cable, $c_0 = \sqrt{L_0^2 + H^2}$ is the initial chord length of the cable, in which H denotes the vertical separation between the supports, s_0 denotes the cable length under the initial static equilibrium conditions, and Δ denotes the maximum relative displacement between the stand-alone equipment items for the specified ground motion. Investigations with five different ground motions and several equipment configurations revealed that there is virtually no interaction between the equipment items when β is less than about 1. Based on this finding, the minimum required cable length to avoid the adverse interaction effect was determined to be

$$s_0 = c_0 + \frac{L_0}{c_0}\Delta \tag{3.2}$$

A procedure for estimating the maximum relative displacement Δ for a specified ground motion in terms of a specified response spectrum was described in our previous study.

After completion of our previous study, we came across a paper by Dastous and Pierre (1996) that described experimental results on flexible conductors subjected to imposed horizontal harmonic excitation either at one end or out-of-phase motions at both ends. The paper argued that these experiments were relevant to the equipment interaction problem, since the response of each equipment item in the connected system would tend to be essentially in first mode and, thus, well represented by an harmonic motion. This experimental study revealed a significant effect on the cable forces arising from the inertia of the cable mass in the vertical direction. Compared to the results based on quasi-static analysis, the horizontal force in the cable could be amplified by several orders of magnitude when end motions were applied at certain frequencies. Furthermore, significant compression forces developed in the cable, thus indicating the potential importance of the flexural rigidity. These results suggest that the effect of interaction in cable-connected equipment items can be greater than that indicated in our previous study, which ignored the inertia and flexural rigidity of the cable. Furthermore, the minimum required cable length given in (3.2) may not be sufficient to avoid the adverse effect of interaction, when inertia and flexural stiffness effects are present.

The aim of the present study is to re-examine the effect of interaction in cable-connected equipment items while accounting for the cable inertia and flexural rigidity. A finite element approach using truss and frame elements with a Lagrangian strain formulation is used to properly account for the geometric nonlinearity in the response. In order to validate the finite element model, first comparisons are made with our previous results for the catenary cable under static loads without including the flexural rigidity effect. Next, comparisons are made with the experimental results of Dastous and Pierre (1996) for a cable subjected to out-of-phase end motions. Reasonable qualitative agreement between the finite element and experimental results is obtained. In the final section of the chapter, the cable-connected equipment system is modeled and numerical time history analyses for the set of five earthquake ground motions from our previous study are carried out to determine the interaction effect. The results indicate that cable inertia and flexural rigidity have small influences for relatively taut cables. For cables with larger sag, the cable inertia and flexural rigidity tend to amply the interaction effect for certain ground motions. However, these amplifications are not as dramatic as anticipated from the discussion in the paper by Dastous and Pierre (1996). Evidently, the interaction between the equipment items and the cable in the case of an imposed ground motion significantly alters the dynamic response of the cable from that of a cable subjected to imposed end motions. While a definitive criterion for minimum slackness cannot be given at this time due to the limited number of ground motions studied, a preliminary recommendation is provided.

3.2 Section Properties of the Flexible Conductor

In order to develop a finite element model of the flexible conductor, it is necessary to describe the axial and flexural rigidity of the conductor at each section. As mentioned earlier, the flexible conductor is typically a cable made of braided strands of aluminum wire. The two ends of the cable usually are attached to the equipment items through welded aluminum connectors so that no unwrapping of the strands is possible. For the following discussion, we let n denote the number of strands and d denote the diameter of each strand.

When the cable is subjected to a tension force, it is conceivable that some tightening of the braids will occur before the full axial stiffness of the strands is developed. Likewise, when a segment of the cable is subjected to compression, opening of the braids or even buckling of the outer strands may occur. These imply that the axial stiffness of the cable for a small tension force or a large compression force could be smaller than the sum of the axial stiffnesses of the individual strands. We are not aware of any experiments that have investigated these effects. For the sake of simplicity, in the following analysis we ignore these effects and assume that the effective cross-sectional area of the cable throughout its length is a constant and is equal to the sum of cross-sectional areas of the strands, i.e.,

$$A = \frac{n\pi d^2}{4} \tag{3.3}$$

The flexural rigidity of the cable at a cross section is given by the product EI, where I denotes the section moment of inertia. The value of I depends on whether the strands at the cross section remain attached or slide with respect to one another as the cable is bent. The minimum value of the moment of inertia, denoted $I_{\min}$, is obtained by assuming that the strands freely slide against one another. In that case the moment of inertia is simply the sum of the moments of inertia of the individual strands and is given by

$$I_{\min} = \frac{n\pi d^4}{64} \tag{3.4}$$

In the actual system, significant friction forces may develop between the strands, particularly at locations where the cable has a strong curvature and is under tension. These friction forces may prevent sliding of some of the strands and, hence, a larger effective moment of inertia may develop. The maximum value of I is obtained when all strands remain attached and is given by

$$I_{\max} = \sum_{i=1}^{n} \frac{\pi d^2}{4}\left(\frac{d^2}{16} + y_i^2\right) \tag{3.5}$$

where y_i is the distance of the i-th strand from the neutral axis, as shown in Figure 3.1. The actual moment of inertia of the cable is somewhere between the above two extremes.

Furthermore, the moment of inertia would tend to vary along the cable depending on the cable curvature and the force magnitude. Unfortunately the two bounding values in (3.4) and (3.5) are widely apart for typical cables used in the power industry. For example, for a 1796-MCM cable consisting of 61 strands in 5 layers, the upper bound in (3.5) is about 80 times the lower bound in (3.4). Based on experiments conducted by BC Hydro in the 1990's, a recent IEEE guideline (IEEE 1999) recommends the use of the approximation

$$I \cong (1+N)I_{\min} \tag{3.6}$$

for short length aluminum conductors, where N denotes the number of layers of strand. In the following analyses, unless stated otherwise, this approximation is employed. Furthermore, it is assumed that the moment of inertia remains constant throughout the length of the cable at all times. A parametric study is performed to investigate the sensitivity to the assumed value of the moment of inertia. Unfortunately, the large uncertainty associated with this characteristic of the cable will prevent us from making predictions of the cable response that are in close quantitative agreement with the experimental results of Dastous and Pierre.

For the subsequent analysis, it is also necessary to assign a value to the Young's modulus. IEEE guidelines (IEEE 1999) recommend $E = 5.72\times10^6\,\mathrm{N/cm^2}$ ($=8.30\times10^6$ psi) for all-aluminum conductors. Unless stated otherwise, this value is used in the subsequent analyses.

3.3 Finite Element Model of the Cable

The dynamic analysis of a taut cable with large displacements and rotations is a highly nonlinear elastodynamic problem that has no known analytical solution. Even a numerical solution of this problem is challenging. During the dynamic response, whenever the cable is fully stretched the axial stiffness dominates the cable behavior and significant high-frequency effects are generated. With finite element spatial discretization, these high frequencies may give rise to errors and instability in the numerical computations (Armero and Romero, 1999). Under these conditions, the Newmark time-integration algorithm, which we had successfully used in our previous study with the catenary cable (using an exact expression of the cable stiffness, but neglecting inertia and flexural rigid-

ity effects), does not lead to stable, accurate results. Furthermore, the classical Newmark family of algorithms and its variants generally fail to conserve total angular momentum for nonlinear elastodynamics. This is a significant shortcoming, since the angular momentum can have an important influence on the cable dynamics. An algorithm that preserves the conservation laws is presented by Simo et al. (1992). A modified version of this algorithm, by controlling parameters, introduces numerical damping to stabilize the computations while slightly compromising on the conservation of energy. Our experience showed that this algorithm with parameter values $\alpha = 0.55$, $\beta = 0.5$ and $\gamma = 1$ (see Simo et al., 1995, for the definitions of these parameters) and time step $\Delta t = 0.0005$s works successfully for the cable dynamics problem. Hereafter we call this the damped energy-conserving (DEC) algorithm. We note that parameter values $\alpha = 0.5$, $\beta = 0.5$ and $\gamma = 1$ correspond to the energy-conserving algorithm with no numerical damping.

As a test of this algorithm, Figure 3.2 shows plots of the computed and exact responses of two single-degree-of-freedom oscillators subjected to a step loading, as normalized by the corresponding static responses. The top plot is for an oscillator with 5Hz frequency and 2% damping ratio. For this oscillator, the solution based on the DEC algorithm coincides with the exact solution. The bottom plot is for an oscillator with 50Hz frequency and 2% damping ratio. Due to the numerical damping, the solution based on the DEC algorithm in this case shows a slightly faster decay than the exact solution. Since such high frequencies have no significant contribution to the response of the cable-connected systems of interest, we conclude that the DEC algorithm with the parameters described above produces accurate results for the purpose of the present study.

Two finite element models of the cable are considered in this study. The first model idealizes the cable with 100 truss elements having the same cross section as the cable. This model is intended to idealize the catenary cable under static conditions. The second model idealizes the cable with 100 frame elements having the same cross section properties as the cable. This model is intended to account for both the cable inertia and flexural rigidity. Full account of the geometric nonlinearity arising from large displacements and large rotations of the cable is made in the analyses by using a Lagrangian strain formula-

tion. The finite element program FEAP, developed by Taylor (1998), and the DEC algorithm, described above, are used for the analyses.

3.4 Comparison of the Finite Element Model with the Catenary Cable

Before proceeding with dynamic analysis, we investigate the responses of a cable under static loading and compare them with the theoretical results obtained for the catenary cable in our previous study. The cable consists of 271 strands in 10 layers, each strand having a diameter of 0.3038cm so that the total cross-sectional area of the cable is $A = 19.6\,\text{cm}^2$. The moment of inertia, computed using (3.6), is $I = 1.246\,\text{cm}^4$. The weight per unit length of the cable is $w = 52.2\,\text{N/m}$. The cable is assumed to have an initial length of 6m, when it is held over two supports 5m apart horizontally with zero vertical separation between the supports. To be consistent with our previous results for the catenary cable, $E = 7.0\times10^6\,\text{N/cm}^2$ is used for the present analysis. Using each finite element model, the horizontal force T in the left support is computed as the right support is moved quasi-statically in the horizontal direction. The normalized force $T/(wL)$, in which L denotes the current span length, is plotted as a function of the slackness $s/L-1$. Note that s denotes the actual length of the cable at each configuration, accounting for the extensibility of the cable.

Figure 3.3 shows a comparison of the horizontal force versus slackness curve for the catenary cable and the finite element model with truss elements. Recall that this model does not account for the flexural rigidity of the cable and, hence, it closely idealizes the catenary cable conditions. The results from the two analyses are virtually identical over a broad range of slackness values, thus demonstrating the accuracy of the finite element model.

It is important to note that a cable having flexural rigidity and held between two fixed supports is a statically indeterminate system. This is because the horizontal support force for such a system cannot be determined from equilibrium considerations alone. For the present analysis with the finite element model with frame elements, we have assumed that the cable is initially straight. After fixing both ends, the gravity load is applied and then the right support is moved horizontally towards the left support. Due to the flexural

rigidity, the shape of the cable is considerably different from the catenary shape. This can be seen in Figure 3.4, which shows the two shapes when the span is 5m. Figure 3.5 compares the normalized horizontal support force $T/(wL)$ as a function of the slackness $s/L-1$ for the catenary cable and the finite element model with frame elements. Due to the flexural rigidity, the support force is in compression for slackness values greater than 0.00275. It is seen that the horizontal force-slackness relationship for the cable with flexural rigidity is similar to that of the catenary cable but shifted downward in the vertical direction. It is of course possible to consider an initially curved cable. In that case, the horizontal force-slackness curve would tend to shift vertically upward so that the zero force point would occur at a slackness value at which no horizontal support force is necessary to hold the cable in its position. This indeterminacy of the initial shape of the cable with flexural rigidity is one more reason why it will not be possible to quantitatively match the experimental results of Dastous and Pierre, as described in the following section.

3.5 Comparison with Experimental Results of Dastous and Pierre

In this section, we compare finite element predictions of the cable response with the experimental results of Dastous and Pierre (1996). Two different cables used by Dastous and Pierre are considered for this analysis. These are code named 1796-MCM and 4000-MCM cable conductors. Their properties are listed in Table 3.1.

As mentioned earlier, our finite element model assumes constant cross-sectional area and moment of inertia along the cable. This is an approximation, since during the experiments the actual effective cross-sectional properties vary along the cable and in time, depending on whether the strands slide against each other or remain attached. It is practically impossible to predict the damping in the cable, which can be significant when the cable strands slide against one another under friction forces. An additional uncertainty has to do with the initial shape of the cable in the experiments. As mentioned earlier, the cable with flexural rigidity and fixed ends is a statically indeterminate system. Unfortunately the paper by Dastous and Pierre did not describe how the cables were shaped and put in their positions before starting the tests. In the analysis in this section, we have used

the following steps to set the initial shape of the cable: A straight cable of the specified length is modeled with both its ends fixed. The weight of the cable is applied as dead load and the cable is allowed to deform. One end of the cable is then moved toward the other end until the specified initial span length used in the experiment is achieved. The deformed shape of the cable in this position is computed. This shape is considered to be the initial shape of the cable without any internal forces. The cable with this shape is now placed on the supports with fixed ends and the reaction forces under the dead load are computed. Note that this will generate an initial horizontal tension force at each support. As described below, because of the uncertainty in the initial conditions of the cable in the experiments, this horizontal force as well as the cable sag will be somewhat different from the initial conditions reported in the experiments by Dastous and Pierre.

Because of the unavoidable differences between the finite element model and the experimental setup used by Dastous and Pierre, it is not possible to expect that the finite element predictions will closely match the experimental results. Hence, instead of a quantitative agreement, we seek to make a qualitative comparison between the theoretical predictions and the experimental results. In particular, we aim at verifying the large amplifications in the horizontal cable force under harmonic excitations, which were observed by Dastous and Pierre. We also carry out parameter variations in order to determine the importance of the flexural rigidity of the cable and the effect of energy dissipation due to friction forces in the cable.

3.5.1 Experiment 1: Sine-Start Test

In this experiment, a 1796-MCM conductor cable of length 5.52m and span length 5.19m was subjected to out-of-phase harmonic support motions having an amplitude of 0.02m and a frequency of 3.5Hz. Figure 3.6, taken from the paper by Dastous and Pierre (1996), shows the time history of the horizontal support force measured during the experiment. We note that the initial horizontal force is around 40N in tension. During the dynamic excitation, the horizontal cable force at each support fluctuates, taking on both positive (tension) and negative (compression) values. The maximum tension force achieved is approximately 400N, whereas the maximum compression force achieved is approxi-

mately 260N. It is important to note that under quasi-static conditions, the horizontal cable force would have varied only a small amount from its initial value of 40N. It is clear, therefore, that the cable inertia and flexural rigidity significantly amplify the cable force.

In the finite element analysis, we apply out-of-phase, harmonic horizontal support displacements of the form

$$u(t) = [1 - \exp(-2\pi\alpha f t)]A\sin(2\pi f t) \tag{3.7}$$

where $A = 0.02\,\text{m}$ is the amplitude and $f = 3.5\,\text{Hz}$ is the frequency. The term inside the square brackets is a loading ramp that is included to avoid numerical instability caused by non-zero initial conditions. For the present analysis, $\alpha = 0.1$ is used. Note that the term inside the square brackets approaches unity in a few cycles and the motion becomes purely harmonic. The Young's modulus of the cable is assumed to be the IEEE-recommended value of $E = 5.72\times10^6\,\text{N/cm}^2$ and the moment of inertia is computed from (3.6). No damping in the cable is assumed for this analysis.

Figure 3.7 shows a plot of the time history of the horizontal cable force as predicted by the finite element model. The overall features of the response are similar to those observed for the experimental result shown in Figure 3.6. In particular, the response shows large amplification of the horizontal cable force due to the inertia and flexural rigidity effects. We also note that the cable experiences significant compression forces. Whereas the initial cable force is 83N, the maximum tension force achieved is 265N and the maximum compression force achieved is 97N. These values are significantly different from the values observed in the experiment. As mentioned earlier, the reasons for this discrepancy may include the assumed values of the cable moment of inertia and damping, as well as the assumed initial shape of the cable. More detailed information about the conditions of the experiment as well as a more refined model of the cable that accounts for the variability of stiffness and damping properties along the length and in time are necessary if a close agreement between the theoretical and experimental results is to be achieved. Nevertheless, the above comparison shows that the large amplification of the cable force, including compression forces, observed by Dastous and Pierre for cables

subjected to harmonic support motions is realistic and is predicted by the finite element model.

The differences observed between the experimental and theoretical results suggests that the cable response might be sensitive to the assumed values of the moment of inertia and damping. To explore the sensitivity with respect to the moment of inertia, we repeat the above analysis while varying the moment of inertia in the range $I = I_{min}$ to $I = 12I_{min}$, where I_{min} is as given in (3.4). It is assumed that the cable has zero damping. The maximum horizontal tension and compression forces, after 3 seconds of motion, are plotted in Figure 3.8 as a function of the ratio I / I_{min}. The maximum responses are found to have mild dependence on the moment of inertia, except in the region of $I < 3I_{min}$. For this value of the moment of inertia, the maximum forces in both tension and compression side are sharply amplified. Evidently, for this value of the moment of inertia the cable is in some sort of resonance with the harmonic excitation. A similar but much smaller resonance effect is noticeable around the value $I = 9I_{min}$. Unfortunately we have no means of knowing what value of I best reflects the conditions of the cable tested by Dastous and Pierre.

In the above analysis, the cable was assumed to have no damping. However, as mentioned earlier, there can be significant dissipation of energy due to sliding of the cable strands against one another under the action of friction forces. Such damping would of course depend on the cable force and curvature at each location and, hence, would vary along the cable and in time. Noiseux (1992) has proposed a hysteretic damping model for cables, which is reported to agree well with experimental results. Unfortunately, implementation of this class of models in FEAP was not possible within the time scope of this project. Instead, we attempted to investigate the sensitivity to damping by using a uniformly distributed viscous damping model, which is already available in FEAP. In this model, the distributed viscous damping is achieved by placing a dashpot at each node of the finite element model, as shown in Figure 3.9. While this model may not be realistic in describing energy dissipation by internal friction forces, it provides a preliminary estimate of the importance of the damping effect on the dynamic response of cables.

For the numerical study, $I = 6I_{min}$ is assumed and the damping coefficient is varied over the range of zero to 100Ns/m^2 per unit length of the cable. To provide a scale for this damping value, it is noted that when the damping value of 100Ns/m^2 is used, the maximum damping force achieved in the cable under the harmonic motion with frequency 3.5Hz is approximately 111N/m. This can be compared with the maximum inertia force, which is approximately 58N/m, and the weight per unit length of the cable, which is 24.6N/m. Thus, while 100Ns/m^2 might be an unrealistically high value for the distributed damping, values around 10-50Ns/m^2 might be quite realistic. Figure 3.10 shows a plot of the maximum horizontal tension and compression forces, after 3 seconds of motion, as a function of the distributed damping coefficient. It is seen that the maximum horizontal forces in the cable increase with increasing damping. This is because the excitation is an imposed support displacement and, naturally, larger forces are necessary to counter the damping effect. Unfortunately we have no means of knowing what value of the damping coefficient best represents the conditions present during the tests by Dastous and Pierre. Nevertheless, this study shows that some of the discrepancy between our theoretical predictions and the experimental results could be attributed to the effect of damping in the cable. We believe further study on the effect of damping in conductor cables is highly desirable.

3.5.2 Experiment 2: Sine-Sweep Test

In this experiment by Dastous and Pierre (1996), a 4000-MCM conductor cable was subjected to out-of-phase harmonic support motions of amplitude 0.02m and frequencies in the range 0.5-5Hz. The cable has a length of 5.64m and an initial span length of 5.35m. Figure 3.11, taken from the paper by Dastous and Pierre, shows plots of the peak horizontal tension and compression forces at the support as functions of the excitation frequency. It is seen that the maximum tension and compression forces vary by several orders of magnitude, depending on the excitation frequency. A peak appears to occur in the maximum tension force at around 4.3Hz, which could be due to some sort of resonance.

For the finite element analysis, the cable is assumed to have constant cross-sectional area and moment of inertia as given by (3.3) and (3.6), respectively. Zero damping is as-

sumed. The support motions are taken to be out of phase and described by (3.7) with the frequency f varying from 0.5 to 5Hz. The resulting maximum tension and compression forces, after 3 seconds of response at each frequency, are plotted in Figure 3.12 as functions of the excitation frequency. The overall features of these plots are similar to the experimental results shown in Figure 3.11. The maximum tension and compression forces show variations by several orders of magnitude, depending on the excitation frequency. Peaks on both tension and compression sides appear at around 2.7Hz frequency, possibly indicating some sort of resonance effect. A similar effect may be present at around 4.6Hz frequency, where the peak responses appear to grow unboundedly. The differences between the experimental and analytical results can be attributed to our assumed values of the cross-sectional area, moment of inertia and damping, and the assumed initial shape of the cable. Unfortunately we have no means of knowing which values of these parameters better represent the experimental conditions. In spite of the quantitative discrepancy between the experimental and analytical results, this study shows that indeed extremely large forces can develop in the cable when it is subjected to harmonic support motions.

3.6 Cable-Connected Equipment Items

In this section we study the effect of flexural rigidity and inertia of the cable conductor on the interaction between two connected equipment items. Figure 3.13 shows a schematic description of the connected system. For the conductor, we consider the aluminum cable investigated in our previous study, which consists of 271 strands in 10 layers, each strand having a diameter of 0.3038cm. The cross-sectional area is $A = 19.6\,\text{cm}^2$, the moment of inertia computed from (3.6) is $I = 1.246\,\text{cm}^4$, the Young's modulus is $E = 7.0\times10^6\,\text{N/cm}^2$, and the weight per unit length of the cable is $w = 52.2$ N/m. First, we consider the case when the cable has an initial length $s_0 = 5.0332\,\text{m}$ and an initial span of $L_0 = 5\,\text{m}$. For the catenary cable, this corresponds to a sag to span ratio of 0.05. This is a rather taut cable and represents perhaps an extreme case. We select it to highlight the effect of interaction and the highly nonlinear nature of the response. Subsequently, we vary the length of the cable in order to investigate the interaction effect for varying cable slackness values. The cable is assumed to connect two equipment items having masses

$m_1 = 1000\,\text{kg}$ and $m_2 = 500\,\text{kg}$, an attachment configuration such that $l_1/m_1 = l_2/m_2 = 1$, stand-alone frequencies $\omega_1 = 2\pi$ rad/s and $\omega_2 = 10\pi$ rad/s, and damping ratios $\zeta_1 = \zeta_2 = 0.02$.

3.6.1 Effect of Flexural Rigidity, Inertia and Damping of the Cable on the Equipment Response

We examine the responses of the above system to the N-S component of the Newhall record of the 1994 Northridge earthquake. The accelerogram of this ground motion is shown in Figure 3.14. Figure 3.15 shows the stand-alone responses of the two equipment items calculated by finite element analysis using the DEC algorithm. The calculated maximum stand-alone displacements are $\max|u_{10}(t)| = 0.3358$m and $\max|u_{20}(t)| = 0.0159$m, respectively, and the maximum relative separation between the two stand-alone equipment items is $\Delta = \max[u_{20}(t) - u_{10}(t)] = 0.3163\,\text{m}$. These estimates are slightly different from the values computed in our previous study (0.3375m, 0.0162m and 0.3163m, respectively), which were based on the Newmark algorithm.

Figure 3.16 shows displacement responses of the two equipment items when both the flexural rigidity and inertia of the cable are neglected. These results are from our previous study and were computed using the Newmark algorithm together with an analytical expression of the catenary cable stiffness. Note that the scales used in Figure 3.16 (and the subsequent five figures) are different from the scales used in Figure 3.15. The maximum responses in Figure 3.16 are $\max|u_1(t)| = 0.500$m and $\max|u_2(t)| = 0.124\,\text{m}$, respectively, which are much larger than the peak stand-alone responses given in the preceding paragraph. It is also noticeable that the response is asymmetric with larger peaks in the equipment responses occurring in the direction of the cable. Unfortunately, using time steps of reasonable size, it was not possible to generate similar results with the finite element model because the numerical integration did not converge when the flexural rigidity and inertia of each frame element were set to zero or small values.

To see the effect of the cable inertia alone, we use the finite element model with the frame elements but set the section moment of inertia of each element to a negligibly small value. The displacement responses for the two equipment items in this system are shown in Figure 3.17. The peak absolute responses now are $\max|u_1(t)| = 0.444\text{m}$ and $\max|u_2(t)| = 0.105\text{m}$, respectively. These values are smaller than the peak values for the case without the inertia effect in Figure 3.16. However, the response curves show stronger asymmetry. Evidently, for this cable, the inertia effect tends to reduce the peaks in the equipment responses, but accentuates the asymmetry of the response. Slightly longer periods in the equipment responses in Figure 3.17 are detectable, when compared with the responses in Figure 3.16 for the cable without mass. These are due to the added mass of the cable.

To see the effect of the cable flexural rigidity alone, we use the finite element model with the frame elements but set the mass of each element to zero, while representing the weight as a dead load. The displacement responses for the two equipment items in this case are shown in Figure 3.18. The peak absolute responses now are $\max|u_1(t)| = 0.422\text{m}$ and $\max|u_2(t)| = 0.130\text{m}$, respectively. In comparison to the case without cable inertia and flexural rigidity shown in Figure 3.16, the peak absolute response of the lower-frequency equipment item is smaller, while that of the higher-frequency equipment item is larger. This agrees with the finding in our previous study that a larger stiffness of the connecting element tends to increase the response of the higher-frequency equipment item and decrease that of the lower-frequency equipment item. Furthermore, with the cable flexural rigidity included, the response of the system is less asymmetric. This is due to increased "beam effect" in the cable. Finally, in the tail region, the response time histories show shorter periods than in Figure 3.16 because of the added flexural stiffness of the cable. In the region of strong response, the cable stiffness is dominated by its axial stiffness, which is the same for both cases, and as a result the predominant period of the response does not change.

Now we consider the system with both the flexural rigidity and inertia of the cable included. Figure 3.19 shows the displacement responses of the two equipment items for

this case. The peak absolute responses now are $\max|u_1(t)| = 0.393\text{m}$ and $\max|u_2(t)| = 0.121\text{m}$, respectively. These peak values are slightly smaller than the values for the previous case, which included only the flexural rigidity of the cable. Evidently, for this cable, cable inertia tends to reduce the peak responses with or without the effect of flexural rigidity. This result, however, may not apply to other cable/equipment configurations or ground motions. As we will see, it is possible that resonance-type effects arise in the cable response leading to larger responses of the equipment items.

In the above analysis, the cable was assumed to have zero damping. As discussed earlier, slippage of the cable strands under friction forces could dissipate significant amounts of energy. To explore this effect, finite element analysis with the frame element was carried out, while including the flexural rigidity and inertia of the cable as well as a uniformly distributed viscous damping with a coefficient of 10Ns/m^2. Figure 3.20 shows the displacement responses of the two equipment items for this case. The peak absolute responses now are $\max|u_1(t)| = 0.355\text{m}$ and $\max|u_2(t)| = 0.112\text{m}$, respectively. As expected, these peak values are smaller than those without cable damping shown in Figure 3.19.

3.6.2 Effect of Interaction in the Cable-Connected System

To determine the effect of interaction on equipment items in a cable-connected system, we compute and plot the response ratios R_1 and R_2 for the system described in the previous section for five different ground motions, which were described in our previous study (Der Kiureghian et al. 1999). All system parameters are kept constant, with the exception of the initial cable length s_0, which is varied to cover a range of the interaction parameter β defined in (3.1). Since the vertical separation between the support points is zero, we have $c_0 = L_0$ and the interaction parameter simplifies to

$$\beta = \frac{\Delta}{s_0 - L_0} \tag{3.8}$$

where $L_0 = 5\,\text{m}$ is the initial span and $\Delta = \max[u_{20}(t) - u_{10}(t)]$ is the maximum relative separation between the two stand-alone equipment items for the selected ground motion.

Figure 3.21 shows plots of the response ratios R_1 and R_2 as functions of the interaction parameter β for the five selected ground motions, where the effects of flexural rigidity and inertia of the cable are neglected. These results are copied from our previous study. As we had discussed, there is virtually no amplification of the equipment responses for values of β less than 1. Based on this finding, in our previous report we recommended a cable length based on $\beta = 1$.

Figure 3.22 shows plots of the response ratios R_1 and R_2 as functions of the interaction parameter β for the five selected ground motions, where we have included the effects of flexural rigidity and inertia of the cable. For $\beta > 1$, significant amplification of the equipment responses occurs similar to that in Figure 3.21. The response ratios for a specific ground motion and β value in the two figures are not identical, but the overall features are the same. For $\beta < 1$, Figure 3.22 shows small amplifications of the equipment responses, which are absent in Figure 3.21. In particular, for the TabasLN record, a local peak of 1.36 appears in the response ratio R_1 around $\beta = 0.9$, which may be due to some sort of resonance for this particular cable configuration and input ground motion. This is similar to the resonance-like behavior observed in the experiments by Dastous and Pierre (1996) and our own analytical results in Section 3.5.

Based on the results shown in Figure 3.22, it appears that the recommendation of selecting a cable length for which $\beta \leq 1$ is still valid. This corresponds to a length of $s_0 > L_0 + \Delta$ for a cable with no vertical offset between its supports. However, in light of possible resonance-type amplification of the cable, it is advisable to design the equipment items for forces slightly (about 50%) higher than the forces obtained for the stand-alone configuration. It should be emphasized that this recommendation is based on a rather limited study. Further investigations are advisable to ascertain the range of applicability of this rule for different types of ground motions and cable/equipment configurations.

Table 3.1. Properties of conductor cables used in the experiments by Dastous and Pierre

Property	1796-MCM	4000-MCM
material	all aluminum	all aluminum
Young's modulus	5.72×10^6 N/cm^2	5.72×10^6 N/cm^2
number of layers	5	10
number of strands	61	271
strand diameter	0.436 cm	0.309 cm
overall conductor diameter	3.92 cm	5.86 cm
cross section area	910 mm^2	2027 mm^2
mass per unit length	2.509 kg/m	5.698 kg/m

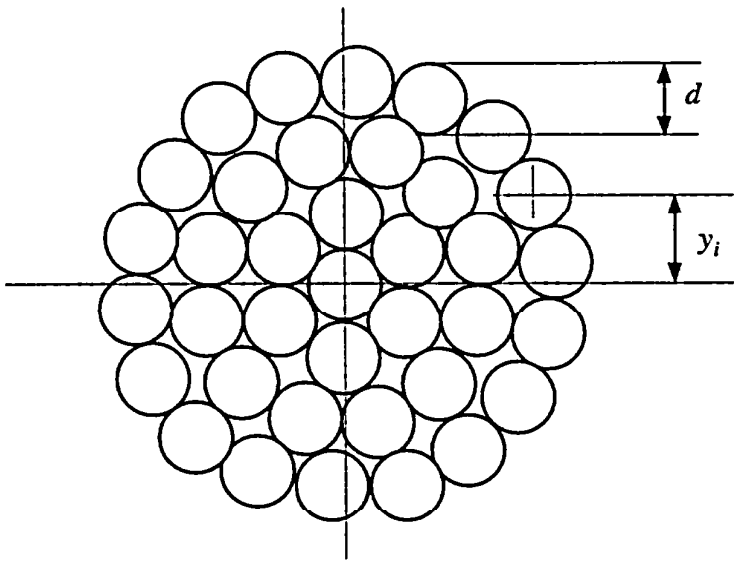

Figure 3.1 Cross section of a conductor cable made of braided wire strands

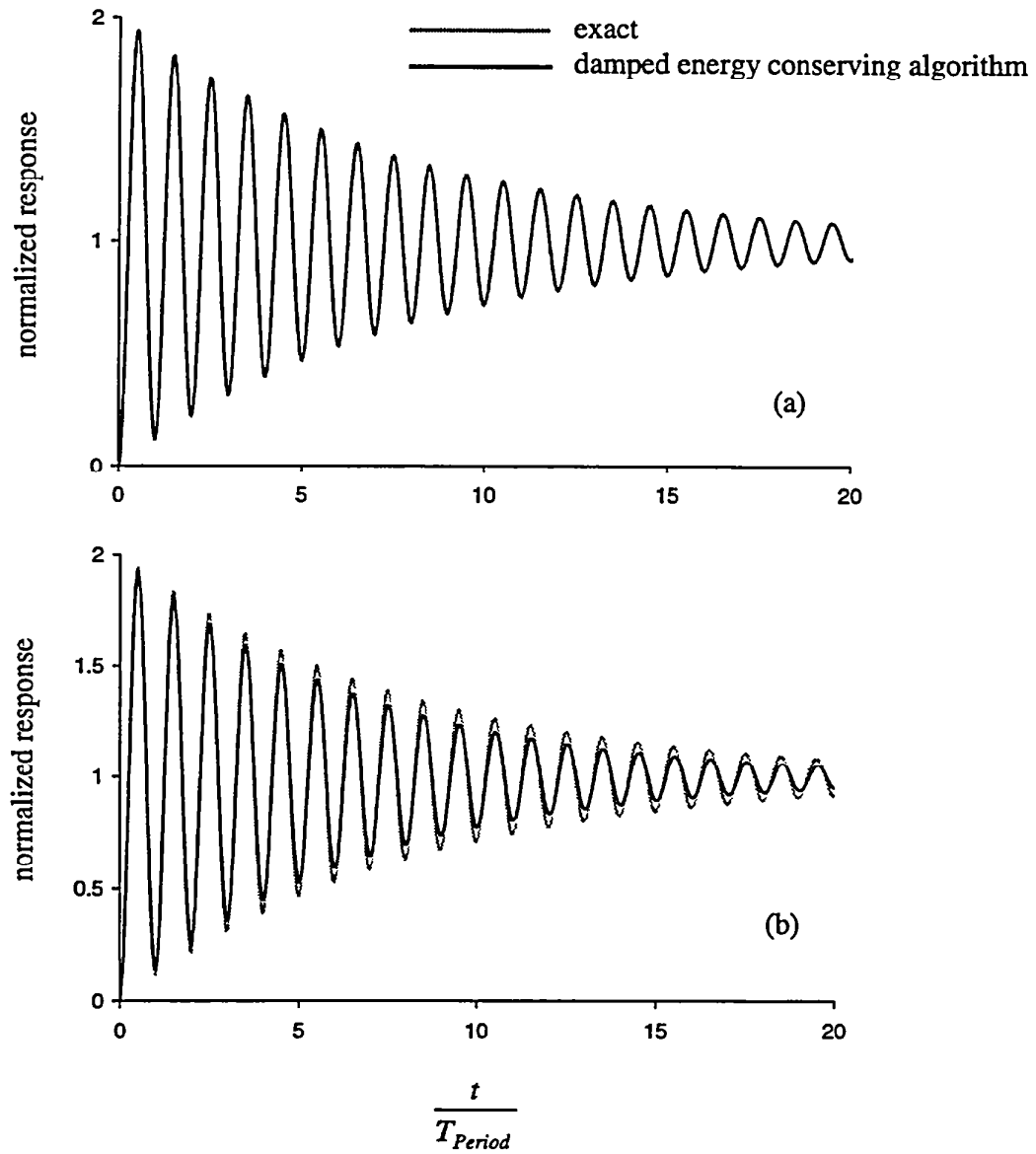

Figure 3.2 Comparison of exact and computed normalized responses of an oscillator to step loading: (a) oscillator with 5Hz frequency and 2% damping ratio, (b) oscillator with 50Hz frequency and 2% damping ratio

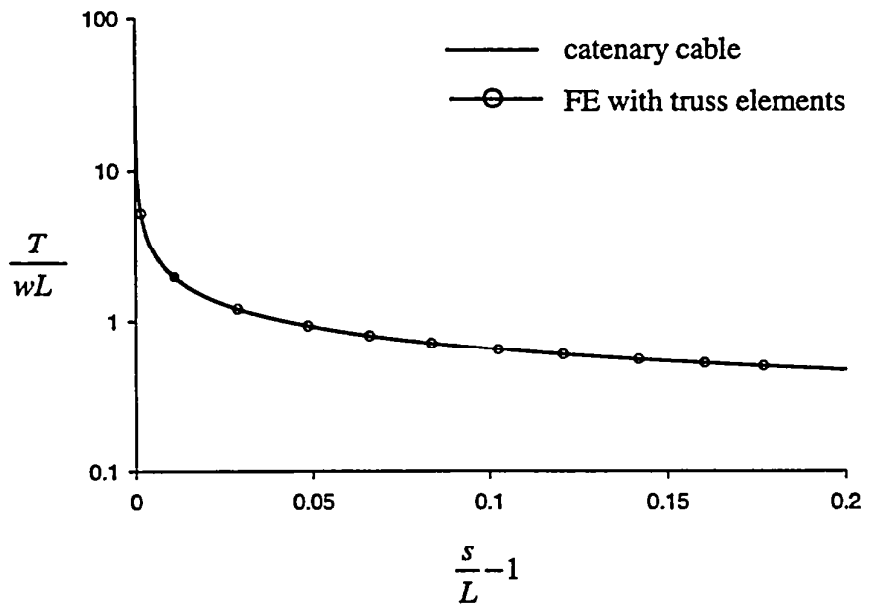

Figure 3.3 Horizontal force versus slackness for a cable with no flexural rigidity under its own weight

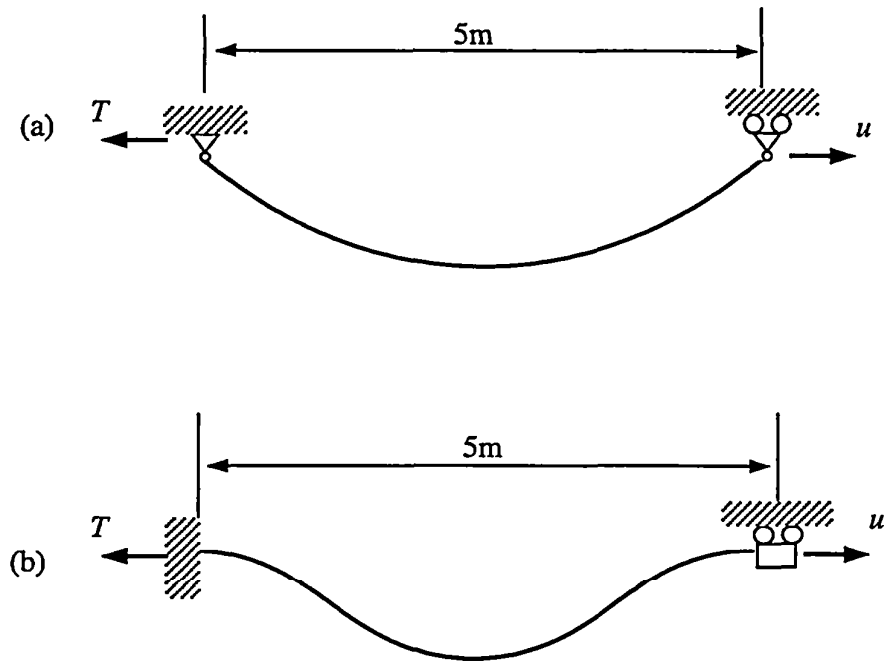

Figure 3.4 Shapes of cables of length $s_0 = 6\,\mathrm{m}$: (a) without flexural rigidity, (b) with flexural rigidity

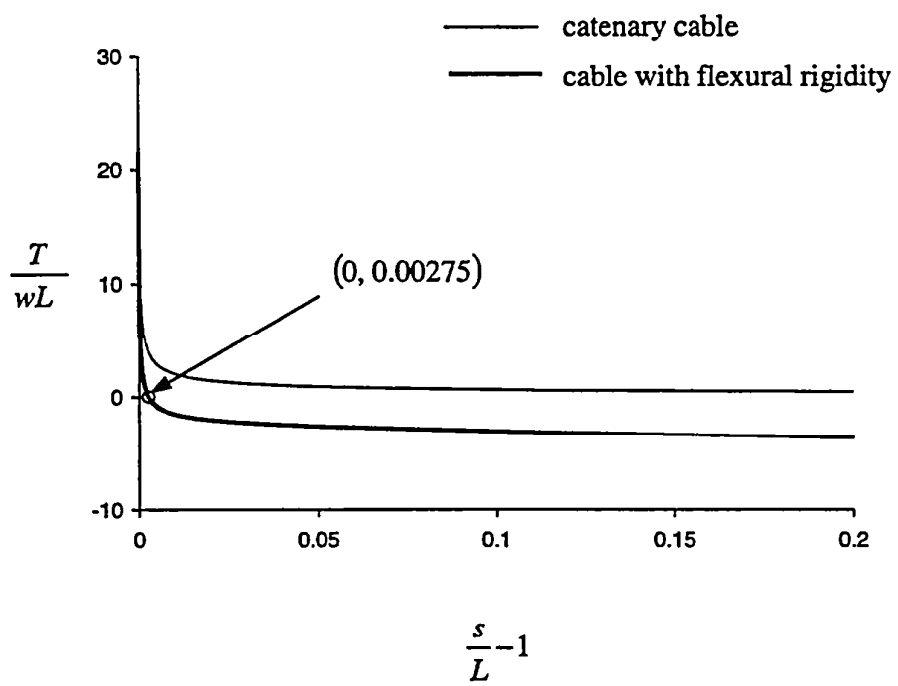

Figure 3.5 Comparison of horizontal force-slackness relationship for a catenary cable and a cable with flexural rigidity

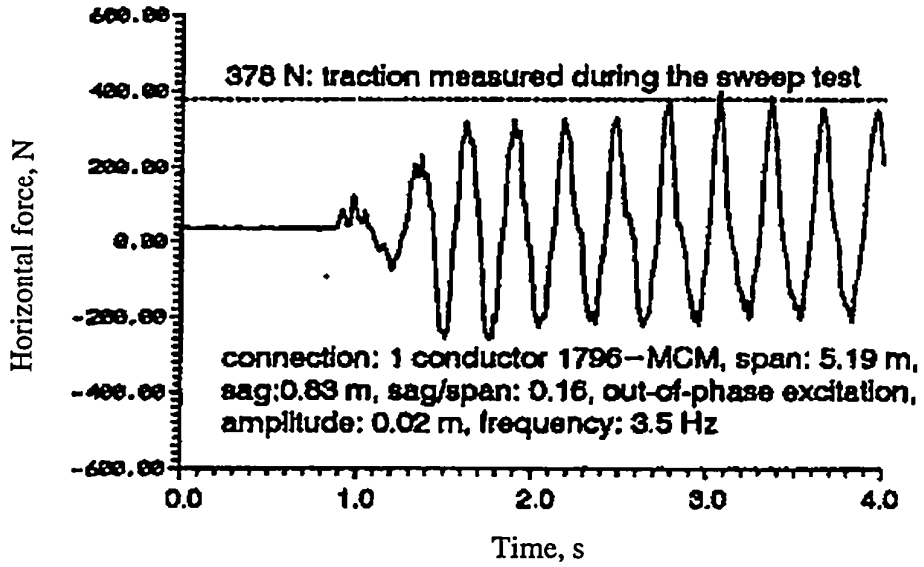

Figure 3.6 Time history of horizontal force at the cable support (after Dastous and Pierre, 1996)

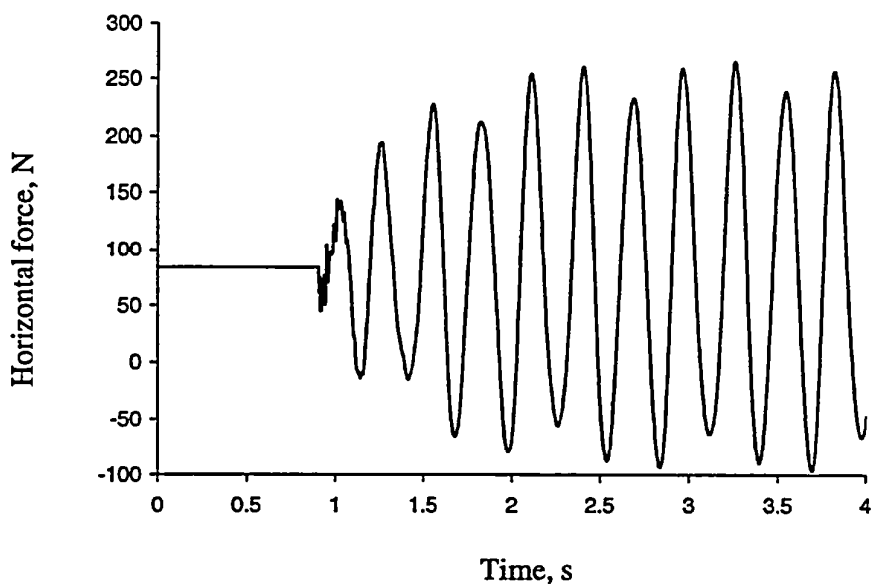

Figure 3.7 Time history of horizontal force at the cable support as predicted by the finite element model

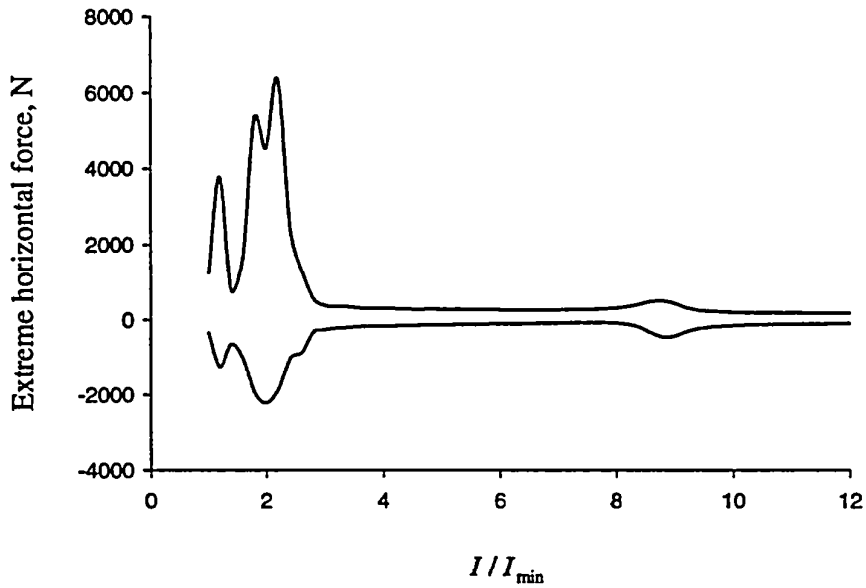

Figure 3.8 Sensitivity of the horizontal force at the support to cable moment of inertia

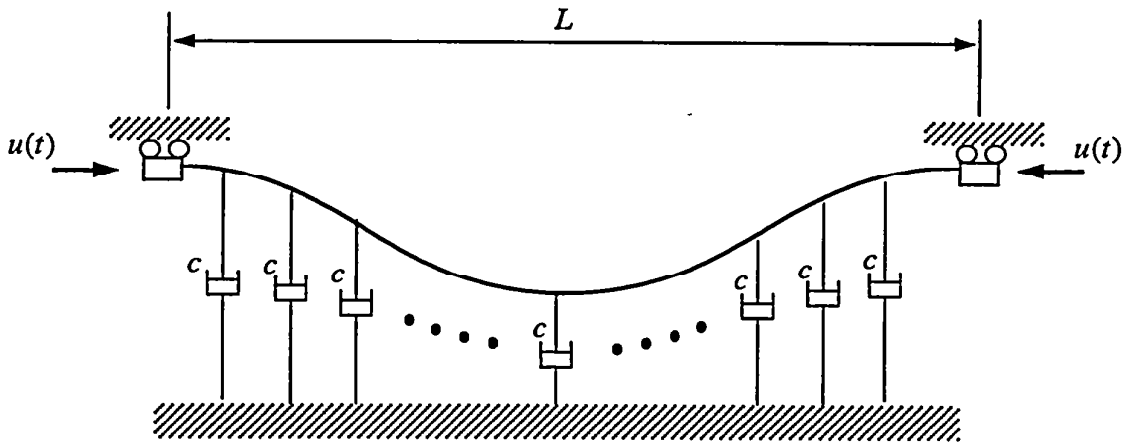

Figure 3.9 Finite element model of distributed viscous damping

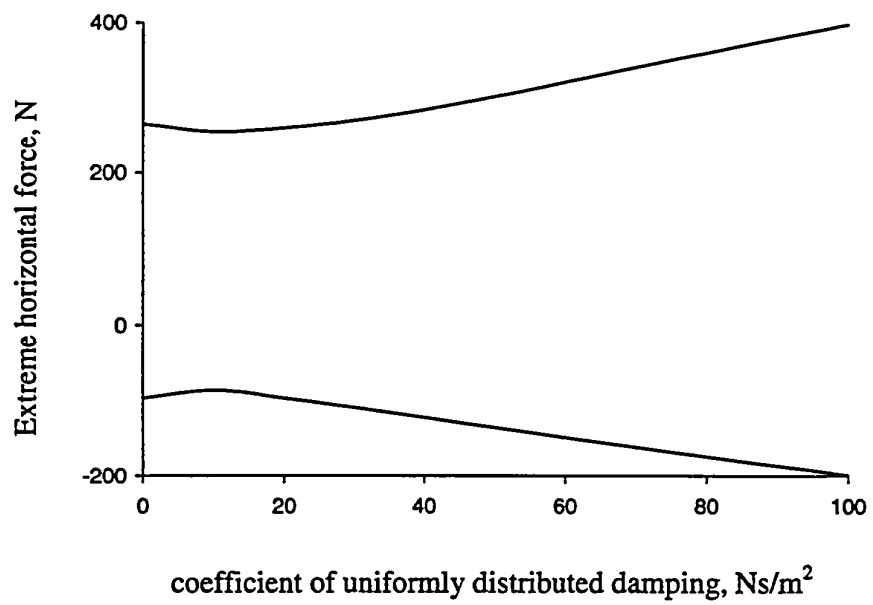

Figure 3.10 Sensitivity of the horizontal force at the support to cable damping

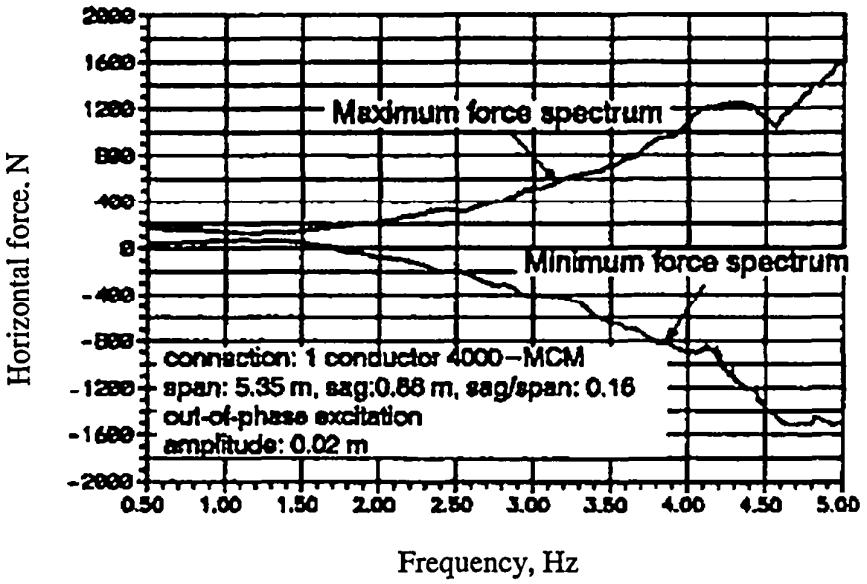

Figure 3.11 Horizontal support force spectrum obtained from the experiment (after Dastous and Pierre, 1996)

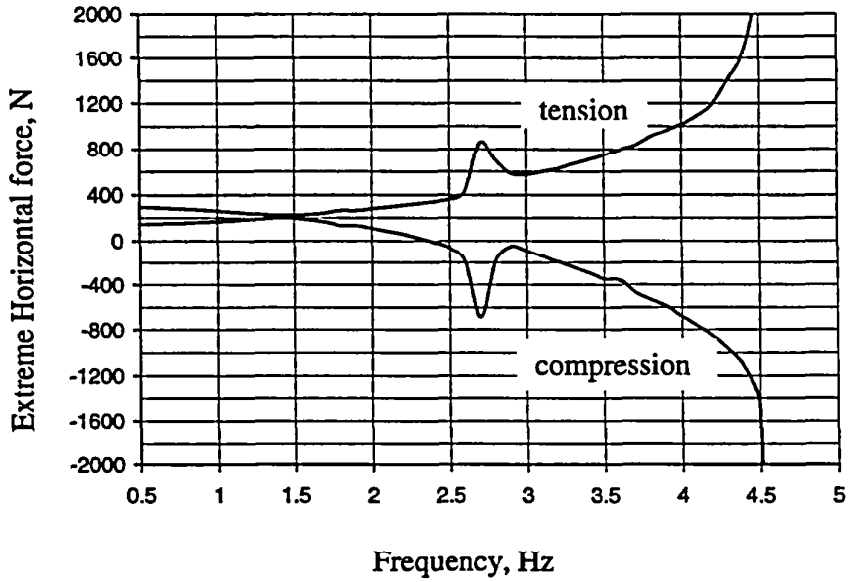

Figure 3.12 Horizontal support force spectrum predicted by the finite element model

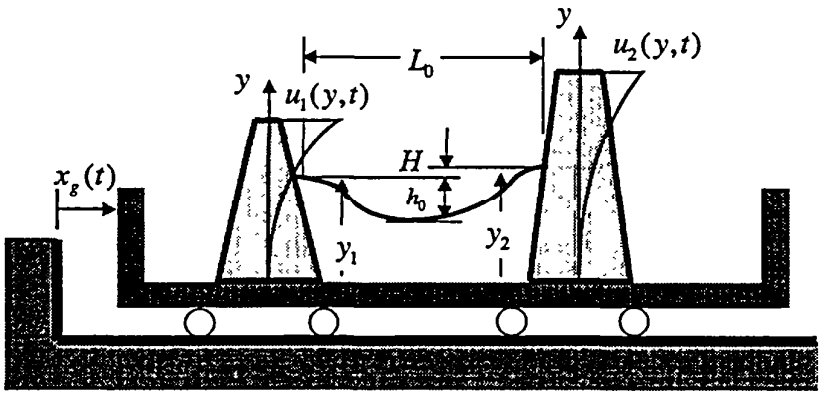

Figure 3.13 Cable-connected equipment items

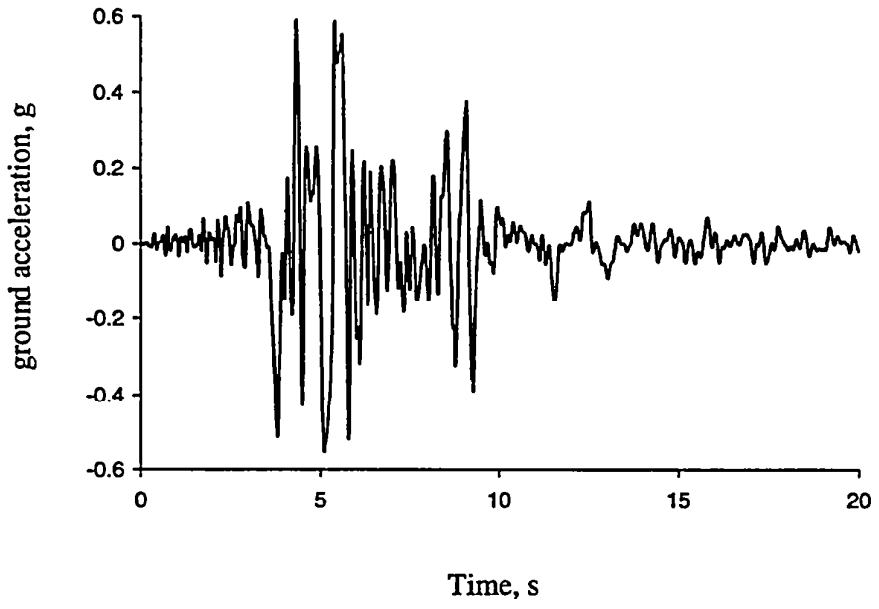

Figure 3.14 N-S component of Newhall record, 1994 Northridge Earthquake

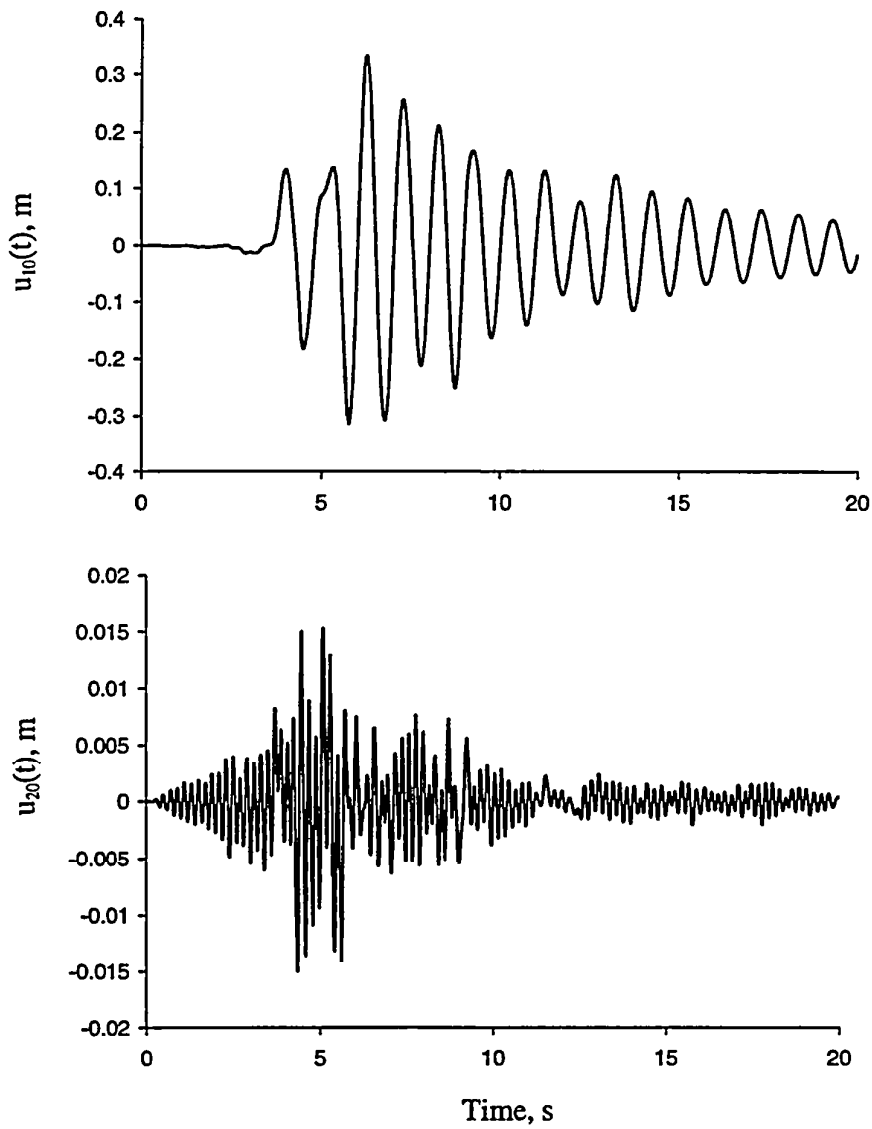

Figure 3.15 Displacement time histories of the stand-alone equipment items calculated by the damped energy-conserving algorithm

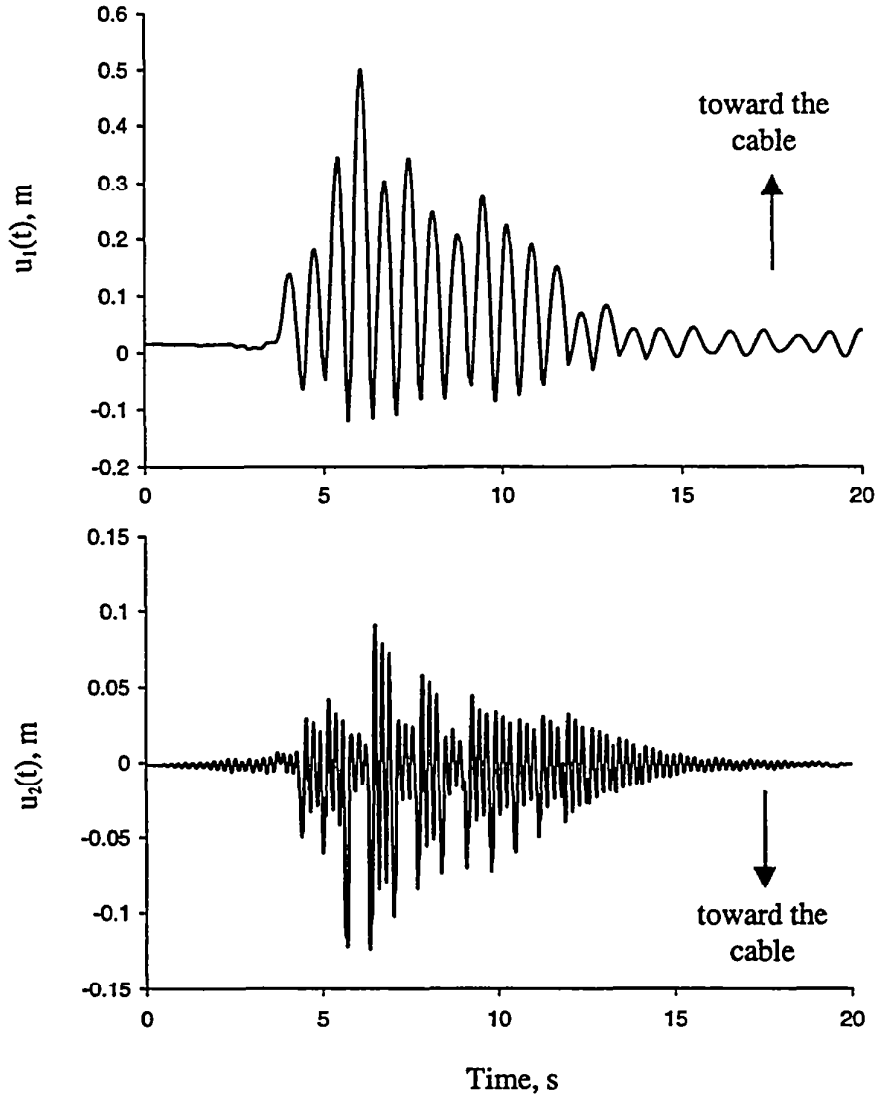

Figure 3.16 Displacement time histories of equipment items in the connected system, using catenary cable formulation and neglecting flexural rigidity, inertia and damping of the cable

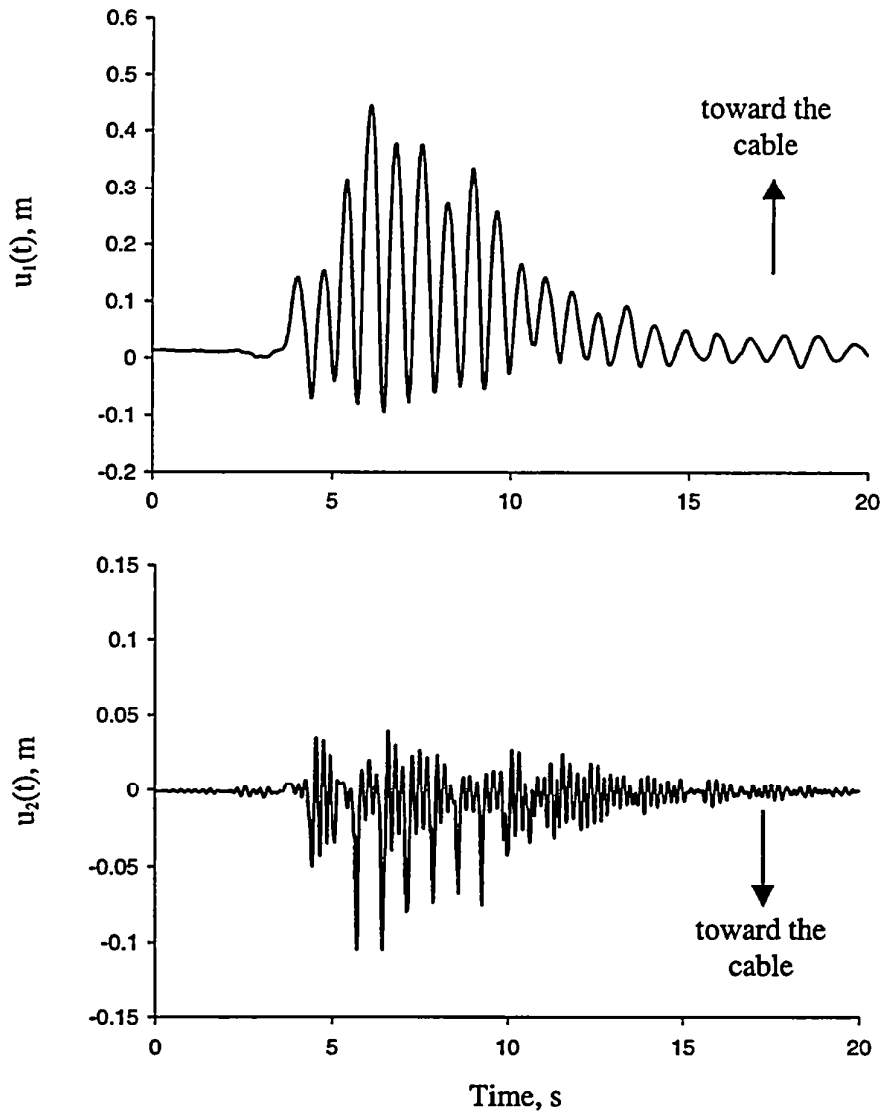

Figure 3.17 Displacement time histories of equipment items in the connected system, including the inertia effect but neglecting the flexural rigidity and damping of the cable

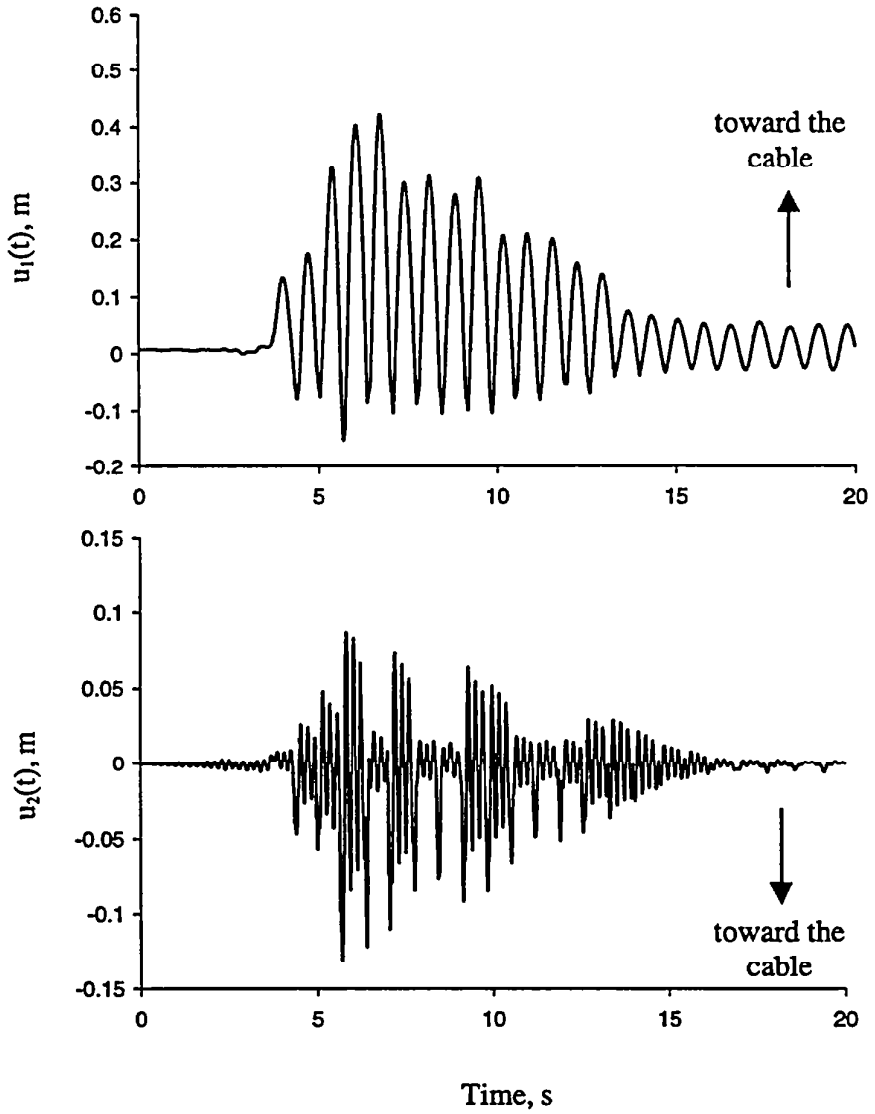

Figure 3.18 Displacement time histories of equipment items in the connected system, including the flexural rigidity but neglecting the inertia and damping of the cable

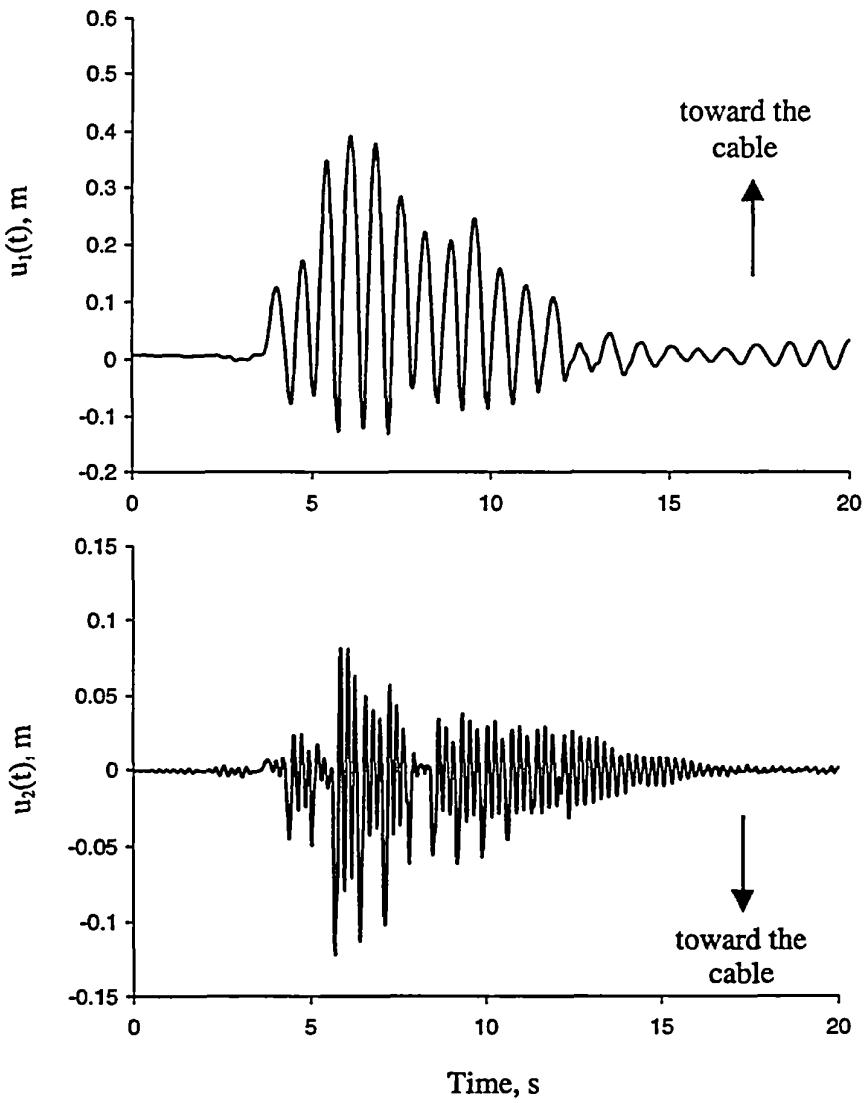

Figure 3.19 Displacement time histories of equipment items in the connected system, including flexural rigidity and inertia, but neglecting the damping of the cable

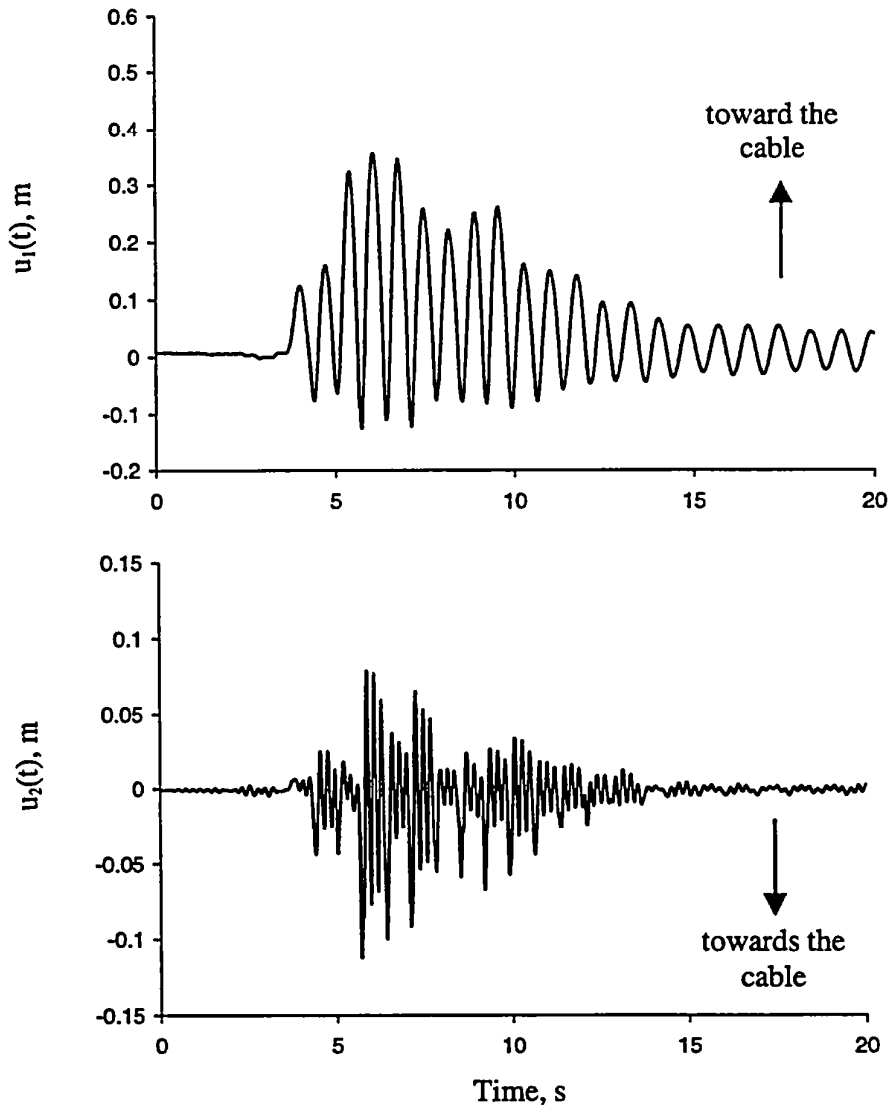

Figure 3.20 Displacement time histories of equipment items in the connected system, including the flexural rigidity, inertia and damping of the cable

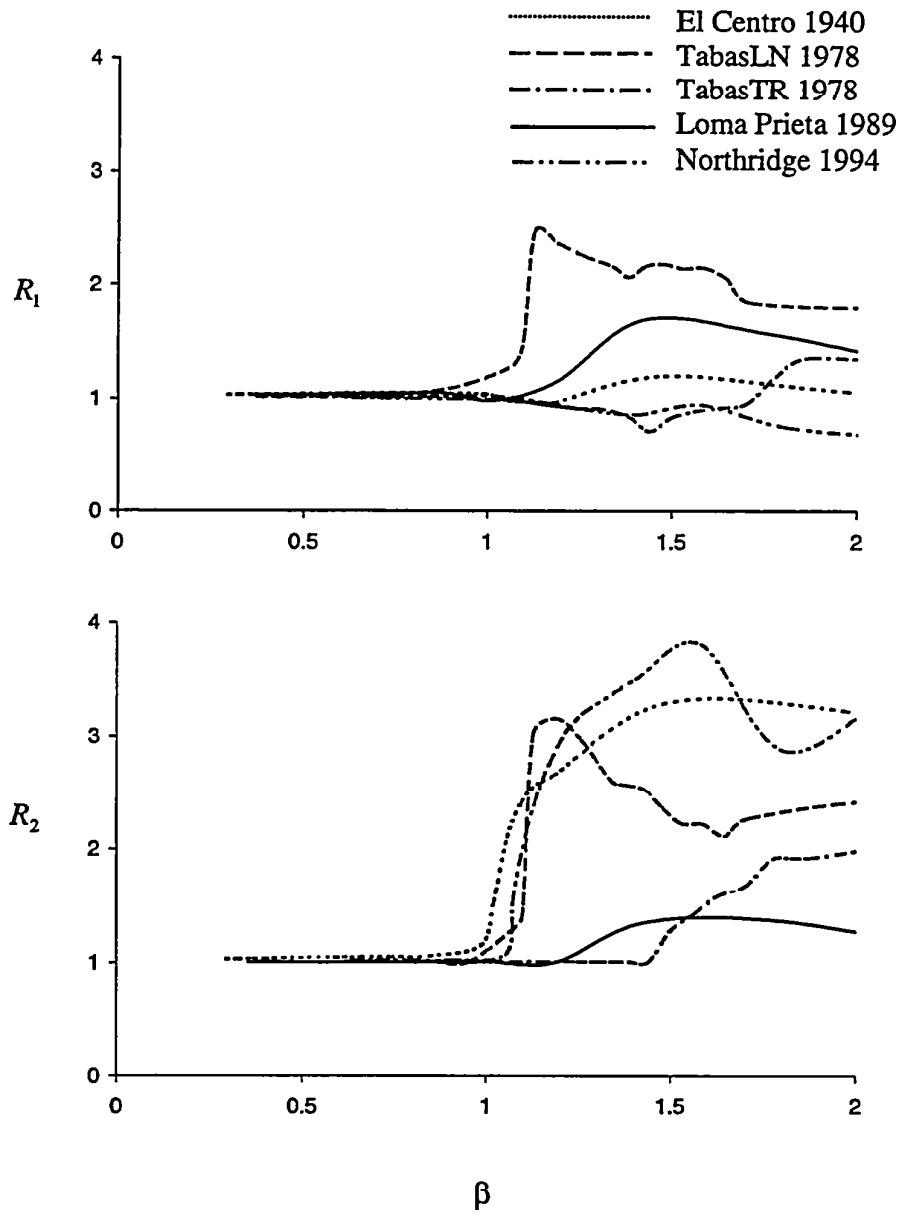

Figure 3.21 Response ratios for five earthquakes as functions of the interaction parameter neglecting the flexural rigidity, inertia and damping of the cable

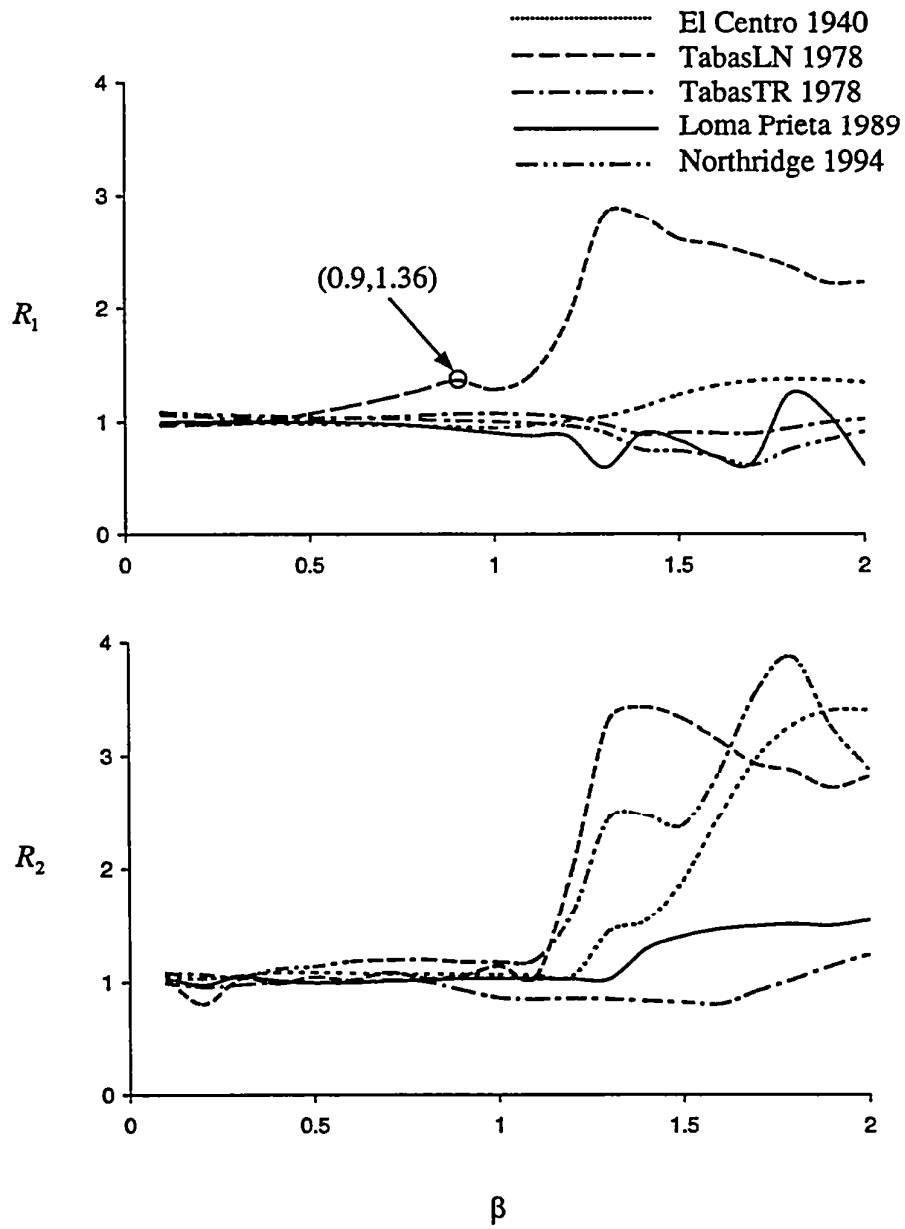

Figure 3.22 Response ratios for five earthquakes as functions of the interaction parameter, including the flexural rigidity and inertia of the cable with zero damping

Chapter 4 Summary and Recommendations for Further Study

4.1 Summary

The main results of the study can be summarized as follows:

(a) An elasto-plastic, large deformation finite element model of the flexible strap connector (FSC) was developed and used to predict the cyclic behavior of the a rigid bus (RB) -FSC system under imposed quasi-static cyclic displacement. The predictions are in reasonably close agreement with the results of tests conducted at the University of California at San Diego (UCSD). More accuracy in the characterization of the material can be achieved if cyclic test results of the material coupon are available. Under large deformations, the bars and straps of the FSC develop contacts and slippage under friction forces. These effects are not included in the current finite element model. A refined model including these effects is expected to provide more accurate predictions. Such a refined model can be used in the future to predict the behavior of other FSC configurations to large cyclic deformations, thus avoiding costly experiments.

(b) An analytical model of the hysteretic behavior of the RB-FSC is developed by use of a modified version of the well known Bouc-Wen differential representation. This model is subsequently used for dynamic analysis of two equipment items connected by an RB-FSC conductor. Time history analysis for two recorded earthquake ground motions are carried out to determine the effects of interaction on each equipment item. Separate analyses are performed to investigate the influences of the flexibility and energy dissipation characteristics of the FSC on the interaction effect. The results show that the flexibility and energy dissipation characteristics of the FSC sig-

nificantly reduce the adverse interaction effect, particularly on the higher-frequency equipment item. Reasonably good agreement with experimental results is achieved.

(c) For the flexible cable conductor, which is made of braided aluminum wire strands, a finite element model using elastic frame elements and a Lagrangian formulation is developed that accounts for large displacements and rotations. Comparisons with existing experimental results for conductor cables subjected to imposed harmonic support displacements are made. Qualitative agreement between the analytical and experimental results is obtained, but large differences in the force magnitudes occur. These differences are attributed to prevailing uncertainties associated with determining the rigidity and damping characteristics of the cable and its initial shape. Nevertheless, the analytical predictions verify the important experimental finding that cable forces can be magnified by several orders of magnitude when the cable is subjected to imposed harmonic end displacement of certain amplitude and frequency.

(d) The finite element model of the cable is used to investigate the effect of interaction in a combined system consisting of two equipment items connected by a conductor cable. Detailed time history results are presented for the Newhall record of the Northridge earthquake, where separate analyses are performed to demonstrate the influences of the cable flexural rigidity, inertia and damping on the interaction effect. These influences are found to be rather mild, certainly not nearly as large as had been anticipated by previous investigators based on the experiments mentioned above.

(e) Extensive time history analyses are carried out for five different recorded ground motions and for varying cable slackness to determine the effect of interaction on each connected equipment item as a function of an interaction parameter. Based on this study, a recommendation for the minimum cable length to avoid the adverse effect of interaction is formulated. This formulation now accounts for the effects of cable flexural rigidity and inertia, but not damping. Since no accurate information regarding the cable damping is currently available, for the sake of conservatism the above recommendation was formulated assuming zero damping in the cable.

4.2 Recommendations for Further Study

In light of the results obtained in the present study, we recommend consideration of the following topics for further study:

(a) Develop a more refined finite element model of the flexible strap connector that accounts for the contact and friction between the bars and straps. Similar models can be developed for the slider connector, as well as for other connectors of different geometry. With such refinement, accurate prediction of the behavior of flexible connectors under large cyclic deformations can be made by finite element analysis, accounting for both material and geometric nonlinearities and for the contact and friction effects, thus avoiding costly experiments that so far have been necessary. This approach can also be used to explore new designs of the connecting element that are aimed at improving its seismic performance or electrical function.

(b) Conduct experiments and develop analytical models to better characterize the flexural rigidity and energy dissipation of conductor cables that are made of braided wire strands. Finite element models should be developed that account for the slippage of the strands against each other under friction forces. These effects should be related to the deformation and force in the cable, so that variation of properties along the cable can be determined. With such refined models, it should be possible to accurately predict the dynamic behavior of conductor cables under imposed end displacements, for which experimental results are available. It is believed that results from such analysis will be of interest in determining the response of transmission cables subjected to earthquake and wind loading.

(c) The recommendation for the minimum cable length to avoid the adverse effect of interaction formulated in this study is preliminary in nature. This is because we are uncertain about the effective values of cable rigidity and damping. For the sake of conservatism, we have used zero cable damping to develop the present recommendation. Furthermore, the investigation so far has considered only five recorded ground motions. Since the response is highly nonlinear and strongly sensitive to the details of the ground motion, a broader set of records should be investigated before a final rec-

ommendation can be made. Study item (b) listed above will also allow us to re-examine this recommendation with a more refined characterization of the cable properties.

(d) Throughout this study we have used a deterministic method of analysis with specifically selected ground motions. Ideally, a random vibration approach should be used to properly account for the variability present in the ground motion. Such a study can be conducted with relative ease by use of the analytical hysteresis model developed for the RB-FSC in this study. For the cable-connected system, the nonlinear random vibration problem can be considerably more difficult.

REFERENCES

Armero, F., and I. Romero. 1999. *On the formulation of high-frequency dissipative time-stepping algorithms for nonlinear dynamics. Part I: Low order methods for two model problems and nonlinear elastodynamics.* Report UCB/SEMM-1999/05. Berkeley, Calif.: Department of Civil & Environmental Engineering, University of California.

Baber, T. T., and Y. K. Wen. 1979. *Stochastic equivalent linearization for hysteretic, degrading, multistory structures.* Report UILU-ENG-80-2001. Urbana, Ill: University of Illinois at Urbana-Champaign.

Bouc, R. 1967. Forced vibration of a mechanical system with hysteresis. Abstract in *Proceedings of the Fourth Conference on Nonlinear Oscillations.* p315. Prague, Czechoslovakia: Academia Publishing.

Dastous, J.-B., and J.-R. Pierre. 1996. Experimental investigation on the dynamic behavior of flexible conductors between substation equipment during an earthquake. *IEEE Transaction on Power Delivery* 11(2): 801–7.

Der Kiureghian, A., J. L. Sackman, and K.-J. Hong. 1999. *Interaction in interconnected electrical substation equipment subjected to earthquake ground motions.* PEER report 1999/01. Berkeley, Calif.: University of California.

Pacific Gas & Electrical Company. Electrical Design Standards. *Flexible strap connectors 700 to 3200 amps.* San Francisco: Department of Engineering.

Filiatrault, A., S. Kremmaidas, A. Elgamal, and F. Seible. 1999. *Substation equipment interaction: Rigid and flexible conductor studies.* Report SSRP-99/09. La Jolla, California: Division of Structural Engineering, University of California, San Diego.

IEEE. 1999. *Draft recommended practice for the design of flexible buswork located in seismically active area.* IEEE P1527/D5. Piscataway, N.J.: IEEE Standards Department.

Noiseux, D. U. 1992. Similarity laws of the internal damping of stranded cables in transverse vibrations. *IEEE Transactions on Power Delivery* 7(3): 1574–81.

Simo, J. C., and T. J. R. Hughes. 1998. *Computational Inelasticity.* Berlin: Springer Verlag.

Simo, J. C., N. Tarnow, and K. K. Wong. 1992. Exact energy-momentum conserving algorithms and symplectic schemes for nonlinear Dynamics. *Computer Methods in Applied Mechanics and Engineering* 100(1): 63–116.

Simo, J. C., N. Tarnow, and M. Doblare. 1995. Non-linear dynamics of three-dimensional rods: Exact energy and momentum conserving algorithms. *International Journal for Numerical Methods in Engineering*, 38(9): 1431–73.

Taylor, R. L. 1998. *FEAP Version 7.1 User Manual.* Berkeley, Calif.: Department of Civil and Environmental Engineering, University of California.

Transmission Line Reference Book: Wind-induced conductor motion. 1979. Palo Alto, Calif.: Electrical Power Research Institute.

Wang, C.-H., and Y. K. Wen. 1998. *Reliability and redundancy of pre-Northridge low-rise steel building under seismic excitation.* UILU-ENG-99-2002. Urbana, Ill.: University of Illinois at Urbana-Champaign.

Wen, Y. K. 1976. Method for random vibration of hysteretic systems. *Journal of the Engineering Mechanics Division*, ASCE 102(EM2): 249–63.

PEER REPORTS

PEER reports are available from the National Information Service for Earthquake Engineering (NISEE). To order PEER reports, please contact the Pacific Earthquake Engineering Research Center, 1301 South 46th Street, Richmond, California 94804-4698. Tel.: (510) 231-9468; Fax: (510) 231-9461.

PEER 2000/01 *Further Studies on Seismic Interaction in Interconnected Electrical Substation Equipment.* Armen Der Kiureghian, Kee-Jeung Hong, and Jerome L. Sackman. November 1999. $20.00

PEER 1999/11 *Performance Evaluation Database for Concrete Bridge Components and Systems under Simulated Seismic Loads.* Yael D. Hose and Frieder Seible. November 1999. $20.00

PEER 1999/08 *Envelopes for Seismic Response Vectors.* Charles Menun and Armen Der Kiureghian. July 1999. $26.00

PEER 1999/07 *Documentation of Strengths and Weaknesses of Current Computer Analysis Methods for Seismic Performance of Reinforced Concrete Members.* William F. Cofer. November 1999. $15.00

PEER 1999/06 *Rocking Response and Overturning of Anchored Equipment under Seismic Excitations.* Nicos Makris and Jian Zhang. November 1999. $15.00

PEER 1999/05 *Seismic Evaluation of 550 kV Porcelain Transformer Bushings.* Amir S. Gilani, Andrew S. Whittaker, Gregory L. Fenves, and Eric Fujisaki. October 1999. $15.00.

PEER 1999/04 *Adoption and Enforcement of Earthquake Risk-Reduction Measures.* Peter J. May, Raymond J. Burby, T. Jens Feeley, and Robert Wood. $15.00.

PEER 1999/03 *Task 3 Characterization of Site Response General Site Categories.* Adrian Rodriguez-Marek, Jonathan D. Bray, and Norman Abrahamson. February 1999. $20.00

PEER 1999/02 *Capacity-Demand-Diagram Methods for Estimating Seismic Deformation of Inelastic Structures: SDF Systems.* Anil K. Chopra and Rakesh Goel. April 1999. $15.00

PEER 1999/01 *Interaction in Interconnected Electrical Substation Equipment Subjected to Earthquake Ground Motions.* Armen Der Kiureghian, Jerome L. Sackman, and Kee-Jeung Hong. February 1999. $20.00

PEER 1998/08 *Behavior and Failure Analysis of a Multiple-Frame Highway Bridge in the 1994 Northridge Earthquake.* Gregory L. Fenves and Michael Ellery. December 1998. $20.00

PEER 1998/07 *Empirical Evaluation of Inertial Soil-Structure Interaction Effects.* Jonathan P. Stewart, Raymond B. Seed, and Gregory L. Fenves. November 1998. $26.00

PEER-1998/06 *Effect of Damping Mechanisms on the Response of Seismic Isolated Structures.* Nicos Makris and Shih-Po Chang. November 1998. $15.00

PEER 1998/05 *Rocking Response and Overturning of Equipment Under Horizontal Pulse-Type Motions.* Nicos Makris and Yiannis Roussos. October 1998. $15.00

PEER 1998/04 *Pacific Earthquake Engineering Research Invitational Workshop Proceedings, May 14–15, 1998: Defining the Links between Planning, Policy Analysis, Economics and Earthquake Engineering.* Mary Comerio and Peter Gordon. September 1998. $15.00

PEER 1998/03 *Repair/Upgrade Procedures for Welded Beam to Column Connections.* James C. Anderson and Xiaojing Duan. May 1998. $33.00

PEER 1998/02 *Seismic Evaluation of 196 kV Porcelain Transformer Bushings.* Amir S. Gilani, Juan W. Chavez, Gregory L. Fenves, and Andrew S. Whittaker. May 1998. $20.00

PEER 1998/01 Unassigned.

The Pacific Earthquake Engineering Research Center (PEER) is a consortium of western U.S. universities working in partnership with business, industry, and government to identify and reduce the risks from major earthquakes to life safety and to the economy.

PEER achieves its objectives of earthquake risk reduction through a coordinated program of research, education, and partnerships with users of research results. PEER's research program includes basic and applied components of seismology, engineering, architecture, urban planning, and economics.

PEER is headquartered at UC Berkeley.

PEER reports are available individually or by yearly subscription from the National Information Service for Earthquake Engineering (NISEE).

To order PEER Reports, contact the Pacific Earthquake Engineering Research Center, 1301 S. 46th St., Richmond, California 94804-4698, Tel: 510-231-9468, Fax: 510-231-9461.